Technical University of Denmark

DTU

Image Analysis for X-ray Imaging of Food

Einarsdottir, Hildur; Ersbøll, Bjarne Kjær; Larsen, Rasmus

Publication date:
2016

Document Version
Publisher's PDF, also known as Version of record

[Link back to DTU Orbit](#)

DTU Library
Technical Information Center of Denmark

Image Analysis for X-ray Imaging of Food

Hildur Einarsdóttir

DTU

Summary

X-ray imaging systems are increasingly used for quality and safety evaluation both within food science and production. They offer non-invasive and non-destructive penetration capabilities to image the inside of food.

This thesis presents applications of a novel grating-based X-ray imaging technique for quality and safety evaluation of food products. In this effort the fields of statistics, image analysis and statistical learning are combined, to provide analytical tools for determining the aforementioned food traits.

The work demonstrated includes a quantitative analysis of heat induced changes in microstructure of meat products. A segmentation framework is presented, from which geometrical parameters are assessed. The grating-based method embraces the complicated microstructure of the meat products, allowing for an analysis of the full three dimensional structure. The results illustrate that the combination of grating-based X-ray imaging and advanced analysis provides a valuable tool for microstructure analysis. Thus, the method can be considered as an alternative to other existing imaging techniques.

Furthermore, the thesis presents the application of grating-based X-ray imaging for novelty and defect detection in food. Compared to the complex three dimensional analysis of microstructure, here two dimensional images are considered, making the method applicable for an industrial setting. The advantages obtained by grating-based imaging are compared to conventional X-ray imaging, for both foreign object and defect detection. The results further emphasize the applicability of grating-based imaging for evaluation of food quality and food safety.

Resumé

Røntgensystemer bruges i stigende grad til kvalitets- og sikkerhedsvurdering, begge inden for fødevarevidenskab og produktion. Røntgen tilbyder gennemstrålings kapaciteter som er hverken invasive eller destruktive til at danne billeder af fødevarers indre struktur.

Denne afhandling præsenterer anvendelser af en ny gitter-baseret røntgenmetode til kvalitets- og sikkerhedsvurdering af fødevarer. Her kombineres metoder inden felterne af statistik, billedanalyse og statistisk læring. Målet er at udvikle analytiske værktøjer til anvendelse i de førnævnte applikationer.

Det præsenterede arbejde i afhandlingen består af en kvantitativ analyse af varmeinducerede ændringer i mikrostrukturen i kødprodukter. En segmenteringsmetode præsenteres, hvorfra geometriske parametre vurderes. Den gitterbaserede metode fanger den komplicerede mikrostruktur i kødprodukterne, der giver mulighed for en analyse af den fulde tredimensionelle struktur. Resultaterne illustrerer, at kombinationen af gitter-baserede røntgenbilleder og avanceret analyse er et værdifuldt redskab, og kan betragtes som et alternativ til andre eksisterende billeddannelses metoder.

Yderligere demonstreres anvendelsen af gitter-baserede røntgenbilleder til detektion af afvigelser og defekter i fødevarer. I stedet for den komplekse tredimensionelle analyse af mikrostruktur, bruges her todimensionelle billeder, hvilket gør metoden anvendelig til industriel brug. Fordelene opnået ved den gitterbaserede metode sammenlignes med konventionel røntgen, for detektion af begge fremmedlegemer og defekter. Resultaterne understreger yderligere anvendeligheden af metoden til vurdering af fødevarekvalitet og fødevaresikkerhed.

Preface

This thesis was prepared at the Department of Applied Mathematics and Computer Science at the Technical University of Denmark (DTU). The work was conducted at the Section of Image Analysis and Computer Graphics and the Section of Statistics and Data Analysis. It was done in fulfilment of the requirements for obtaining a *doctor of philosophy* degree (Ph.D.) in applied mathematics with an emphasis on image- and data analysis.

Two-thirds of the project funding originated from a research project granted by the Danish Council for Strategic Research: New X-ray imaging modalities for safe and high quality food 'NEXIM' (contract no. 11-116226), within the Program Commission on Health, Food and Welfare. The remaining funding was contributed by the ITMAN Graduate School program at DTU.

The thesis presents research focused on the application of grating-based X-ray imaging combined with statistics, image analysis, and statistical learning for evaluation of food quality and food safety. The first part of the thesis provides a motivation and background for the research, followed by the theoretical background relevant to the thesis work. Hereafter, the major contributions of the thesis work are presented and put into context to the methodologies presented. Finally, four original manuscripts that were prepared during the course of the Ph.D. study are included.

The project has been supervised by Professor Bjarne Kjær Ersbøll and co-supervised by Professor Rasmus Larsen. The research has been conducted at DTU, with collaborative work with Copenhagen University. Furthermore, the external research was conducted at the Technische Universität München, hosted by Professor Dr. Franz Pfeiffer at the Chair of Biomedical Physics.

Lyngby, 31-May-2016

Hildur Einarsdóttir

Acknowledgements

Contributions

Papers included in this thesis

[A] H. Einarsdottir, M. J. Emerson, L. H. Clemmensen, K. Scherer, K. Willer, M. Bech, R. Larsen, B. K. Ersbøll, & F. Pfeiffer (2016). Novelty detection of foreign objects in food using multi-modal X-ray imaging, *Food Control*, 67, 38-47.

[B] H. Einarsdottir, A. Yaroshenko, A. Velroyen, M. Bech, K. Hellbach, S. Auweter, Ö. Yildirim, F. G. Meinel, O. Eickelberg, M. Reiser, R. Larsen, B. K. Ersbøll, & F. Pfeiffer (2015). Computer-aided diagnosis of pulmonary diseases using x-ray darkfield radiography, *Physics in Medicine and Biology*, 60(24), 9253-9268.

[C] R. Miklos, M. S. Nielsen, H. Einarsdottir, R. Feidenhans'l, & R. Lametsch (2014). Novel X-ray phase-contrast tomography method for quantitative studies of heat induced structural changes in meat, *Meat Science*, 100, 217-221.

[D] H. Einarsdottir, M. S. Nielsen, R. Miklos, R. Lametsch, R. Feidenhans'l, R. Larsen, & B. K. Ersbøll (2014). Analysis of micro-structure in raw and heat treated meat emulsions from multimodal X-ray microtomography, *Innovative Food Science & Emerging Technologies*, 24, 88-96.

Other papers by author

- R. Miklos, M. S. Nielsen, H. Einarsdottir & R. Lametsch (2016). Grating-based X-ray tomography of 3D food structures. In *AIP Proceedings, 19th International ESAFORM Conference on Material Forming: ESAFORM.*

- R. Miklos, H. Einarsdottir, M. S. Nielsen, & R. Lametsch (2015). Novel X-ray phase-contrast tomography method for quantitative studies of the microstructure of meat-soy emulsions, In *Proceedings of the 12th International Congress on Engineering and Food: ICEF12.*

- H. Einarsdóttir, M. S. Nielsen, B. K. Ersbøll, R. Larsen, M. Bech, F. Pfeiffer, L. B. Christensen, & R. Feidenhans'l (2013). Contextual multivariate segmentation of pork tissue from grating-based multimodal X-ray tomography, In *Proceedings of Workshop on farm animal and food quality imaging: WFAFQI.*

- R. Miklos, R. Lametsch, M. S. Nielsen, T. Lauridsen, & H. Einarsdottir (2013). Effect of fat type and heat treatment on the microstructure of meat emulsions, In *Proceedings of InsideFood Symposium.*

- H. Einarsdottir, M. S. Nielsen, R. Miklos, R. Lametsch, R. Larsen, & B. K. Ersbøll (2013). Quantitative analysis of micro-structure in meat emulsions from grating-based multimodal X-ray tomography, In *Proceedings of InsideFood Symposium.*

- R. Miklos, M. S. Nielsen, H. Einarsdottir & R. Lametsch (2013). Application of X-ray phase contrast tomography in quantitative studies of heat induced structural changes in meat, In *Proceedings of the 59th International Congress of Meat Science and Technology: ICoMST 2013.*

Contents

Nomenclature

3D	Three-dimensional
AAM	Active appearance model
AUC	Area under the curve
CAD	Computer-aided diagnosis
CNR	Contrast-to-noise ratio
CT	Computed tomography
DA	Degree of anisotropy
DSC	Dice similarity coefficient
EM	Expectation-Maximization
FBP	Filtered back-projection
FN	False negative
FP	False positive
FPR	False positive rate
GBI	Grating-based imaging
GMM	Gaussian mixture model
GRF	Gibbs random field
JSC	Jaccard similarity coefficient

MAP   Maximum a posteriori

MIL   Mean intercept length

MLE   Maximum likelihood estimation

MRF   Markov random field

MRI   Magnetic resonance imaging

MSE   Mean squared error

N   Negatives

NMR   Nuclear magnetic resonance

OF   Overlap fraction

P   Positives

PCA   Principal component analysis

POV   Percent object volume

ROC   Receiver operating characteristic

SNR   Signal-to-noise ratio

SPCA   Sparse principal component analysis

SVD   Singular value decomposition

SVM   Support vector machines

TN   True negative

TNR   True negative rate

TP   True positive

TPR   True positive rate

µCT   Micro-computed tomography

Introduction

1.1   Scope of the project

The work presented in this thesis is a project within the New X-ray imaging modalities for safe and high quality food 'NEXIM' project, granted by the Danish Council for Strategic Research (contract no. 11-116226). The activities within the project aim at developing a new X-ray imaging technique specifically towards food applications. In this regard, the focus is to identify the areas within the Danish food industry with the highest technological and commercial impact. There are three focus points within these activities; i) to improve the detectability of low density foreign bodies, incidentally present in food products, like pieces of paper, plastic, wood and insects, ii) to develop new modalities for assessment of quality traits in food production like fatty acid composition, connective tissue and tenderness development, and iii) develop a proof-of-principle of a conveyor belt solution that could form the basis for real product development. These strategies have set the scope of the work presented in this thesis. The main focus is on developing advanced analysis techniques and combining them with the novel X-ray technique, thus addressing the first two topics mentioned.

1.2   X-ray imaging of food

In recent years, consumer demand for high quality, safe and consistent food products has been vastly growing [1, 2, 3]. Thus, it has become increasingly

important to monitor food production in order to predict consumer perception of the final product. Likewise, there is an increasing demand for healthier products without compromising the quality. Here, food engineering and design of food functionality play an important role. These two subjects, food safety and food quality, require the entire production chain to contribute to, and maintain, the high standards to ensure a positive consumer perception. Thus, monitoring the production is necessary to ensure such standards, enabling manufacturers to compete on the competitive international market. Previous strategies towards end-of-line production inspections are no longer adequate, and quality assurance is now required throughout the production chain both as regulatory compliance and to meet customer requirements [4]. In order to approach a zero-defect solution, future technologies for assessment of food quality will need to focus on better detection capabilities along with high sensitivity and specificity [5]. In this effort, research within industry and academia has focused on developing new and emerging technologies for the assessment of food quality and safety.

A number of emerging technologies exist for the purpose of non-destructive analysis of food quality and safety [6, 7]. These include hyperspectral imaging [8, 9, 10], nuclear magnetic resonance (NMR) spectroscopy and magnetic resonance imaging (MRI) [11, 12, 13], thermal imaging [14, 15], ultrasound imaging [16, 17], fluorescence imaging [18, 19, 20] and X-ray imaging [21, 22, 23, 24, 25, 26]. MRI and X-ray imaging provide penetration ability in a non-destructive manner, which allows for inspection of the actual spatial 3D structure of a sample. MRI systems are quite expensive and therefore not well-suited for industrial use for food manufacturing. In comparison, X-ray imaging systems are low-cost, and commercial systems are widely available. FOSS (Hillerød, Denmark) have developed an on-line dual-energy X-ray system (MeatMaster II), which measures the fat content of meat products at production speed. It also serves as a foreign object detector. Furthermore, an online X-ray system for meat trim analysis of the fat and lean ratio, bone detection and batch control has been developed by Marel (SensorX by Marel hf, Iceland). Additionally, there are commercially available X-ray tabletop systems such as the SkyScan µCT from Bruker (Brussels, Belgium).

X-ray imaging, first discovered by Wilhelm Röntgen [27], has found widespread use in the medical field, airport security scanning and in-line quality control on industrial production lines. Conventional X-ray systems typically consist of an X-ray source and a detector, which measures how much the initial X-rays are attenuated by an object. This is known as absorption X-ray imaging, and is the most common imaging modality for X-ray setups. Absorption X-ray imaging is well-suited for imaging materials with significant differences in density. However, the imaging technique often lacks contrast in materials with subtle differences in attenuation. These include soft tissues, hair, paper and plastics as their densities are similar to that of water [7]. The use of X-ray imaging for food

<div align="center">

(a) Absorption.   (b) Phase contrast.   (c) Dark field.

</div>
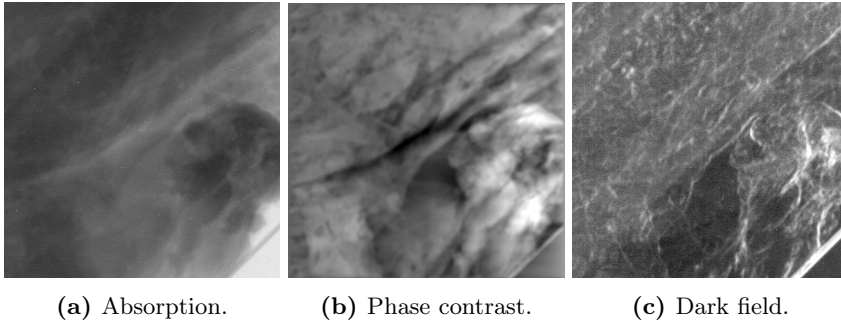
Figure 1.1: Bacon slices imaged with GBI. The images were recorded at a laboratory setup developed by Scherer et al. [51]. The phase-contrast modality was integrated as described in the same paper.

production has therefore mainly been limited to i) predicting carcass composition [28, 29, 30, 31], ii) foreign object detection of hard materials such as metal, bones and glass [23, 32, 33, 34] and iii) salt uptake in meat [35, 36, 37]. Low-energy X-rays (or soft X-rays) have less penetrating power, and systems utilizing them are more sensitive to subtle changes in densities. Soft X-ray imaging has been applied for quality inspection of wheat [38, 39, 40] and detecting insects in cereal grains [41]. Additionally, dual-energy X-ray techniques have also been applied for food quality inspection [42, 43].

For imaging of food products, the ability to measure subtle differences in materials is important, as this can allow for distinguishing between e.g. i) meat and connective tissue, ii) food products and soft plastics and iii) soft tissues and water. A recent X-ray technique based on grating-interferometry has introduced new imaging modalities capable of measuring the refraction and scattering of X-rays [44, 45, 46]. The approach, known as grating-based imaging (GBI), results in three imaging modalities with pixel correspondence. These three modalities are the conventional absorption X-ray imaging, phase-contrast imaging and dark-field imaging. Figure 1.1 shows slices of bacon imaged with GBI, and the different contrasts obtained by each modality. Enhanced contrast capabilities of these modalities over typical absorption X-ray imaging has previously been demonstrated [47, 48, 49, 50]. Jensen et al. [48] demonstrated how contrast between dermis and water was obtained by the phase-contrast modality, and in Nielsen et al. [49] the detection capabilities of organic foreign bodies in food products from the dark-field modality was demonstrated. Since the development of GBI in the early 2000s, research efforts have focused on obtaining high image quality for a number of applications such as imaging of breast cancer [52], differentiation of kidney stone types [53], investigation for quality testing fea-

sibility of porcine fat [48] and to improve diagnostic capabilities of pulmonary diseases [54]. The majority of research activities has thus focused on medical applications, and specifically on improving visual contrast for qualitative and quantitative purposes. Du & Sun [22] illustrated the importance of statistical learning techniques in computer vision for food, where topics such as segmentation, feature selection and classification are emphasized. Thus, in order to expedite the application of GBI towards food production, development of quantitative and automatic methods for quality and safety determination is equally as essential as further development of the imaging technique itself. The purpose of this thesis is to investigate and develop methods for this purpose, combining image analysis, statistics and statistical learning. The two main focus areas will be i) developing methods for quality assessment of food based on three-dimensional (3D) microstructure and ii) novelty and defect detection in food products.
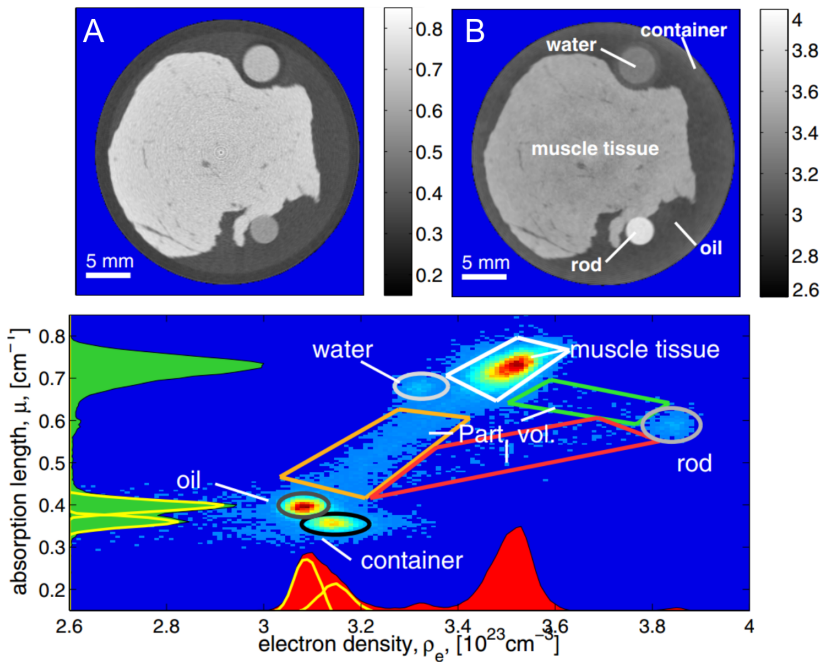
Figure 1.2: An absorption (A) and phase contrast (B) slice of a piece of beef in oil with a plastic rod and water as references. The two dimensional histogram is shown at the bottom. Reproduced from Nielsen et al. [55].

1.3   Motivating examples

1.3.1   Grating-based X-ray imaging of food

Previous studies have demonstrated the applicability of GBI for food products
to both determine food quality and for foreign object detection. Nielsen et al.
[55] demonstrated a grating-based X-ray tomography setup where pieces of meat
were imaged. The samples were a piece of pork backfat and a piece of beef muscle
tissue (Longissimus Dorsi). The absorption and phase-contrast modality gave
different contrasts, and a two dimensional histogram allowed for segmentation
utilizing the bivariate intensity information. Figure 1.2 shows the absorption
and phase-contrast modalities of the beef sample and corresponding bivariate
histogram. Nielsen et al. [49] also demonstrated the use of GBI radiography
for foreign object detection of organic material such as paper and insects. The
contrast obtained from the absorption modality and dark-field modality was
assessed using a measure of the contrast-to-noise ratio (CNR). Figure 1.3 shows
three foreign objects placed in minced meat. It is clear that the glass piece
(left) has higher visibility in the absorption image. On the contrary, the paper
(middle) and insect (right) are visible only in the dark-field modality. Kottler et
al. [56] applied GBI to store bought lasagne containing plastic tape and textile
fabric. The tape was visible in both the absorption modality and in dark field.
The fabric was however only visible in the dark-field image, due to the strong
scattering from the mesh of fibers. These studies underline the great potential
of GBI for food quality and food safety assessment. Detecting paper, plastic and
organic matters such as insects in food remains an unsolved major challenge [6].
Improving the detection of such light materials would add great benefit for food
manufacturers.
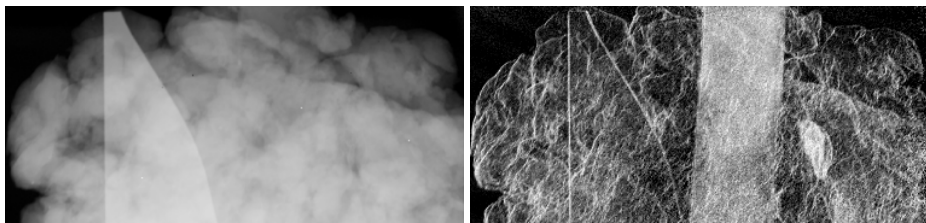
(a) Absorption modality.   **(b)** Dark-field modality.

Figure 1.3: X-ray images of minced meat with three foreign bodies; glass (left),
4 layers of paper (middle) and a ladybug (right). Adapted from
Nielsen et al. [49].

1.3.2 3D microstructure of food

Food microstructure analysis has been an important research field ever since microscopes were first presented [57]. As new and sophisticated techniques for micro-structural analysis are emerging, there has been an increasing interest in the subject. Microstructural properties are found to be related to nutrition, chemical and microbiological stability, texture and physical properties, transport properties and product engineering [58]. Applications vary from characterizing the stability and flow behaviour of food foams [59], measuring the rehydration kinetics of freeze-dried carrots [60] and determining the effects of fat level on the stability of meat emulsions [61]. Techniques for analyzing the microstructure of food include electron microscopy [62, 63, 64], MRI [65, 66] and X-ray micro-computed tomography (µCT) [25, 26]. X-ray µCT is a non-invasive and non-destructive technique requiring no sample preparation. The three dimensional data obtained from a µCT allows for internal examination of the structure of food products at resolutions ranging from millimeters to micrometers [67]. Additionally, food products can be imaged under normal conditions of temperature and pressure. Schoeman et al. [26] provide a detailed review demonstrating the ability of X-ray µCT as a non-destructive and non-invasive technique to investigate the 3D microstructure of a range of food products. As is highlighted in the paper, the image contrast obtained with X-ray µCT is due to differences in X-ray absorption caused by density and compositional variation in the sample. Thus, materials with similar density are difficult to distinguish by conventional X-ray µCT. This limits the application field of µCT to investigating the internal structure of products with significantly different attenuation properties.

To demonstrate the applicability of combining GBI imaging and advanced analysis methods for food quality assessment, µCT data obtained from a synchrotron source is analyzed. The main applications will be investigating thermally induced changes of microstructure in meat based products. The products are composed of elements with similar attenuation properties, and therefore the GBI technique is suitable for this purpose. Multivariate segmentation techniques will be considered to fully utilize the multimodal nature of the data. For engineering food functionality, product characterization and quality determination, the geometrical properties of food structure are needed. Therefore a geometrical parameter analysis will be performed to determine microstructural changes caused by heating of the samples. These include mass-, volume-, and area-related properties such as size, shape, surface area, porosity, density and volume [68].

1.3.3   Novelty and defect detection

X-ray systems have widely been used for detection of defects and contaminants in food products since the 1970s [69]. Applications range from bone detection in meat, poultry and fish [70, 33, 34], foreign object detection in dry foods [32] and defects in fruits [23, 71, 72]. Most applications focus on relatively homogeneous food products with varying thickness, and simple or adaptive thresholding techniques are commonly used for segmentation purposes. Some of the more advanced analyses performed include extensive feature selection and classification [72, 33]. For foreign object detection, it is important to note the type of foreign objects typically detected by conventional X-ray systems. These include hard and sharp objects such as metals, glass and bones that can pose hazard to the consumer if ingested. Other foreign objects may however also cause concern. Insects such as the housefly and cockroaches, can for instance be vectors of food-borne pathogens such as salmonella [73] and E. coli [74]. Additionally, foreign objects that do not typically pose a threat to the average consumer can pose a high risk to infants, elderly and physically or mentally challenged. Foreign object contamination incidences can cause great economic consequences for food manufacturers involving production downtime and large scale product recall, which can affect the consumer perception of the brand. There are also regulatory requirements by which food manufactures are obligated to use inspection technology available to ensure food safety, and they can be found liable for injuries or illnesses caused by their products if they fail to comply [23]. Therefore a balance between development of the X-ray technique itself and use of analysis methods is sought. Developing tailored methods for defect and contamination detection from X-ray images can prove costly and time consuming. Additionally, the price of an X-ray machine typically increases with its sophistication. Obtaining high-quality images can demand long acquisition times which may not be feasible for most on-line applications. Therefore, simple and generic algorithms are typically desired, to provide high capacity and robust solutions.

The work in this thesis contributes to the field of food monitoring, in terms of novelty and defect detection, by presenting applications of GBI by two cases. The first is focused on increasing the detectability of low-density foreign objects in food such as light plastics and insects, and performing a quantitative analysis to determine the gain from using the multimodal nature of the GBI method. Secondly, defect detection will be considered. As an example, defect detection of meat, poultry, cheese and fish can be concerned with detecting abnormal regions and shapes of the food products. The detection of defects will be demonstrated by the development of a computer-aided diagnosis (CAD) scheme for detecting pulmonary diseases in lungs. The scheme is designed to detect anomalies and defects, and can be adjusted to monitoring defects for food applications.

1.4   Thesis objectives

The main objectives of the thesis forming the basis of the included contributions are:

- To develop a generic multivariate segmentation tool taking spatial relations into account for multimodal X-ray tomography.

- To evaluate geometrical parameters for characterization of microstructure in meat products and how cooking alters these parameters.

- To quantitatively determine the gain from using the multimodal nature of GBI to detect low-density foreign objects in food products.

- To develop a defect detection scheme aimed to analyze products with geometrical structure.

- To further establish the use of GBI for food research and food production purposes, and also establish the use of automatic analysis techniques based on the cross-disciplinary fields of image analysis, statistics and statistical learning.

The objectives are accomplished through collaboration with other researchers within the fields of food science and physics.

1.5   Thesis outline

The thesis consists of two parts, a review of relevant methodology used throughout the thesis work and a summary of the scientific contributions.

Part I introduces and describes the relevant methodology used in the thesis work. It covers grating-based X-ray imaging, and methods from statistics, image analysis and statistical learning. The methods form the basis for the work presented in the included papers.

Part II summarizes the main scientific contributions of the included manuscripts. The papers are summarized into two groups; i) Quantitative analysis of microstructure for food quality evaluation and ii) novelty and defect detection. The summaries provide a general motivation for the presented work, and overview of the methods applied. The main results and contributions are also highlighted.

Conclusions of the thesis, along with a future outlook, are given before the included papers are appended.

Notation To aid the interpretation of abbreviations, a nomenclature is provided in the preface. In Part I, common notation for the methodology discussed is adopted from the literature, and referenced accordingly.

Part I

Methodology

Grating–based X-ray imaging

This chapter provides a review of the grating-based X-ray imaging technique. The purpose is to provide a high-level understanding of the basic concepts. References will be given to more thorough reviews were applicable. In order to better understand the concepts of grating-based X-ray imaging, the basic concepts of X-ray imaging are first explained.

2.1 Basics of X-ray imaging

A conventional X-ray setup consists of an X-ray source and detector, where in between the object of interest is placed. The common X-ray sources are X-ray tubes and synchrotrons. For now the remaining concepts of X-ray imaging will be described when an X-ray tube is used, and synchrotrons will be discussed in more detail later. X-ray tubes consist of a filament-type cathode and metal target called anode [75]. High-energy electrons are emitted from the cathode, and when they strike the target anode material (typically tungsten) they are decelerated by the atoms of the anode which causes Bremsstrahlung radiation (or breaking radiation). In this process X-ray photons are emitted. The two main characteristics of X-rays are their energy and intensity. The number of electrons

flowing per second from cathode to anode is determined by the current of the tube, thus determining the intensity of the X-ray beam. The maximum energy of the X-ray photons is determined by the voltage applied between cathode and anode, hence determining the energy or penetration power of the X-rays in the object to be imaged [75]. The focal spot of the tube is the region which the X-rays are emitted from and has great significance for the characteristics of the image produced [23]. A smaller focal spot allows for imaging of finer details in a material. The X-rays emitted can roughly be categorized into hard X-rays and soft X-rays. There is no formal distinction between the two, however soft X-ray wavelengths are said to span typically from 10 nm to 0.6 nm and hard X-rays from 0.6 nm to 0.01 nm. This range is also given as approximately 100 eV to 100 keV [76]. Hard X-rays have higher penetration power and are commonly used to investigate high-density materials such as metals, glass and bones. Soft X-rays on the other hand have low penetrating power and are more suitable for low-density materials such as fruits, vegetables and seeds [75]. The voltage of the X-ray tube, along with the filter used in the setup, determines the type of X-rays emitted.

Apart from the conventional X-ray setup previously described, several variants exist. These include dual- and multi-view X-ray imaging, dual- and multi-energy X-ray radiography, synchrotron radiation imaging and computed tomography (CT) X-ray imaging. Dual- and multi-view X-ray imaging obtains images from different angles in order to increase the information available of the object being imaged. Dual-energy X-ray imaging places two detectors in a stacked configuration, where soft X-rays are absorbed by the first detector and the hard X-rays by the second. The difference image then reveals information on low-density materials. Such systems are typically used for airport security scanning. Synchrotron radiation and X-ray CT (specifically μCT) both play an extensive role in this thesis and will therefore be described in more detail in Sections 2.1.2 and 2.1.3.

2.1.1 Attenuation mechanisms

Three interactions can occur when X-rays pass through matter. The X-rays can be absorbed, scattered or transmitted unaffected, and the loss of intensity of the X-rays is called attenuation. This loss in intensity depends on the composition of the material that the X-rays pass through, namely the absorption coefficient μ and the depth of penetration z (or thickness). The intensity of an X-ray beam after it passes through a medium is modelled as

$$I = I_0 \exp\left(-\mu z\right), \tag{2.1}$$

where I_0 is the initial beam intensity. The linear absorption coefficient is wavelength dependant, that is it depends on the photon energy of the X-ray beam. It

also depends on the material density and the atomic numbers Z of the elements composing the material. It is worth noting that soft tissues mainly consist of materials with low Z numbers such as hydrogen, oxygen and carbon. The absorption coefficients of soft tissue can be very similar and therefore it is hard to distinguish between them in absorption based X-ray imaging [77, 78].

Attenuation of X-rays mainly consists of three mechanisms; Rayleigh scatter (or coherent scatter), Compton scatter and photoelectric absorption. Rayleigh scattering is when the photons interact with matter and are re-emitted at the same energy in a different direction. The scattering predominately occurs with low energy radiation. The photoelectric absorption is when a photon is absorbed by a bound or orbital electron. In the process, an electron is emitted leaving the atom ionized. The probability of photoelectric absorption is higher for electrons tightly bound in high Z materials as the binding energies are closer to X-ray photon energies. Thus, electrons in the K shell (the closest shell to the nucleus) are predominantly involved. Soft tissue does not have significant photoelectric absorption, as opposed to denser matter such as calcium in bones. Finally, Compton scattering is the main contribution to the scattering of X-rays in a material. The scattering occurs when an X-ray photon collides with the loosely bound electron on the valence shell of the atom, causing the incident photon and electron to scatter. Compton scattering further ionizes other atoms. The scattering is proportional to the physical and electron density of the material, and inversely proportional to the energy of the photon. Photoelectric absorption is the dominating factor to attenuation at low energies for materials with high atomic numbers. Compton scattering on the other hand is dominant for high energies and low atomic numbers, and is the most significant source of attenuation in soft tissue.

2.1.2   Synchrotron sources

Synchrotrons have driven X-ray imaging to an extreme, demonstrating new modalities and imaging capabilities. They obtain both excellent signal-to-noise ratio and high resolution capabilities, making them superior to laboratory X-ray setups. Synchrotron radiation imaging is performed at large scale facilities, where a highly coherent X-ray beam, both in terms of spatial coherence and spectral width, can be obtained [77]. The X-rays in synchrotrons are produced by accelerating electrons using magnetic fields in a circular accelerator. A further magnetic field, e.g. an undulator, consisting of a periodic structure of dipole magnets is used to force the electrons to oscillate and thereby to radiate energy. The electrons emitted have several GeV in energy and emit a narrow beam of polychromatic radiation consisting of soft UV light to hard X-rays. The required wavelength for a particular experiment can be tuned by monochromator crys-

tals [79]. The ability to use monochromatic radiation, that is the selection of specific wavelengths of radiation, eliminates beam hardening effects [80]. Synchrotron sources give high brilliance, which describes the brightness and the angular opening of the beam. Brilliance considers the number of photons produced per second, the angular divergence of the photons, the cross-sectional area of the beam and the photons falling within a bandwidth of 0.1% of the central wavelength [81]. The high flux obtained at synchrotrons allows the use of shorter exposure time. The small source size further allows for the depiction of more details. Synchrotron sources are thus ideal for high resolution tomography, where high contrast is obtained for small samples.

2.1.3   Computed tomography

In order to quantitatively analyze the microstructure of food products, the internal three-dimensional information must first be obtained. Computed tomography is a method for constructing a three dimensional (3D) image of a sample by X-ray imaging. The procedure collects X-ray images taken at many different viewing directions, and the 3D image is then reconstructed mathematically from these images. In more detail, an ideal X-ray beam of a CT scanner consists of parallel pencil-beams of X-rays which travel from the source, through a sample and the attenuation is then analyzed by a detector. Either the X-ray source and detector or the sample itself is then rotated, and a number of projections taken at different angles [82]. The CT measurements thus consist of the sum of attenuation coefficients μ_i in every voxel that lies in the path of each pencil-beam of the X-rays. The measured X-ray beam will have intensity I as given by

$$I = I_0 \exp\left(-z \sum_{i=1}^{n} \mu_i\right). \tag{2.2}$$

Equation (2.2) is an approximation since low-energy X-rays are typically absorbed with polychromatic sources [82]. This is called beam hardening and can be corrected for by either placing filters to remove the low-energy X-rays, or as a post-processing step after data acquisition [83, 84, 85]. In order to reconstruct the 3D image, filtered back-projection (FBP) is most commonly used. The basis for tomographic reconstruction by FBP was first introduced by Johann Radon. FBP is a modified version of simple backprojection where the value in the projection image is backprojected by setting the voxels of each individual pencil-beam to the same value. The backprojected image is then the sum of all the backprojected views. Figure 2.1b shows the result from simple backprojection reconstruction of the image in Figure 2.1a. The resulting reconstruction becomes blurry and is in general not a good solution. In FBP the algorithm corrects the blurring effect by first filtering each view before backprojecting. Given

(b) Back projection.

(a) Projection angles.

(c) Filtered back projection.
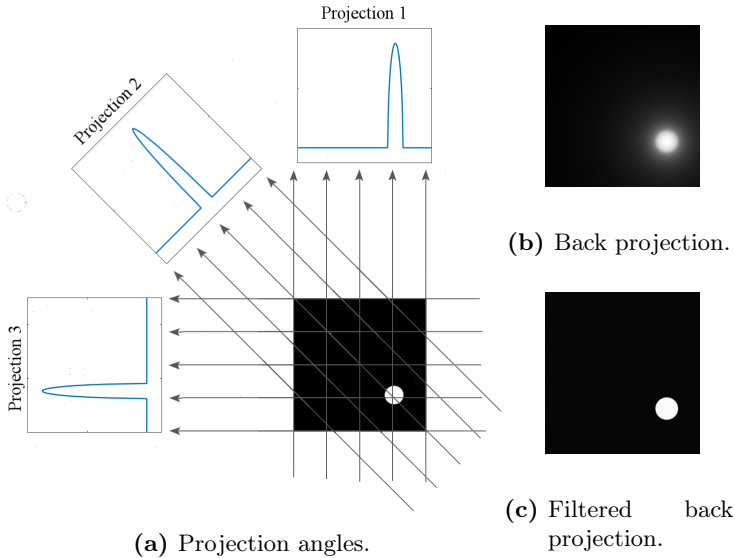
Figure 2.1: The reconstructed images of the multiple views in a) calculated by b) back-projection and c) filtered-back projection.

an infinite number of views and infinite number of points the FBP method will produce an ideal solution identical to the correct image. A FPB reconstruction of the image in Figure 2.1a is shown in Figure 2.1c. In general a CT scanner consists of a cone beam geometry, which requires the use of different filtering operations during reconstruction. The parallel case presented here only applies in first approximation at synchrotrons. For scenarios when the FBP is not adequate, iterative reconstruction techniques can be alternatively used [86].

2.1.4 Noise sources and artifacts

Several random processes contribute to the noise of X-ray imaging. These include; i) the number of photons emitted from the X-ray source, ii) the number of photons that pass unaffected through the material, iii) the number of photons captured by the detector, iv) the number of X-ray photons converted to visible light photons and v) the response of the imaging device. In general, the overall noise is Poisson distributed. For X-ray imaging, noise is usually evaluated by comparing the signal-to-noise ratio (SNR).

The quantum noise of the X-ray system is not the only contributor to decreased image quality. Image artifacts are undesired image features that can occur in sev-

eral ways. The most common include; i) motion artifacts which is when a sample moves during the image acquisition, ii) ring artifacts in CT where miscallibration and defects in the detector are the culprit, iii) streak artifacts caused by beam hardening, scatter, Poisson noise, motion and edge effects, and iv) partial volume effects where voxels in a CT image consist of a combination of different materials. The analysis methods applied to X-ray data need to consider these effects in order to obtain a reliable result.

2.2   Grating interferometry

Grating-based imaging (GBI) is based on measuring three types of physical interactions i) attenuation, ii) refraction and iii) scattering, obtained from the absorption, phase-contrast and dark-field imaging modalities, respectively. Figure 2.2 shows the effect of an incoming Gaussian shaped beam profile (shown in black) when samples with different physical properties are measured. The colored profiles represent what the detector records when a sample is present. The effect from an absorptive material is depicted in green, and illustrates an attenuation of the beam, while in blue, the effect of a refractive material is seen to cause a transverse shift in the position of the beam profile. Finally, in red, the small-angle scattering from a material with ordered microstructure causes a broadening of the beam profile. These three complementary interactions can be measured, resulting in three imaging modalities with pixel or voxel correspondence.
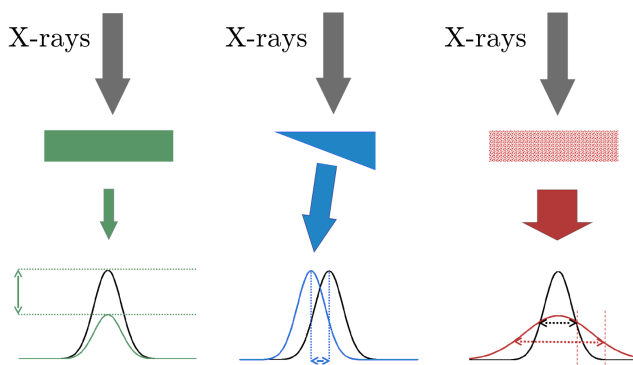
Figure 2.2: The incoming X-ray beam changes when a sample is present. The effect on the beam from an absorptive material (green), a refractive material (blue) and a material with a homogeneous distribution of microstructures (red). Adopted from Nielsen [87].
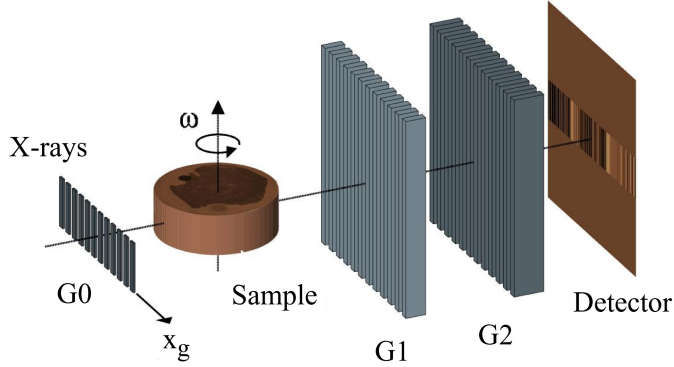
Figure 2.3: Grating-based X-ray imaging setup. The phase-grating G1 creates an interference pattern that is analyzed by the detector through the analyzer grating G2. If the X-ray source lacks spatial coherence, the source grating G0 can be included. For a radiographic setup the sample is simply placed before the phase-grating, if tomography is required a rotating stage is mounted. Reproduced from Nielsen [55].

The GBI setup is illustrated in Figure 2.3. In order to obtain the desired image contrast a phase grating G1 is placed after the sample. The grating acts as a phase mask, imprinting periodic phase modulations onto the incoming wave field [88]. This phase modulation is transformed into an intensity modulation in the plane of the analyzer grating G2 through the Talbot effect [89]. The Talbot effect forms a linear periodic fringe pattern that is perpendicular to the setup axis and parallel to the fringe lines of G1. Grating G2, placed immediately before the detector, has absorbing lines and the same orientation and periodicity as the fringes created by G1. Either the G1 or G2 grating can then be stepped in the x_g direction, scanning the oscillation of the intensity signal $I(m,n)$ for each pixel (m,n). The sample can be mounted on a rotation stage for tomography imaging. The grating interferometer can be used to measure all three afore-mentioned effects. For refraction, this is done by measuring the slight angular change of an incoming X-ray beam as it passes through a sample, which causes a transverse displacement of the interference pattern produced by the grating setup. For scattering the blurring of the interference pattern can be measured. The details of the grating interferometer are thoroughly discussed in [90, 91, 92] for synchrotron sources and in [45] for laboratory-based setups. For tomography, the full complex refractive index can be reconstructed as shown in [93, 94], along with performing dark-field tomography [44].

2.2.1   Contrast mechanisms

As for visible light, matter can refract X-rays, and the description of attenuation and refraction of X-rays can be combined through the complex index of refraction as given in [81]

$$n = 1 - \delta + i\beta, \tag{2.3}$$

where the real part δ and the imaginary part β are related to the attenuation length μ^{-1} and electron density ρ_e, respectively. For X-rays, both δ and β are small quantities $(< 10^{-5})$ and are given by

$$\delta = \frac{2\pi\rho_a Z r_0}{k^2} \tag{2.4}$$

$$\beta = \frac{\mu}{2k}, \tag{2.5}$$

where the atomic number density ρ_a and atomic number Z are related to the electron density $(\rho_e = \rho_a Z)$, r_0 is the Thomson scattering length [81], and $k = 2\pi/\lambda$ is the X-ray wave number where λ is the wavelength. For low atomic numbers, the phase shift of an X-ray beam is larger than the absorption effect, indicating higher sensitivity to density variations [77].

The dark-field imaging modality introduced by Pfeiffer et al. [46] measures the reduction in visibility of the interference pattern, and is described as a beam spread caused by small angle scatter and multiple refraction [77]. Bech et al. [44] demonstrated an imaging approach to measure the scattering by assuming that the angular probability distribution $A(\theta)$ of the scattered intensity is Gaussian

$$A(\theta) = \frac{1}{\sigma\sqrt{2\pi}} \exp\left(-\frac{\theta^2}{2\sigma^2}\right), \tag{2.6}$$

where μ and σ are the mean and standard deviation, respectively, and θ is the scattering angle. The recorded intensity is the convolution $I^s = I^r \otimes A(\theta)$, where the superscript s denotes the presence of a sample and r denotes the reference without the sample.

2.2.2   Imaging modalities

The grating-interferometer creates an interference pattern which changes when a sample is placed in the X-ray beam. As previously mentioned, this interference pattern can be reconstructed from the images obtained by stepping either the G1 or G2 grating. A minimum of three equidistant transverse shifts of the grating are required to extract the three imaging signals [77]. A reference scan where
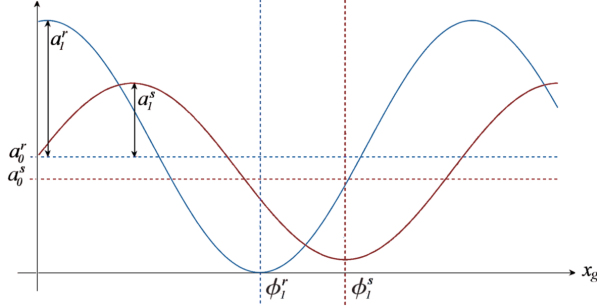
Figure 2.4: The absorption, change in phase and dark-field signal can be calculated from the change in sinusoidal intensity profiles between the reference (in blue) and when a sample is present (in red). Adapted from Nielsen [87].

no sample is present is then compared with a sample scan and the attenuation, refraction and scatter can be calculated. This is done by analyzing the oscillation of the intensity $I(m, n)$ for every pixel (m, n) written in a Fourier series [88]

$$I(m, n, x_g) = \sum_i a_i(m, n) \cos\left(ikx_g + \phi_i(m, n)\right) \tag{2.7}$$

$$\approx a_0(m, n) + a_1(m, n) \cos\left(kx_g + \phi_1(m, n)\right), \tag{2.8}$$

where a_i are the amplitude coefficients, ϕ_i are the corresponding phase coefficients, $k = 2\pi/p_2$ and p_2 is the period of grating G2. The higher order terms are ignored for adequately large source sizes, as their contribution is less than 0.1% [77]. The normalized average transmission of the sample in each pixel is then given by

$$T(m, n) = \frac{a_0^s(m, n)}{a_0^r(m, n)}, \tag{2.9}$$

corresponding to what is measured in a conventional absorption X-ray setup. Pfeiffer et al. [45] show that by analyzing the lateral shift of the intensity modulation, the phase-contrast imaging modality can be obtained. This lateral shift is the $\phi_1(m, n)$ quantity in Equation 2.8. The relative phase shift is given as

$$\phi_1(m, n) = \phi_1^s(m, n) - \phi_1^r(m, n). \tag{2.10}$$

The dark-field imaging modality measures the scattering power of the sample, and information on the scattering is contained in the first Fourier component of $I(m, n, x_g)$. In other words, the amplitude of the first Fourier component a_1 decreases when X-rays are scattered or reflected through the sample [46]. This is illustrated in Figure 2.4. In order to quantitatively describe the change in

the oscillation amplitude when a sample is present, the normalized reference oscillation amplitude is first defined by the ratio

$$V^r(m,n) = \frac{I^r_{\max} - I^r_{\min}}{I^r_{\max} + I^r_{\min}} = \frac{a^r_1(m,n)}{a^r_0(m,n)}. \tag{2.11}$$

The relative visibility decrease V when a sample is present is then defined as the normalized visibility

$$V(m,n) = \frac{V^s(m,n)}{V^r(m,n)} = \frac{a^r_0(m,n)a^s_1(m,n)}{a^s_0(m,n)a^r_1(m,n)}. \tag{2.12}$$

When a sample has negligible small angle X-ray scattering the visibility remains unchanged and $V(m,n) = 1$. For strongly scattering samples, the visibility drops resulting in $V < 1$ [46].

The phase-contrast and dark-field sensitivity is primarily defined by the parameters of the gratings, and only secondly by the X-ray beam properties. The high quality of the beam at synchrotrons allows to use equipment that is very sensitive to small changes [77]. X-ray tube sources have very different beam properties, they are highly divergent allowing for large field of views at a short distance. Coherence of a conventional X-ray tube is achieved by adding the source grating G0 as previously mentioned.

Image acquisition is the first step to obtaining a meaningful representation of a sample measured. In order to give a quantitative analysis of the sample characteristics, image segmentation and classification become essential. The topics of segmentation and classification will be discussed in the following chapter.

CHAPTER 3

Segmentation and classification

This chapter presents the main topics within the fields of statistics, image analysis and statistical learning relevant to the work in this thesis. First, the basic statistical methods used are presented. The methods are in large based upon the normal distribution. Next, the topics of image segmentation will be introduced, where the focus will be on models that include prior information of both intensity and shape. Finally, methods of statistical learning for both classification and interpretation of data are discussed. In addition to presenting the relevant theory, this chapter will also focus on illustrating the importance of model selection and evaluation of segmentation and classification results.

3.1   Statistical methods

Statistics form an important basis for other advanced methods within image analysis and statistical learning. This section presents methods based on normal distributions, including the definition of a univariate and multivariate normal distribution, mixture of Gaussians modeling, and the Mahalanobis distance measure.

3.1.1   Normal distribution

The normal distribution, or Gaussian distribution, is commonly used in image analysis. It is a parametric model which is represented by two parameters, the mean μ and variance σ^2. These parameters can be estimated from a given data set $X \in \mathcal{N}(\mu, \sigma^2)$ as

$$\mu = \frac{1}{n} \sum_j x_j, \tag{3.1}$$

and

$$\sigma^2 = \frac{1}{n} \sum_j (x_j - \mu)^2, \tag{3.2}$$

where σ^2 is a biased estimator of the sample variance. The unbiased estimator normalizes by $n - 1$ instead of n. The probability density of the normal distribution is given as

$$\mathcal{N}(x \mid \mu, \sigma^2) = \frac{1}{\sqrt{2\pi}\sigma} \exp\left(-\frac{1}{2}\frac{(x-\mu)^2}{\sigma^2}\right). \tag{3.3}$$

The multivariate Gaussian distribution $\mathbf{X} \in \mathcal{N}(\boldsymbol{\mu}, \boldsymbol{\Sigma})$ is defined as

$$\mathcal{N}(\mathbf{x} \mid \boldsymbol{\mu}, \boldsymbol{\Sigma}) = \frac{1}{\sqrt{(2\pi)^p |\boldsymbol{\Sigma}|}} \exp\left(-\frac{1}{2}(\mathbf{x}-\boldsymbol{\mu})^{\mathrm{T}}\boldsymbol{\Sigma}^{-1}(\mathbf{x}-\boldsymbol{\mu})\right) \tag{3.4}$$

$$= \frac{1}{Z} \exp\left(-\frac{1}{2}\log|\boldsymbol{\Sigma}| - \frac{1}{2}(\mathbf{x}-\boldsymbol{\mu})^T\boldsymbol{\Sigma}^{-1}(\mathbf{x}-\boldsymbol{\mu})\right), \tag{3.5}$$

where p is the number of dimensions, $\boldsymbol{\mu}$ is the mean vector, $\boldsymbol{\Sigma}$ is the covariance matrix, $|\boldsymbol{\Sigma}|$ is the determinant of $\boldsymbol{\Sigma}$ and Z is a normalization constant.

3.1.2   Gaussian mixture model

Often data is not well represented by a single distribution and instead consists of multiple distributions. The Gaussian mixture model (GMM) incorporates this by representing a mixture of K Gaussian distributions as

$$p(\mathbf{x}) = \sum_{k=1}^{K} \pi_k \mathcal{N}(\mathbf{x} \mid \boldsymbol{\mu}_k, \boldsymbol{\Sigma}_k) \tag{3.6}$$

$$= \sum_{k=1}^{K} \frac{1}{Z} \exp\left(\log \pi_k - \frac{1}{2}\log|\boldsymbol{\Sigma}_k| - \frac{1}{2}(\mathbf{x}-\boldsymbol{\mu}_k)^T\boldsymbol{\Sigma}_k^{-1}(\mathbf{x}-\boldsymbol{\mu}_k)\right), \tag{3.7}$$

where π_k is the prior probability of each mixture.

3.1.3   Maximum likelihood estimation

The maximum-likelihood estimation (MLE) is a method to estimate the parameters of a distribution for given data. The following review of MLE is based on the notation as given by Hastie et al. [95]. A probability density function for observations x from the distribution X can be specified as

$$x_i \sim g_\theta(x), \tag{3.8}$$

where if X has a normal distribution, then θ is the parameters (μ, σ^2) and $g_\theta = \mathcal{N}(x \mid \mu, \sigma^2)$ as given in Equation (3.3). The likelihood function, or the probability of the observed data for g_θ, for data $\mathbf{X}$ is defined as

$$L(\theta; \mathbf{X}) = \prod_{i=1}^{N} g_\theta(x_i), \tag{3.9}$$

where N is the number of observations. The MLE chooses the value of the parameters $\theta = \hat{\theta}$ that maximizes the log-likelihood given as

$$\ell(\theta, \mathbf{X}) = \sum_{i=1}^{N} \ell(\theta; x_i), \tag{3.10}$$

where $\ell(\theta; x_i) = \log g_\theta(x_i)$ is the log-likelihood [95].

3.1.4   Expectation-Maximization

The Expectation-Maximization (EM) algorithm deals with fitting the parameters of a parametric model [96]. Given the observed data $\mathbf{X}$, sampled from a parametric distribution with unknown parameters $\boldsymbol{\theta}$, the latent variables $\mathbf{Z}$ and a likelihood function $L(\boldsymbol{\theta}; \mathbf{X}, \mathbf{Z}) = p(\mathbf{X}, \mathbf{Z}|\boldsymbol{\theta})$, the EM algorithm calculates the MLE of $\boldsymbol{\theta}$. Here, latent variables are not directly observed, but are rather inferred from other variables that are observed.The EM algorithm is an iterative method, alternating between two steps. First an expectation step (E) is performed, which uses the current estimate of parameters $\boldsymbol{\theta}$ to evaluate the expectation of the log-likelihood. A maximization step (M) follows, that computes the parameters that maximize the expected log-likelihood found in the E step. The two steps are briefly described as follows [95]:

Expectation step   The E step calculates the expected value of the log-likelihood function given the observed data $\mathbf{X}$ and current estimate of the parameters $\boldsymbol{\theta}^k$. The expectation value is defined as

$$Q(\boldsymbol{\theta}|\boldsymbol{\theta}^k) = E_{\mathbf{Z}|\mathbf{X}, \boldsymbol{\theta}^k} L(\boldsymbol{\theta}; \mathbf{X}, \mathbf{Z}). \tag{3.11}$$

Maximization step The M step calculates optimal values for $\boldsymbol{\theta}$ given the expectation value from the E step. The parameter estimates are defined by

$$\boldsymbol{\theta}^{k+1} = \arg\max_{\boldsymbol{\theta}} Q(\boldsymbol{\theta}|\boldsymbol{\theta}^k). \tag{3.12}$$

The two steps are then repeated until convergence is obtained. The EM algorithm does not guarantee a globally optimum solution, and rather converges to a local optima [97]. In high-dimensional spaces there can be a number of local optima, and therefore the performance of the EM algorithm can be poor. The number of Gaussians to be fitted also greatly affects the result of the EM algorithms. Gap statistics [98] can be used to estimate the number of Gaussians in the given data, in hopes of obtaining a better performance from the EM algorithm.

3.1.5 Mahalanobis distance

Given a data point $\mathbf{x}$ and normal distribution $\mathbf{X} \in \mathcal{N}_p(\boldsymbol{\mu}, \boldsymbol{\Sigma})$, the Mahalanobis distance measures the distance between the two by taking into account the correlations of the data. In other words, the Mahalanobis distance measures how many standard deviations $\mathbf{x}$ is from the given distribution. It is defined as

$$D(\mathbf{x}) = \sqrt{(\mathbf{x} - \boldsymbol{\mu})^T \boldsymbol{\Sigma}^{-1} (\mathbf{x} - \boldsymbol{\mu})}. \tag{3.13}$$

The Mahalanobis distance corresponds to the Euclidean distance in a transformed space. It is unit less and scale-invariant. Since the Mahalanobis distance uses the inverse of the variance-covariance matrix, several computational problems can arise. Data containing a large number of variables that are correlated can lead to a singular or nearly singular variance-covariance matrices which cannot be inverted. Secondly, for $p >> n$ problems, i.e. there are more variables than observations, the calculation of the variance-covariance matrix also becomes problematic. For these cases the Mahalanobis distance can be calculated using a subset of variables found with e.g. principal component analysis [99] (see Section 3.3.5). The Mahalanobis distance can be used as a suitable metric for outlier detection and as a distance classifier.

3.2 Image segmentation

Image segmentation is concerned with the task of dividing an image into separate regions, and thereby representing meaningful segments of the image. In the following sections, a selection of segmentation methods relevant to the work in this thesis will be presented. This includes Bayesian classification, which is related to the Markov random field (MRF) framework [100]. The MRF framework is a state-of-the-art general probabilistic framework that can be used to model a priori knowledge of the spatial context of an image. MRFs work well for minimizing segmentation errors due to image noise and partial volume effects. For problems where the image to be segmented contains a well defined structure, and given a set of annotated training shapes, an even stronger prior can be included. This is achieved by for instance the active appearance model (AAM) framework [101]. The AAM combines shape and texture into a single model, and is ideal for segmenting known anatomical structures.

3.2.1 Bayesian classification

Bayesian statistics are well established for estimation and decision-making, and form a basis for many advanced segmentation methods. They play a crucial role towards formulating the MRF segmentation model. The reader is thus reminded of the Bayesian modeling paradigm for the purpose of multivariate classification.

Given a data point $\mathbf{x} = (x_1, ..., x_n)$, where n is the number of variables, and possible class labels $\boldsymbol{\pi} = (\pi_1, ..., \pi_m)$, where m is the number of possible classes, the Bayes conditional probability model assigns probabilities $P(\pi_k \mid \mathbf{x})$ for each of the $k = 1, ..., m$ possible classes of $\boldsymbol{\pi}$ [102]. The posterior probability can be calculated by using Bayes theorem

$$P(\pi_k \mid \mathbf{x}) = \frac{P(\mathbf{x} \mid \pi_k)P(\pi_k)}{P(\mathbf{x})}, \tag{3.14}$$

where $P(\pi_k)$ is the prior probability, $P(\mathbf{x} \mid \pi_k)$ is the probability of $\mathbf{x}$ conditioned on π_k and $P(\mathbf{x})$ is the weighted combination of $P(\mathbf{x} \mid \pi_k)$ given as

$$P(\mathbf{x}) = \sum_{i=k} P(\mathbf{x} \mid \pi_i)P(\pi_i). \tag{3.15}$$

Assuming the probability follows a normal distribution $\mathcal{N}(\boldsymbol{\mu}, \boldsymbol{\Sigma})$, the posterior probability is given by Equation 3.4 as

$$f(\mathbf{x} \mid \pi_k) = \frac{1}{\sqrt{2\pi}^n \sqrt{|\boldsymbol{\Sigma}_k|}} \exp\left(-\frac{1}{2}(\mathbf{x} - \boldsymbol{\mu}_k)^{\mathrm{T}} \boldsymbol{\Sigma}_i^{-1}(\mathbf{x} - \boldsymbol{\mu}_k)\right), \quad k = 1, ..., m, \tag{3.16}$$

The maximum a posteriori (MAP) solution is found by

$$f^* = \arg\max_{f \in F} P(f \mid x),\qquad\qquad(3.17)$$

where F is the set of all possible label combinations $f \forall k$ [100].

3.2.2   The Markov random field framework

X-ray imaging noise and artifacts can affect a final segmentation, and typically pixel-wise classification is not sufficient to obtain a satisfactory result. Applying a model capable of capturing contextual constraints can minimize these effects. By doing so, a prior is incorporated which presumes homogeneity of regions, i.e. intensity and texture. The Markov random field framework is a probabilistic model which captures such contextual constraints. The Markov random field framework is well described by Li in [100], and will briefly be touched upon here. Before the MRF is defined, some concepts and notions are first given.

Random fields

An image can be defined as a set of regular sites $\mathcal{S}$, where each site represents a pixel for a two dimensional image or voxel for a three dimensional image. This set of sites can be considered as a random field, where each site has a stochastic variable associated with it. Sites are thus spatial positions (pixels or voxels) $\mathcal{S} = \{s_1, ..., s_n\}$, where n is the number of sites. Each site is assigned a label l and the set of possible labels is denoted by $\mathcal{L} = \{l_1, ..., l_m\}$, which for segmentation purposes are categorized as discrete, and m is the number of possible labels. The mapping from sites to labels $f : \mathcal{S} \rightarrow \mathcal{L}$ assigns a label from the label set $\mathcal{L}$ to site $i \in \mathcal{S}$. In other words, each site has an associated stochastic variable f_i, where the stochastic variables can take on a value within the set of labels $\mathcal{L}$, i.e. $f_i \in \mathcal{L}$.

Neighborhood structure

A neighborhood for each site i is defined as $\mathcal{N}_i$, which consists of neighboring sites. The collection of neighborhoods gives the neighborhood structure $\mathcal{N}$. A
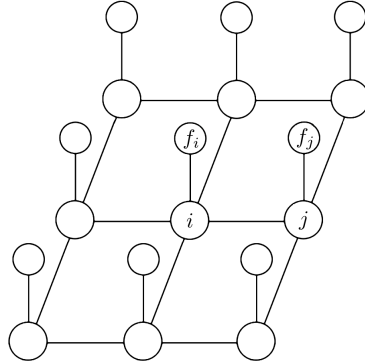
Figure 3.1: The model for a random field on a 4-neighborhood regular lattice grid.

formal definition of neighborhood structure $\mathcal{N}$ is given as

$$\mathcal{N} = \{\mathcal{N}_i \mid \forall i \in S\} \tag{3.18}$$

$$i \neq \mathcal{N}_i \tag{3.19}$$

$$j \in \mathcal{N}_i \Leftrightarrow i \in \mathcal{N}_j. \tag{3.20}$$

The definition states that a site cannot be a member of its own neighborhood and that if site j is a neighbor to site i, then site i must be a neighbor to site j. A first-order neighborhood system on a regular lattice is defined such that the nearest neighbors of a site define its neighborhood (i.e. four nearest neighbors on a regular 2D lattice and six nearest neighbors for a 3D lattice). Figure 3.1 illustrates sites of a regular grid with a 4-neighborhood structure. A subset of sites in $\mathcal{S}$ with neighborhood $\mathcal{N}$ is defined as a clique c, where a single site is $c = \{i\}$ and a pair of neighboring sites $c = \{i, j\}$. The set of single sites is denoted $C_1 = \{i \mid i \in \mathcal{S}\}$ and pair-sites $C_2 = \{(i, j) \mid j \in \mathcal{N}_i, \ i \in \mathcal{S}\}$ (horizontal- or vertical neighbors). Finally, the entire collection of cliques for $\{\mathcal{S}, \mathcal{N}\}$ is $\mathcal{C} = \mathcal{C}_1 \cup \mathcal{C}_2$.

Markov random fields

Given the random field $\mathcal{F}$ with neighborhood structure $\mathcal{N}$ and label set $\mathcal{L}$, the Markov property states that the random field is a Markov random field if and only if the following criterion are fulfilled

$$P(\mathcal{F} = f) > 0 \quad \forall f \in \mathcal{F} \tag{3.21}$$

$$P(f_i | f_{\{\mathcal{S} \setminus i\}}) = P(f_i | f_{\mathcal{N}_i}), \tag{3.22}$$

where $f_{\{\mathcal{S} \setminus i\}}$ is the set of labels at the sites in $\mathcal{S} \setminus i$ and

$$f_{\mathcal{N}_i} = \{f_j \mid j \in \mathcal{N}_i\}, \tag{3.23}$$

is the set of labels at the sites neighboring i. The Markov property thus states that all information about what label to assign to site i is contained in the labels of the neighbors to that site.

The Ising model

A special case of the MRF is the Ising model [103] which considers a binary labeling problem $\mathcal{L} = \{-1, 1\}$. The model is based on a 4-connectedness neighborhood structure on a regular lattice. The probability distribution function for the Ising model is given as

$$p(f_i \mid f_{\mathcal{N}_i}) = \frac{\exp\left(\alpha_i f_i + \sum_{j \in \mathcal{N}_i} \beta_{ij} f_i f_j\right)}{\sum_{f_i \in \mathcal{L}} \exp\left(\alpha_i f_i + \sum_{j \in \mathcal{N}_i} \beta_{ij} f_i f_j\right)}, \tag{3.24}$$

where α_i is a constant for each site and β_{ij} is a smoothing parameter for each neighborhood pair. The denominator of Equation (3.24) is a normalizing constant that sums over all possible labels such that the combined probability is equal to one.

The Gibbs model

The Gibbs random field (GRF) is equivalent to a MRF, but is better suited to finding the maximum a posteriori probability. Instead of expressing distributions on fields as the MRF does, GRFs model context by cliques and data terms (encaptured by one-cliques) [104, 100]. A MRF is a GRF if and only if its configuration follows a Gibbs distribution given by

$$P(f) = \frac{1}{Z} \exp\left(-\frac{U(f)}{T}\right), \tag{3.25}$$

where $U(f)$ is the energy function and T and Z are constants, where the latter is defined as

$$Z = \sum_{f \in F} \exp\left(-\frac{U(f)}{T}\right). \tag{3.26}$$

The energy function $U(f)$ is the sum of clique potentials $V_c(f)$ over all possible cliques $\mathcal{C}$. The GRF is homogeneous if the clique potential is independent of the
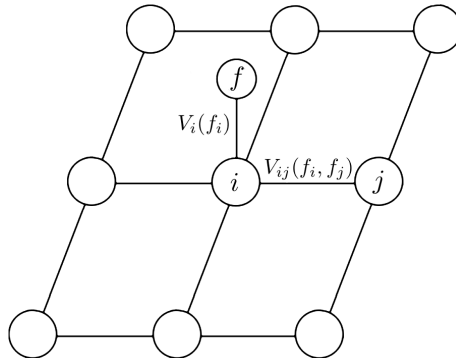
Figure 3.2: The Markov random field illustrated for site i. The cost of assigning
label f to site i is given by minimizing the energy of all possible
labeling configurations.

relative position of the clique c in $\mathcal{S}$. Furthermore, the GRF is isotropic if V_c
is independent on the orientation of c. The energy function $U(f)$ for the Ising
model is given as

$$U(f) = -\left(\sum_{i \in C_1} \alpha_i f_i + \sum_{(i,j) \in C_2} \beta_{ij} f_i f_j\right). \tag{3.27}$$

The single-cite clique potential is thus $V_i(f_i) = -\alpha_i f_i$ for $i \in \mathcal{C}_1$ and the pair-site
potential is $V_{ij}(f_i, f_j) = -\beta_{ij} f_i f_j$ for $(i, j) \in \mathcal{C}_2$. These relations are illustrated
in Figure 3.2. If labels f_i and f_j are the same, then a positive β_{ij} is added to
the energy function enforcing homogeneity, otherwise $-\beta_{ij}$ is added.

In order to generalize to multilabel problems the Potts model is used [105, 106].
The model assumes i) a pixel-wise classification function, such as Bayesian clas-
sification, for the single-clique potentials and ii) the two-clique potentials are
determined as

$$V_{ij}(f_i, f_j) = \beta_{ij}(1 - \delta_k(f_i - f_j)), \tag{3.28}$$

where $\delta_k(f_i - f_j)$ is the Kronecker delta function

$$\delta_k(f_i - f_j)) = \begin{cases} 1 & \text{for} \quad f_i - f_j = 0 \\ 0 & \text{for} \quad f_i - f_j \neq 0, \end{cases} \tag{3.29}$$
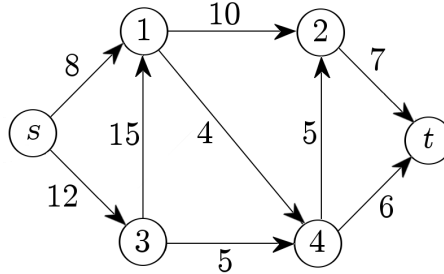
Figure 3.3: An example of a directed graph with source and sink vertices and non-negative edge weights.

Graph cuts

Graph cuts is a framework by which discrete energy minimization problems can be solved. Graph cuts use max-flow (min-cut) algorithms for this purpose, and can for instance be used to solve binary MAP-MRF problems. A graph is defined as a directed graph $\mathcal{G} = (\mathcal{V}, \mathcal{E})$, where $\mathcal{V}$ is the set of vertices and $\mathcal{E}$ the set of edges, with non-negative weights on each edge. The graph contains two special vertices, the source s and sink t [107]. A graph is illustrated in Figure 3.3. The graph can be partitioned such that the vertices $\mathcal{V}$ are divided in two sets S and T, where $s \in S$ and $t \in T$. The cost of the cut is then the sum of all the edge weights going from S to T [107]. Hence the cut with the minimal cost is sought, which according to Ford and Fulkerson [108] is the equivalent to finding the maximum flow of the graph. A binary MRF problem can be formulated as a graph cut problem [107], where the minimal cut corresponds to the minimal possible energy $U(f)$, i.e. the MAP-MRF solution. The graph cut method is guaranteed to find the global optimum solution [107]. Boykov et al. [109] provide an efficient approximate solution using graph cuts for general multilabel MRF problems.

α-expansion

A limitation of the graph cut method is that it only deals with binary label problems. Boykov et al. [109] introduced a solution to this problem by fusion moves, where two sets of labeling $g = \cup g_i$ and $h = \cup h_i$ are fused into the labels $k = \cup k_i$. One of the fusion moves introduced is α-expansion, where the labeling is expanded on label α iteratively. That is, for all labels $\alpha \in \mathcal{L}$, the α value is iteratively compared against all other labels $\mathcal{L} \setminus \alpha$ to solve the binary graph cut

problem. Thus, for all sites $i \in \mathcal{S}$ labeled as $f_i \neq \alpha$ a decision is made whether it is changed to α or not.

Anisotropic MRFs

MRFs can model either an isotropic smoothing constraint, such that all pair-sites are assigned the same smoothing parameter β_{ij}, or the parameter can vary depending on clique orientation, resulting in an anisotropic smoothing. For the anisotropic case a method for determining the influence function on β is required. Grau et al. [110] introduced the use of a structure tensor to incorporate the local information about structure orientation and coherence into the segmentation process, thus defining an anisotropic MRF. It is based on the coherence-enhancing filtering of Weickert [111] and the nonlinear diffusion filters by Perona and Malik [112]. Anisotropic diffusion was also introduced by Black et al. [113]. In Grau et al. [110], the influence function is described such that the neighborhood influence on the voxel classification is weighted by the local structure characteristics at its location. The structure tensor for an m dimensional image y is defined as

$$J(y, \sigma, \rho) := K_\rho * (\nabla(K_\sigma * y) \otimes \nabla(K_\sigma * y)), \tag{3.30}$$

where K_σ and K_ρ are Gaussian kernels with standard deviations σ and ρ, and $\otimes$ is the tensor product. The matrix in Equation (3.30) is a symmetric positive semidefinite matrix [111], where the eigenvalues provide a measure of the average intensity variation in the eigenvector directions, and ρ is a scale parameter [110]. In other words, the eigenvalues $\mu_1, ..., \mu_m$ of the structure tensor matrix provide information of the amount of anisotropy. A coherence function is defined in [111] as

$$\kappa := \sum_{i=1}^{m-1} \sum_{j=i+1}^{m} (\mu_i - \mu_j)^2, \tag{3.31}$$

which tends to zero for structures that are isotropic and becomes large for differing eigenvalues. This information can be incorporated into the influence function $I(i, j)$ which modulates β_{ij}, thus relating it to the structure in the image. For this purpose Grau et al. [110] propose a diffusion tensor D. The diffusion tensor has the same eigenvectors as the structure tensor, and the eigenvalues of the diffusion tensor are small constants except for the eigenvalue associated with the main direction, depending on the coherence value κ in Equation (3.31). The eigenvalues are calculated as

$$\lambda_m = \begin{cases} \alpha, & \text{if } \kappa = 0 \\ \alpha + (1 - \alpha) \exp\left(-\frac{C}{\kappa}\right), & \text{otherwise} \end{cases} \tag{3.32}$$

$$\lambda_i = 1 - \lambda_m, \qquad i = 1...m - 1, \tag{3.33}$$

where C is a threshold parameter, and α is chosen such that eigenvalues will be approximately equal where coherence is small (isotropic coherence tensor D), and such that the coherence tensor D becomes directional where coherence is great [110]. The influence function is then defined as

$$I(i,j) = \frac{\bar{r}_{ijN} D \bar{r}_{ijN}^{T}}{|\bar{r}_{ij}|}, \qquad (3.34)$$

where $\bar{r}_{ijN}$ is a normalizing vector joining i and j. The influence value approximates an isotropic MRF where coherence is small, and is maximum when the voxels i and j are aligned in the dominant structure orientation of i [110].

3.2.3   Active appearance models

An active appearance model (AAM) is a generative model which can represent both shape and texture variability of a training set, where texture refers to the intensity patterns of an image patch. AAMs have proven useful for segmenting a variety of anatomical structures within medical image analysis [114]. In the work of this thesis, images of objects with known structure are considered, and for this type of data AAMs are applied for segmentation. AAMs were first introduced by Cootes et al. in [115, 101], and the following section will follow the notation given there.

AAM training

In order to construct the model, a training set consisting of images with manually placed landmark points is required, thus making the learning of the model supervised. The landmarks are then aligned by Procrustes analysis [116, 117], i.e. the points are scaled, rotated and translated such that they become superimposed onto the same coordinate frame of reference. The statistical model for both shape and texture is then generated by applying principal component analysis (PCA), see Section 3.3.5, to the set of vectors that describe the shape and texture separately. Using the shape model, described in [118], an example of a shape can be approximated by

$$\mathbf{s} = \bar{\mathbf{s}} + \mathbf{\Phi}_s \mathbf{b}_s, \qquad (3.35)$$

where $\bar{\mathbf{s}}$ is the mean shape vector, $\mathbf{\Phi}_s$ is a set of orthogonal modes of shape variation from the PCA and $\mathbf{b}_s$ is a vector of shape parameters [119]. For the texture model, the training images are first warped, using a piecewise affine transformation, such that the landmarks match the mean shape $\bar{\mathbf{s}}$. The intensity

values of the patch, covered by the shape-normalized region, are then sampled. PCA is again applied, and a linear model constructed as

$$\mathbf{t} = \bar{\mathbf{t}} + \mathbf{\Phi}_t \mathbf{b}_t, \tag{3.36}$$

where $\bar{\mathbf{t}}$ is the mean intensity vector, $\mathbf{\Phi}_t$ is a set of orthogonal modes of intensity and $\mathbf{b}_t$ is a set of intensity parameters. The shape and intensity model are combined by concatenating the vectors $\mathbf{b}_s$ and $\mathbf{b}_t$ and applying once again a PCA to obtain the appearance model given by

$$\mathbf{b} = \begin{pmatrix} \mathbf{W}_s \mathbf{b}_s \\ \mathbf{b}_t \end{pmatrix} = \begin{pmatrix} \mathbf{\Phi}_{c,s} \\ \mathbf{\Phi}_{c,t} \end{pmatrix} \mathbf{c} = \mathbf{\Phi}_c \mathbf{c}, \tag{3.37}$$

where weights for each shape parameter are given by the diagonal of $\mathbf{W}_s$ to compensate for difference in units between the shape and intensity model. The weights are typically determined by the square root of the ratio between the sums of the texture and shape eigenvalues [114]. From the combined appearance model, shape and texture can be expressed as functions of $\mathbf{c}$

$$\mathbf{x} = \bar{\mathbf{x}} + \mathbf{\Phi}_s \mathbf{W}_s^{-1} \mathbf{\Phi}_{c,s} \mathbf{c} \quad , \quad \mathbf{t} = \bar{\mathbf{t}} + \mathbf{\Phi}_t \mathbf{\Phi}_{c,t} \mathbf{c}. \tag{3.38}$$

AAM search

Given the appearance model, an unseen image can be interpreted and the modeled object segmented. This is done iteratively by updating the model parameters and comparing the current model image $\mathbf{t}_{\mathrm{model}}$ and corresponding patch from the unseen image $\mathbf{t}_{\mathrm{image}}$. Ideally the procedure should find the ground truth shape in the unseen image, given an accurate prior estimate of the position. The iterative search can be summarized by the following steps:

1. Image texture $\mathbf{t}_{\mathrm{image}}$ and model texture $\mathbf{t}_{\mathrm{model}}$ are calculated.

2. The residual vector $\mathbf{r}(\mathbf{p}) = \delta\mathbf{t}(\mathbf{p}) = \mathbf{t}_{\mathrm{image}}(\mathbf{p}) - \mathbf{t}_{\mathrm{model}}(\mathbf{p})$ and current error $E = |\mathbf{r}^2|$ are evaluated.

3. Displacements $\mathbf{p}$ of landmarks that minimize the current error are found by an optimization approach.

4. Steps 1 to 3 are repeated until convergence.

Several methods exist for predicting parameter updates, including linear regression [115] and a fixed Jacobian matrix estimate [101]. The implementation of the Jacobian approach is simpler than the linear regression approach. It is also faster to compute and more memory efficient [114]. Alternatives to AAM are constrained local models [120], and Random forest regression voting [121, 122].

3.2.4 Evaluation of segmentation results

For the purpose of quantitative analysis, the segmentation accuracy is critical. In order to determine the accuracy, a ground truth is required. Such a 'golden standard' is hard to define and remains an unsolved problem. In medical image analysis the ground truth is typically determined by manual segmentations performed by experts. Several issues arise when a manual segmentation is used as ground truth, including intra and inter-observer variability. Even though a reliable manual segmentation is available, it is still questionable if the results are accurate in relation to the object measured. Image noise and artifacts can misguide a manual segmentation and partial volume effects are difficult to handle. The precise interface boundary of two materials is difficult to determine if the image resolution is not adequate. With these issues in mind, if a valid ground truth is available, there are several ways to determine the accuracy of the segmentation, some of which are discussed in the following sections.

Similarity coefficients

Given a ground truth segmentation V_{ref}, several metrics exist to evaluate the quality of the predicted segmentation, V_{seg}, including the Dice similarity coefficient (DSC) [123], the Jaccard similarity coefficient (JSC) [124] and overlap fraction (OF). The DSC measures the spatial overlap between two segmentations, the target regions V_{ref} and V_{seg}, and is defined by

$$\mathrm{DSC} = 2\frac{|V_{\mathrm{seg}} \cap V_{\mathrm{ref}}|}{|V_{\mathrm{seg}}| + |V_{\mathrm{ref}}|}, \tag{3.39}$$

where $\cap$ is the intersection. JSC is defined as

$$\mathrm{JSC} = \frac{|V_{\mathrm{seg}} \cap V_{\mathrm{ref}}|}{|V_{\mathrm{seg}} \cup V_{\mathrm{ref}}|}, \tag{3.40}$$

where $\cup$ is the set union. The overlap fraction is finally defined as

$$\mathrm{OF} = \frac{|V_{\mathrm{seg}} \cap V_{\mathrm{ref}}|}{|V_{\mathrm{ref}}|}. \tag{3.41}$$

Confusion matrix

The DSC, JSC and OF measures can be used when the segmentation problem is a binary one. For evaluation of segmentation including several classes other

Table 3.1: A confusion matrix for linking true labels with predicted ones.

		Predicted label		
		Label_1	...	Label_n
	Label_1	M_{11}	...	M_{1n}
True label	...	...	...	...
	Label_n	M_{n1}	...	M_{nn}

evaluation methods need to be considered. On such method is calculating the confusion matrix. The confusion matrix is also discussed in Section 3.3.6. The matrix is a table that illustrates the performance of a segmentation by comparing the actual class label of a pixel and the predicted one from the segmentation. An example of a confusion matrix for an image with n labels is shown in Table 3.1 where M_{ij} represents the number of pixels segmented as label number i and actually belonging to the true label j.

3.3   Statistical learning

Statistical learning has been used extensively for segmentation, feature selection and classification for food product quality evaluation [22]. Bayesian theory for instance provides a generic, mathematically rigorous probabilistic approach to inference. This section will present the topics of statistical learning relevant for the thesis work. These include novelty detection, model selection based on the bias-variance trade-off, classification by support vector machines and dimensionality reduction by principal component analysis.

3.3.1   Novelty detection

In novelty detection (also known as anomaly- and outlier detection), the classification problem is to identify whether an observation is part of the data or is in fact unknown. The aim is to assign an abnormal label to anomalies within known normal observations. Novelty detection can thus be described as a one-class classification problem. To determine whether new observations are truly abnormal, some sort of distance measure is required along with a threshold for decision making. Novelty detection is relevant for many applications, for instance in medical image analysis where diseases need to be identified from image data [125, 126, 127], foreign object detection in food products [128, 32] and video surveillance for crowd analysis [129, 130, 131]. Typically in situations where novelty detection is applied the normal observations are available and only a few or none of the abnormal are. In a practical setting it is difficult to foresee all possible types of anomalies and therefore the novelty detection scheme is well suited. Pimentel et al. [132] describe a model of normality $M(\theta)$, where θ are the parameters of the model. From the model, novelty scores $z(\theta)$ are calculated for unseen test data x, where large novelty scores correspond to increased abnormality from the normal model. To determine whether the data truly is abnormal $(+)$ or normal $(-)$ a threshold is determined $z(x) = k$ such that

$$x = \begin{cases} + & \text{if} \quad z(x) \geq k \\ - & \text{if} \quad z(x) < k. \end{cases} \qquad (3.42)$$

Therefore a decision boundary is determined by $z(x) = k$. The three main steps to consider for novelty detection are the methods for modeling normality $M(\theta)$, tuning of the model parameters θ, and choosing a threshold value k.
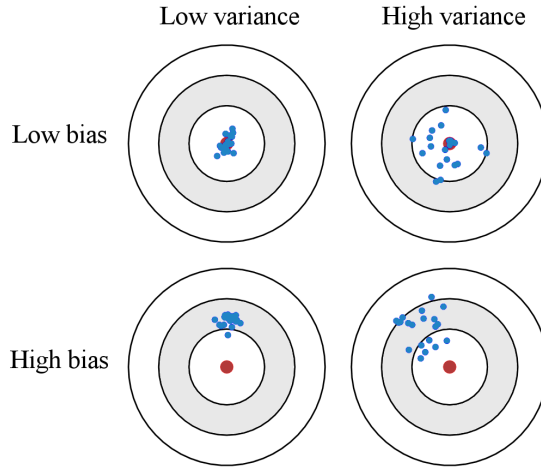
Figure 3.4: Visualization of bias and variance.

3.3.2 The bias-variance tradeoff

Most classification problems require more complex models than the novelty detection scheme previously presented. As model complexity increases, it is important to consider issues in regards to model over-fitting and under-fitting. Given a training set of observations $X = x_1, ..., x_n$ with associated real values $Y = f(X) + \epsilon$, where $\epsilon \in \mathcal{N}(0, \sigma_\epsilon^2)$ is noise with zero mean and variance σ^2, a good learning model $\hat{f}(x)$ will have minimal mean squared error (MSE) $(Y - \hat{f}(X))^2$ [95]. Since Y contains noise, no model will be perfect and this is what is called the irreducible error σ_ϵ^2. The expected prediction error of a model can be decomposed into the irreducible error, bias and variance as given by [95]

$$\text{E}[(Y - \hat{f}(X))^2] = \text{Bias}[\hat{f}(X)]^2 + \text{Var}[\hat{f}(X)] + \sigma_\epsilon^2, \tag{3.43}$$

where $\text{Bias}[\hat{f}(x)] = \text{E}[\hat{f}(x)] - f(x)$ and $\text{Var}[\hat{f}(x)] = \text{E}[(\hat{f}(x) - E[\hat{f}(x)])^2]$. The expectation is estimated for different combinations of the training set. Bias describes the average error of the model while variance describes the variance in the predictions of the model. In other words, bias indicates the average difference between the expected prediction of a model and the true values. Variance on the other hand measures how much the predictions of observations vary from the actual value. Models with low bias and high variance get a correct prediction on average with high variability (over-fitting). Models with high bias and low variance have low variability in the predictions but generally result in a wrong prediction (under-fitting). This is illustrated in Figure 3.4. Model com-

plexity greatly influences the so-called *bias-variance tradeoff*. As the complexity increases, the variance tends to increase and bias tends to decrease. When model complexity decreases the opposite behaviour occurs [95].

3.3.3   Model selection

In order to select an appropriate model the available data can be randomly split into three parts; training set, validation set and test set. Typically, the training set is the largest of the three and is used to train the model on a range of parameters. The prediction error of the models is then calculated using the validation set and the best option selected. Finally, the test set is used to estimate how well the resulting model works. This procedure is adequate for well-conditioned problems where there are enough observations available. For datasets where the number of samples are limited a common and simple approach for model selection is k-fold cross-validation [133]. The cross-validation procedure splits the data X randomly into k equal parts $X_1, X_2, ..., X_k$. The model is then trained and tested k times; each time $t \in \{1, 2, ..., k\}$ it is trained on the parts of X excluding X_t and tested on X_t. The accuracy is then estimated as the overall number of correct classifications, divided by the number of observations in the dataset [133]. The cross-validation method can be used to avoid over-fitting data.

3.3.4   Support vector machines

Support vector machines (SVM) is a non-probabilistic binary classifier, and is commonly used as a supervised learning model. When given a set of training examples, where all observations are labelled one of two classes, SVM will assign a label to new observations. SVMs are a generalization of linear decision boundaries called optimal separating hyperplanes, and extends to cases where classes are non-separable. The support vectors of SVM are a set of vectors in the training data that are closest to the decision boundary [102]. An excellent description of SVM is given by Hastie et al. [95] and the following review of SVM will be based on their terminology and notation. The training data consists of n observations $x_1, ..., x_n$ with corresponding output values $y_1, ..., y_n$ where $x_i \in \mathbb{R}^p$ and $y_i \in \{-1, 1\}$. Given a hyperplane $f(x) = x^T \beta + \beta_0 = 0$, where β is a weights vector and β_0 is the bias, a classification rule can be determined as

$$G(x) = \text{sign}[x^T \beta + \beta_0]. \tag{3.44}$$

For every training point x_i, the function $f(x)$ gives the signed difference from the point to the hyperplane. When the classes are separable there exists a hyperplane
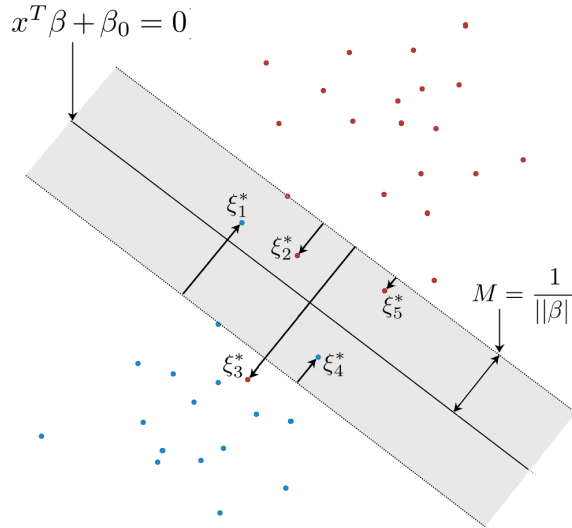
Figure 3.5: Support vector classifier for an inseparable case. The margin is denoted by the dotted line, the decision boundary by a solid line, and the support vectors are labeled as ξ_j^*.

which creates the largest margin between the training points for the two classes. This is called the optimal separating hyperplane, where $f(x) = x^T\beta + \beta_0$ with $y_i f(x_i) > 0 \;\; \forall i$. The optimization problem can be defined as

$$\min_{\beta,\beta_0} ||\beta|| \quad \text{subject to } y_i(x_i^T\beta + \beta_0) \geq 1, \;\; i = 1, ..., N, \tag{3.45}$$

The margin of the hyperplane is $M = 1/||\beta||$ and can be maximized for separable data by Equation (3.45) which is a convex optimization problem.

For the case where the data is non-separable, SVM seeks to maximize the margin M by allowing for some points in the training set to be misclassified. Hence slack variables $\xi = (\xi_1, .., \xi_N)$ are introduced and the support vector classifier becomes

$$\min ||\beta|| \;\; \text{subject to} \;\; \begin{cases} y_i(x_i^T\beta + \beta_0) \geq 1 - \xi_i \; \forall i, \\ \xi_i \geq 0, \; \sum \xi_i \leq \text{constant}. \end{cases} \tag{3.46}$$

That is to say, the margin of the support vector classifier is maximized by the support vectors ξ_i where their total distance is determined by the constant. Figure 3.5 illustrates the support vector classifier for the non-separable case.

The solution can be found by Lagrangian optimization if rephrased as

$$\min_{\beta, \beta_0} \frac{1}{2} ||\beta||^2 + C \sum_{i=1}^{N} \xi_i \tag{3.47}$$

$$\text{subject to } \xi_i \geq 0, \ y_i(x_i^T \beta + \beta_0) \geq 1 - \xi_i \ \forall i, \tag{3.48}$$

where C is a cost parameter that replaces the constant in Equation (3.46). If $\hat{\beta}$ and $\hat{\beta}_0$ are the solutions then the decision function becomes

$$\hat{G}(x) = \text{sign}[x^T \hat{\beta} + \hat{\beta}_0]. \tag{3.49}$$

Equation (3.46) describes a linear support vector classifier, which can be expanded by enlarging the feature space through basis expansions. These include polynomial- or spline expansions. Given the basis functions $h_m(x)$, $m = 1, ..., M$, the input features become $h(x_i) = (h_1(x), ..., h_M(x_i))$, $i = 1, ..., N$, and fitting the SVM will result in a non-linear decision boundary in the original feature space $\hat{f}(x) = h(x)^T \hat{\beta} + \hat{\beta}_0$. The tuning of parameter C becomes crucial in the enlarged feature space, as too large a value can cause over-fitting, while a lower value will result in a smoother decision boundary. C can be determined by for instance cross-validation.

As for all learning techniques, SVMs both have several advantages and disadvantages. The kernel transformation allows for non-linear decision boundaries, adapting the SVM to non-linearly separable data. The cost parameter and kernel parameters of the SVM can be tuned to avoid over-fitting. Since SVMs are defined by a convex optimization problem they can be easily trained, efficiently calculated and give a unique solution. SVMs also scale well to high dimensional data. SVMs are well-suited for small training sets, in contrary to random forests [134] and deep neural network algorithms [135] that require larger training sets. The tuning of several parameters for the kernel function of SVM can however be difficult, and increases the complexity compared to the linear variety. The extension of multiclass SVMs exists [136]. However, the conventional approach to multiclass classification is building a 'one-against-all' SVM for each class, increasing the computational cost.

3.3.5   Principal component analysis

For high dimensional data, visualization and interpretation becomes difficult. In order to obtain a meaningful representation of the data, a reduction of the number of variables can be performed. This can be achieved by orthogonal transformations, which convert a set of variables into a new space by linear transformation, preserving a symmetric inner product. One such transform is
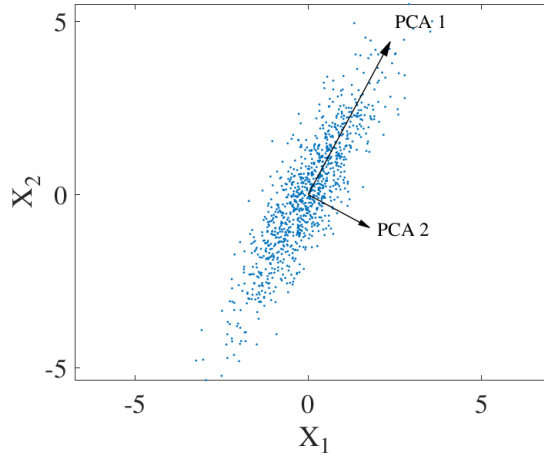
Figure 3.6: The first two principal components of data $\mathbf{X}$. The first principal component direction maximizes the largest variance possible in the data and the second principal component is orthogonal to the first.

principal component analysis (PCA) which converts a set of observations of possibly correlated variables into a set of values of linearly uncorrelated variables called principal components. The principal axis of the new coordinate system thus maximizes the variance of the projected data. Each sequential axis is then ordered in decreasing variance. Each principal component is a linear combination of all of the initial variables. PCA is an unsupervised and exploratory method, and can recover low-dimensional structure in high-dimensional spaces. Given an $N \times p$ matrix $\mathbf{X}$, the singular value decomposition (SVD) is given by [95]

$$\mathbf{X} = \mathbf{U}\mathbf{D}\mathbf{V}^T, \tag{3.50}$$

where $\mathbf{U}$ and $\mathbf{V}$ contain the p orthonormalized eigenvectors for the p largest eigenvalues of $\mathbf{X}\mathbf{X}^T$ and $\mathbf{X}^T\mathbf{X}$ respectively [137]. The singular values of $\mathbf{X}$ are the diagonal elements of $\mathbf{D}$, which are the non-negative square roots of the eigenvalues of $\mathbf{X}^T\mathbf{X}$. The principal components of the centered matrix $\mathbf{X}$ can be expressed by the SVD as

$$\mathbf{X}^T\mathbf{X} = \mathbf{V}\mathbf{D}^2\mathbf{V}^T. \tag{3.51}$$

The principal component directions or loadings v_j of $\mathbf{X}$ are thus the columns of $\mathbf{V}$ and the principal components are expressed as $\mathbf{z}_j = \mathbf{X}v_j$. Figure 3.6 shows the first two principal components for a multivariate normal distribution. Variants of PCA are the sparse principal component analysis (SPCA) and kernel PCA. Instead of each principal component being a linear combination of all

Table 3.2: The confusion matrix relating true values to predicted ones.

		Prediction condition	
		Positive	Negative
True condition	Positive	TP	FN
	Negative	FP	TN

the variables, SPCA aims to drive some loadings to zero to provide a sparse representation while still aiming for maximum variance. The sparse loading can be obtained with lasso (L_1) penalties and elastic net (L_1 and L_2) penalties [95]. PCA is a linear transformation, however it can be done with a non-linear mapping called kernel PCA. Kernel PCA first expands the variables by non-linear transformations and applies PCA to the transformed feature space [95].

3.3.6 Evaluation of classification results

When a classification is performed, an evaluation of the results is essential. The results from a binary classification are grouped into four decisions as seen in Table 3.2, true positive (TP) (observations correctly classified as positive), true negative (TN) (observations correctly classified as negative), false positive (FP) (observations incorrectly classified as positive) and false negative (FN) (observations incorrectly classified as negative). For an ideal classifier all n observations would be classified as true positives or true negatives. However, in most settings some observations will be incorrectly classified and the classification rate is defined as

$$CR = (TN + TP)/n = (TN + TP)/(N + P),\qquad(3.52)$$

where P and N are the number of actual positive and negative instances, respectively. The threshold selected for determining whether an observation is positive or negative greatly influences the performance of the classifier. The threshold must therefore be carefully selected, making a trade-off between the acceptable false positive rate and false negative rate. Depending on the application, it may be more critical to minimize one than the other.

3.3.6.1 Sensitivity, specificity and accuracy

To further evaluate the classification results, several statistical measures are defined. The true positive rate (TPR) (also known as sensitivity) is a measure
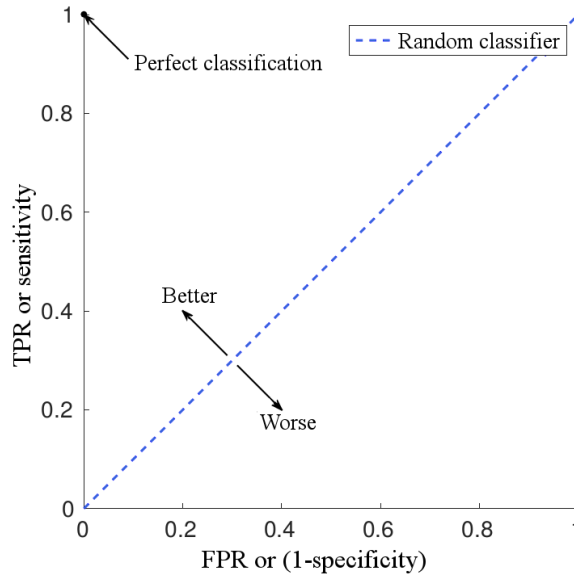
Figure 3.7: Receiver operating characteristic for a random classifier. An ideal classifier is illustrated be the point in the upper left corner.

of the proportion of positives (P) that are correctly classified, TPR=TP/P= TP/(TP+FN). Similarly, the true negative rate (TNR) (also called specificity) measures the proportion of negatives (N) correctly classified, TNR=TN/N= TN/(TN+FP). The receiver operating characteristic (ROC) curve is a useful tool to evaluate the effect of varying the threshold of the binary classifier. The curve plots the TPR (sensitivity) as a function of the false positive rate (FPR) (1-specificity) for a range of decision threshold values. The ROC for a random classifier is shown in Figure 3.7. How well a classifier performs is either determined by the area under the curve (AUC) or the minimal distance to perfect classification.

This concludes the methodological overview related to the work of this thesis.

Part II

Summary of scientific contributions

Segmentation framework for multimodal X-ray images

This chapter presents a segmentation framework based on the methodology discussed in Chapter 3. The framework was developed to segment µCT data obtained from a synchrotron source. The framework presented in this chapter was applied for the data analysis in Papers A and B.

The papers demonstrate the application of GBI µCT in order to determine heat induced structural changes in meat products. Due to the brilliance and spatial resolution obtained from synchrotron sources, high contrast of soft tissue is seen [48, 138], making it possible to distinguish between the protein structure, gel phase and connective tissue of the samples. Paper A presents a quantitative analysis of meat emulsions before and after cooking, and how the use of different fat types affects the emulsion stability in terms of structure homogeneity and cooking loss. Paper B investigates the heat induced structural changes in meat by the use of X-ray phase-contrast tomography. The paper analyzes the decrease in muscle volume due to heat denaturation, along with the increase in connective tissue volume and cooking loss. The papers serve as a technological demonstrator, and illustrate how the GBI technology combined with advanced segmentation methods can be used for novel analysis of food structures.
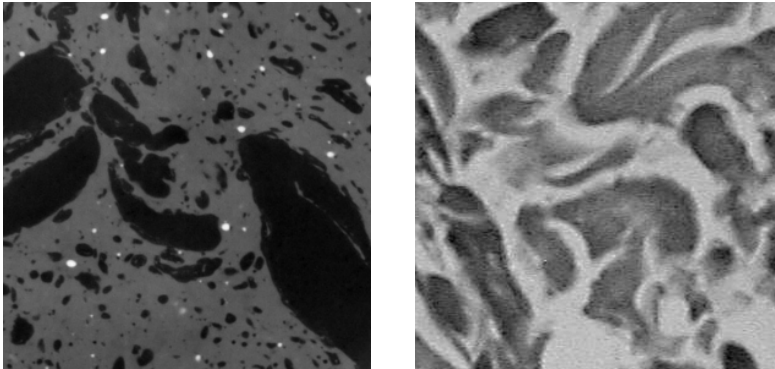
Figure 4.1: Examples of blob like (left) and thin structures (right).

In order to achieve the quantitative results illustrated in both papers a segmentation scheme was proposed that both takes into account the multimodal and spatial nature of grating-based tomography. Despite the high brilliance of the synchrotron source, the data acquisition is prone to noise and measurement artifacts, similar to other X-ray measurements. Intensity gradients, streak- and ring artifacts and partial volume effects are some of the more noticeable errors. Thus, simple threshold segmentation does not suffice for reliable segmentation. In addition to noise, the data is multimodal adding complexity to the segmentation problem. For these reasons the MRF framework was utilized, in order to incorporate a smoothing constraint for the segmentation problem. Additionally, MRFs can be configured with isotropic or anisotropic smoothing, adding to the flexibility of the segmentation procedure. The application of energy minimization via graph cuts to µCT data has previously been demonstrated in a number of papers [139, 80, 140, 110, 141].

4.1　Segmentation framework

For the purpose of segmenting the µCT data presented in this thesis, a segmentation framework was developed based on the MRF framework. The tool was written in Matlab R2014b in order to provide a low barrier of entry for users with non-programming backgrounds. The tool provides means for segmenting 2D and 3D data. Estimation of the parameters for the Bayesian labeling prior of the first-order MRF can either be determined by Expectation-Maximization as described in Section 3.1.4, or by estimating them from manually selected regions. When EM is chosen, the number of Gaussian distributions to be fitted is

required as an input. In addition, the segmentation framework can both handle univariate data as well as multimodal. For data containing thin structures (such as connective tissue in muscles) the option for applying an anisotropic β constant is provided by calculating the structure tensor as described in Section 3.2.2. This method for anisotropic smoothing was based on the work described in Grau et al. [110]. In order to adapt to multimodal data, the structure tensor is calculated as either i) a weighted average of the three separate tensors for all modalities or ii) by applying PCA and using the obtained coefficients of the first principal component as weights for the tensors. Furthermore, the segmentation framework allows for multiclass labeling by α-expansion as described by Boykov et al. [109]. Due to the large data volumes produced by synchrotron GBI, the segmentation framework also provides a method for volume patch segmentation. Finally, the segmentation results can be visualized both by a labelling map and histogram analysis. The segmentation framework was presented at the 3rd Annual Conference of the COST Action [142].

To demonstrate the anisotropic smoothing of the segmentation framework two examples are given, for the structures shown in Figure 4.1. Figure 4.2 shows the result for the isotropic- and anisotropic smoothing constraint for both the blob like and thin structures, for varying β's. The blob like structures are fat globules and salt particles in meat emulsions, while the thin structures are histology results of a tissue sample. Figure 4.3 illustrates the percent error for varying β's for the isotropic- and anisotropic segmentation of the same structures. Although the anisotropic segmentation performs better on both types of structures, the error difference is significantly smaller for blob like structures. This is important to note when designing the segmentation procedure. GBI data is quite complex, and if all the features of the framework are to be used (i.e. anisotropy, 3D, multi-label and multimodal) the problem becomes computationally heavy. Therefore, a tradeoff should be considered when deciding which features to include in the segmentation pipeline.

Main results

The segmentation method was applied for data analysis in Papers A and B. Segmentation accuracy was determined by constructing a confusion matrix based on ground truth labels annotated by experts. In Paper A all three modalities from GBI were included in the segmentation pipeline, and an isotropic smoothing constraint chosen. The results are illustrated in Figure 4.4. Both the raw and heated treated sample volumes were segmented which provided a labeling map for further quantification of microstructural properties. Apart from increased segmentation accuracy compared to univariate MRF segmentation, the multivariate segmentation method allowed for identification of new phases
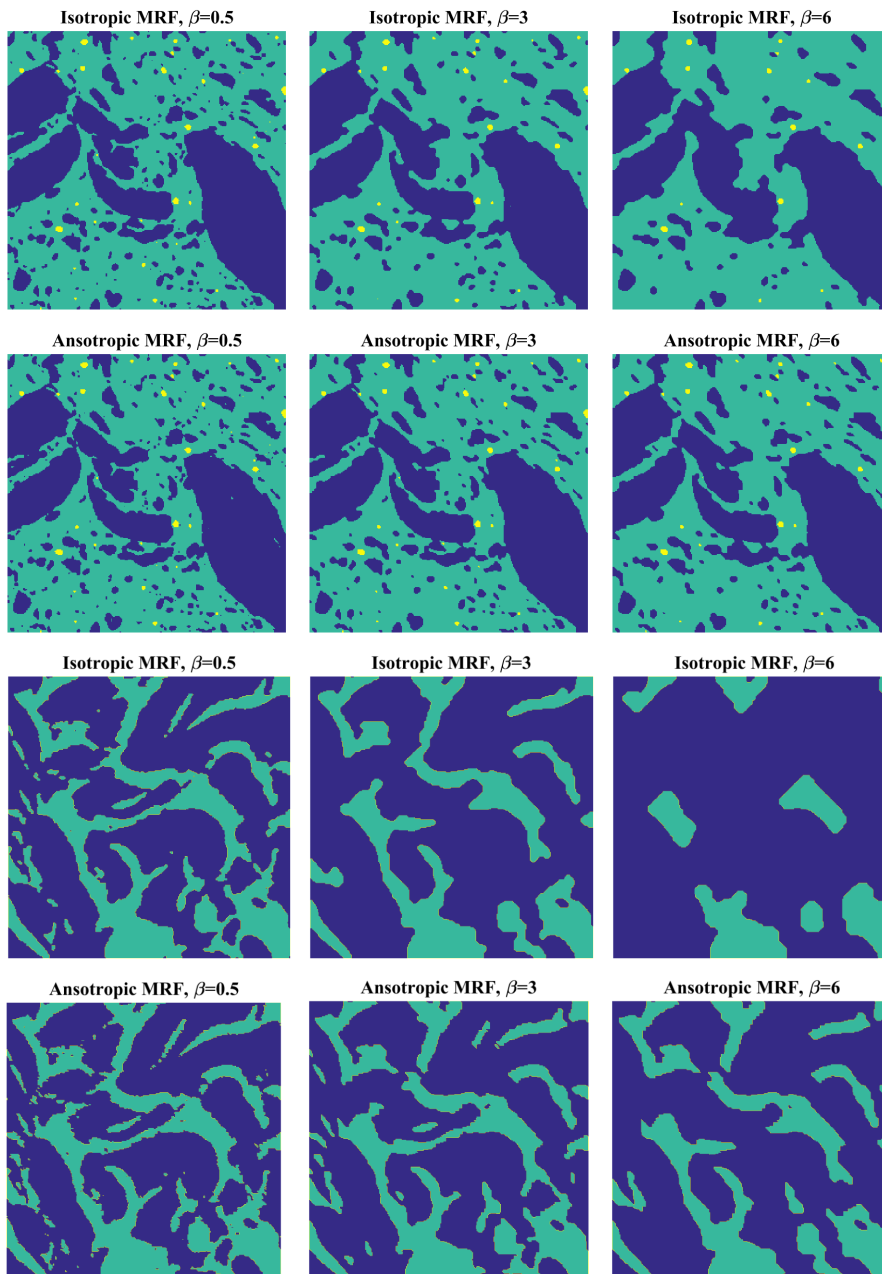
Figure 4.2: Comparison of isotropic- and anisotropic MRF segmentation for blob like (top two rows) and thin structures (bottom two rows).

(a) Blob like structures.   **(b)** Thin structures.
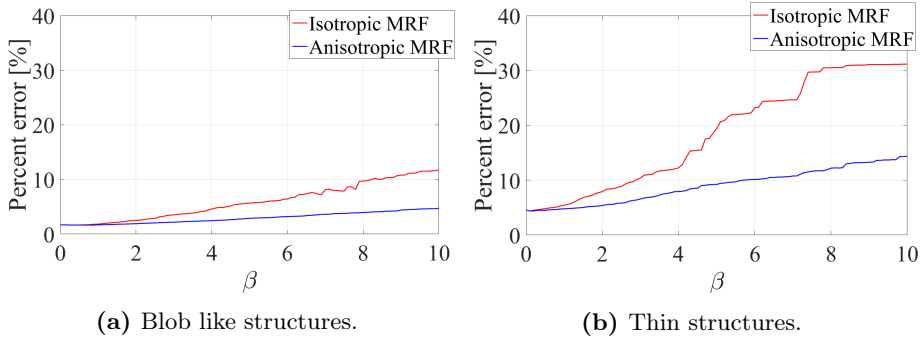
Figure 4.3: Segmentation error (incorrectly classified pixels) as a function of β for isotropic- and anisotropic MRF segmentation of blob like and thin structures.

in the emulsion. In Paper B only the phase-contrast modality was included in the segmentation stage, as the contrast in this modality was superior compared to the absorption and dark-field modalities. The presence of the thin structures of the connective tissue required an anisotropic smoothing constraint. This resulted in a better segmentation of the connective tissue structures, allowing for a quantitative evaluation of their volume increase due to heat treatment.

Main contributions

To summarize, the main contributions of the work include:

- Development of a segmentation framework based on the methodology given in Chapter 3.

- Extension of the anisotropic smoothing procedure described in Grau et al. [110] to multimodal data.

- Visualization of the segmentation results through histogram analysis.

- Application of the segmentation scheme to GBI µCT data.

- Evaluation of the segmentation accuracy obtained.
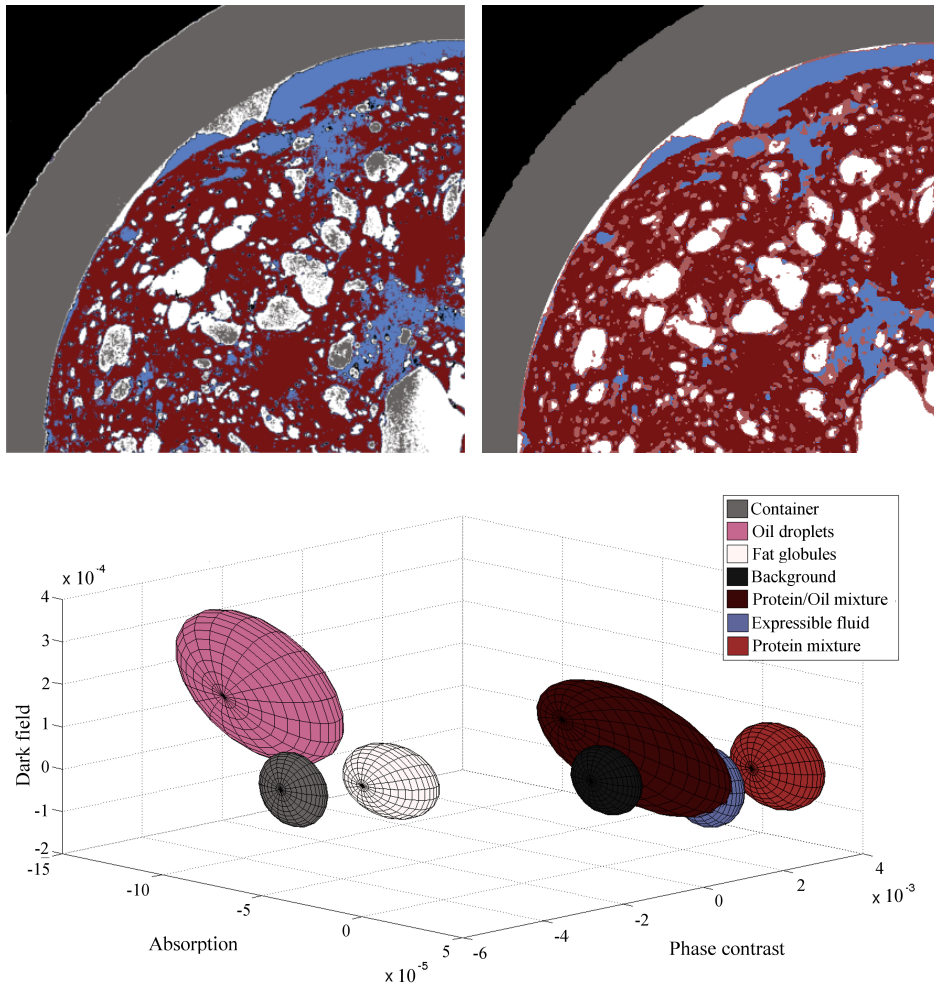
Figure 4.4: Comparison of phase-contrast threshold (top left) and isotropic multimodal MRF segmentation (top right). The multivariate histogram is illustrated by the covariance ellipsoids of the segmented phases (bottom).

3D microstructural changes in meat products

The discipline of food quality analysis is both broad and diverse. Topics range from determining the effect of freezing beef [143, 144] to the relationships between fruit maturity, ripening and quality [145]. Recently, the role of microstructure in food quality has gained increased attention [58, 146]. Furthermore, X-ray μCT has gained specific attention as a technique capable of imaging the internal microstructure in food [26]. This chapter presents the application of GBI for quantitative analysis of the microstructure of meat products. The analysis is performed to determine the effects of heat treatment, i.e. how it affects the stability and cooking loss of the product. This is the subject of both Papers A and B. Both papers serve as a technological demonstrator for combining GBI with advanced analysis methods, in order to obtain novel extraction of important parameters of the cooking process.

5.1   Heat-induced microstructural changes in meat

Cooking of meat immediately influences changes in its microstructure, causing extensive structural changes of the meat proteins [147]. Tornberg [148] discussed

the structural changes on cooking in whole meat and comminuted meat products, and how the procedure alters the water-holding capacity and texture of meat. As both directly influence the palatability and quality of the product, determining the extent of their change is of great value. Damez & Clerjon [149] provide an overview of techniques to quantify and predict meat and meat product quality attributes using electromagnetic waves. These include microwaves, magnetic resonance imaging (MRI), infrared and ultra-violet light and X-ray interactions. Both MRI and X-ray provide sufficient penetration power allowing for 3D imaging of the internal structures in a sample. The advances in X-ray phase-contrast µCT imaging at synchrotron sources have allowed for investigation of fatty acid composition of the fat-fraction, and variations of density in the meat fraction [48]. Inspired by these results, Papers A and B investigate the heat-induced changes in whole meat and meat emulsions, determining quality traits such as cooking-loss and percent object volumes. The measurements were carried out using a grating interferometer at the TOMCAT beamline at the Swiss Light Source. The X-ray µCT setup provides the means for re-measuring the same sample, thus allowing for the samples to be measured both prior to and after cooking.

5.2   3D microstructural parameters

The synchrotron data was segmented with the segmentation framework discussed in the previous chapter. From the acquired label maps, quantitative parameters were extracted. An important measure is the percent object volume (POV). The POV quantifies the volumetric proportion of each element in a segmented 3D volume. Given that a segmented volume has labels $l \in \mathcal{L} = \{\mathcal{L}_1, ..., \mathcal{L}_n\}$, where n is the number of labels, the POV for label i is computed as

$$POV_i = \frac{V_i}{V},\tag{5.1}$$

where V_i is the volume consisting of labels i and V is the total volume. The POV can be used to estimate for example the cooking loss.

For the emulsion analysis, labeling individual fat globules in the emulsion is the basis for further quantification of their stability. Connected component labeling is a common task in image analysis. Pixels belonging to the same component in a binary image are labeled such that all pixels of that component have the same label. Components can be wrongfully connected due to image noise and digitization errors. A common approach to solving the problem is by using the watershed algorithm [150] and morphological operations. Standard parameters to quantitatively analyze three dimensional spatial structures include the vol-
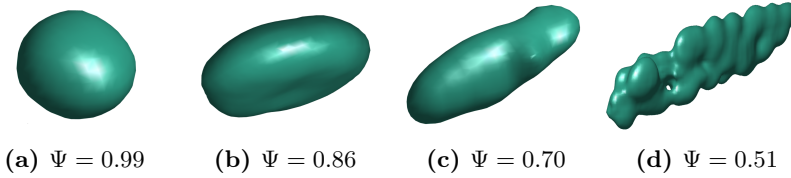
(a) $\Psi = 0.99$ **(b)** $\Psi = 0.86$ **(c)** $\Psi = 0.70$ **(d)** $\Psi = 0.51$

Figure 5.1: Objects of varying sphericity.

ume, surface area and mean width. These parameters are called Minkowski functionals [151]. Due to the nature of X-ray imaging, the measurements of real objects are digitized by the detector. For a 2D image this results in a pixel grid and for a 3D image the data is digitized on a voxel grid. In order to assess quantitative parameters of the object imaged, an estimate of the digital geometry is necessary [152]. These estimates should reflect the true quantitative properties of the object. Legland et al. [151] proposed a reconstruction of binary structures in 2D and 3D images as complexes of convex cells. Additionally, the computation of Minkowski measures as approximations based on the reconstructions was described, along with an algorithmic implementation. In addition to the surface area, volume and average structure thickness, the sphericity of the globules is also of interest. Wadell defined sphericity Ψ as a measure of how round an object is [153]. It is defined as

$$\Psi = \frac{\pi^{1/3}(6V_p)^{2/3}}{A_p},\tag{5.2}$$

where V_p is the object volume and A_p is the surface area. A sphere has $\Psi = 1$ and objects other than a sphere will have $0 < \Psi < 1$. The sphericity of fat globules in emulsions is an important measure, as it gives insight to the stability of the emulsion structure [154]. Figure 5.1 shows several fat globules of differing sphericity. Finally, a measure of the degree of anisotropy (DA) is commonly calculated to describe the degree of 3D asymmetry in a structure [155, 156]. The DA is a geometrical measure defined as the ratio of the maximal and minimal radius of the mean intercept length (MIL) ellipsoid [156]. In 3D the MIL is determined as the ratio between a test line sent through the 3D volume at a given angle, and the number of times it passes an interface between structure and empty space. The directional MIL is calculated as the average of all lines for each angle. The MIL ellipsoid is then calculated by a least square fit of the directional MIL to a directed ellipsoid [156].
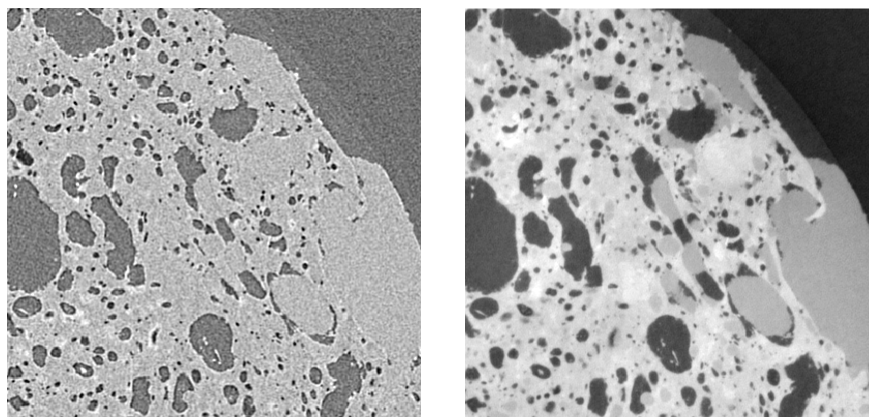
(a) Absorption modality.   (b) Phase-contrast modality.

Figure 5.2: Partial slices of the cooked lard emulsion sample.

5.3   Quantitative analysis of meat emulsions

Due to health aspects, substitution of animal fat with vegetable oil has generated interest in the meat processing industry [157]. However, the higher mobility of the oil compared to the solid animal fat provides a challenge. The coalescence of oil droplets may lead to channel formation in the protein network, facilitating moisture transportation during heat treatment which can be observed as increased cooking losses [154]. Paper A, titled *'Analysis of microstructure in raw and heat treated meat emulsions from mulitmodal X-ray tomography'*, investigates the heat-induced structural changes for meat emulsions, consisting of different fat types. Fat globules act as fillers, reducing the porosity and increasing the stability of the emulsion structure when cooked. Animal fat and vegetable oil have different properties, which will affect the final quality of the emulsion. To evaluate these effects, one sample was prepared with animal lard while the other was prepared with sunflower oil. When the emulsions are cooked, fat and moisture will be separated from the emulsion [148]. The aim is to minimize the cooking loss (i.e. amount of water, protein and fat expelled from the emulsion), and obtain a stable protein structure [158]. The phase-contrast μCT data obtained allowed for visualization of the microstructure of the emulsions to estimate the cooking loss. Figure 5.2 shows a partial slice from the absorption and phase-contrast modalities for the cooked lard sample. The medium gray intensity pockets seen in the phase-contrast modality are the expelled fluid from the emulsion structure, i.e. the cooking loss. This phase is not seen in the absorption modality. Figure 5.3 shows partial 3D visualization of the raw
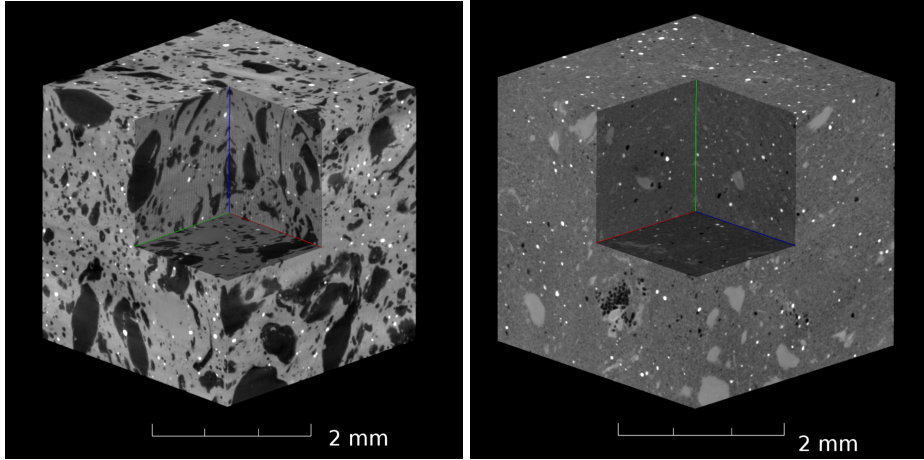
Figure 5.3: Partial visulization of the phase-contrast modality for both lard (left) and sunflower oil (right) emulsion samples prior to cooking.

samples from the phase-contrast modality. It is apparent that the structure is quite different in the two samples. In the lard sample the light gray area is the protein structure, the dark gray blobs are pork fat globules and the white dots are undissolved salt grains. In the sunflower sample the light gray blobs are pure protein which has not been mixed with the rest of the emulsion. The sunflower oil is not visible in the data, as the oil droplets are inseparable from the emulsion mixture due to resolution limits, making the combined voxel intensity appear darker.

Main results

The label maps obtained from segmentation are illustrated in Figure 5.4. From the label maps, parameters such as cooking loss and stability of the protein structure were determined. Additionally, a label map of the fat globules was extracted, and a custom labeling method applied to identify each individual fat globule. Parameters such as fat globule surface area, volume and sphericity were calculated along with meat structure parameters including structure thickness and degree of anisotropy. Additionally, the cooking loss was estimated in three separate phases; i) the segregated fluid within the emulsion, ii) the expelled fluid outside the emulsion and iii) the segregated fat located at the inner rim of the container. These parameters gave insight to how cooking alters the emulsion stability when using either animal or vegetable fat in the emulsion mixture. The results obtained agreed with previous findings [159, 160, 161], which estab-

(a) Raw sample.   (b) Cooked sample.
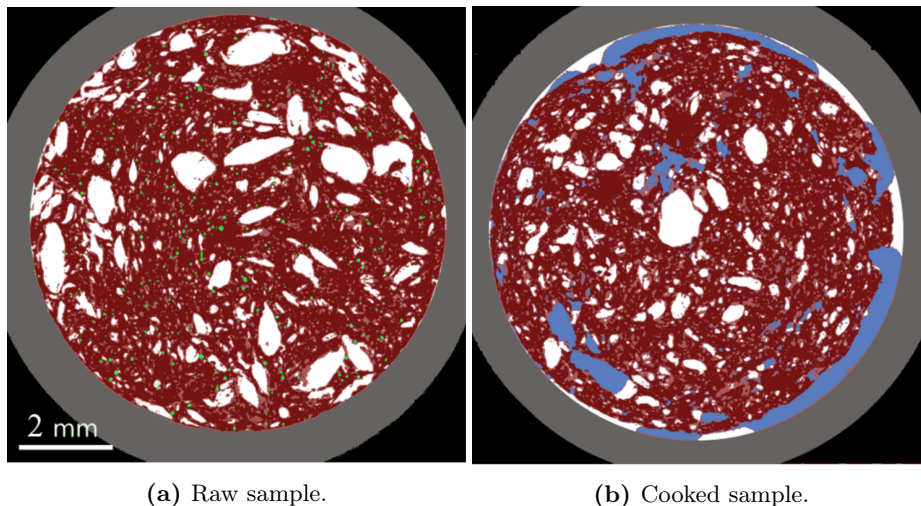
Figure 5.4: A single slice from the lard sample label map volumes prior to and after cooking.

lishes both the grating-based imaging technique and segmentation method as a viable option for imaging the inner structure of meat emulsions. The technological demonstration opens opportunities of utilizing GBI together with advanced analysis tools to investigate a range of characteristics of emulsions such as lipid type, salt content and protein substitutes. The 3D data analysis obtained can replace 2D electron microscopy methods to provide a deeper understanding of emulsion properties.

Main contributions

To summarize, the main contributions of the work include:

- Perform a quantitative analysis of the microstructure of meat emulsions using GBI μCT and advanced data analysis.

- Development of a labeling scheme to identify individual fat globules.

- Relate quantitative geometrical properties to the heat-induced effects on the microstructure of meat emulsions.

- Technological and practical demonstrator of the results achievable when combining GBI with the proposed algorithms.

5.4   Quantitative analysis of whole meat

In paper B, titled *'Novel X-ray phase-contrast tomography method for quanti-
tative studies of heat-induced structural changes in meat'*, a piece of beef was
imaged by GBI µCT, both prior to and after cooking preparation. Figure 5.5
shows a partial slice from the absorption and phase-contrast modalities, where
the phase-contrast modality shows superior contrasts of the meat structure. The
muscle fibers are seen in light gray, the darker gray area is the connective tis-
sue and the black spots are intramuscular fat. The heat-induced difference in
microstructure of the sample was explored by first segmenting the data. As pre-
viously mentioned, the contrast in the phase-contrast image sufficed to segment
the different elements of the muscle, namely the muscle fibers, connective tissue,
intramuscular fat and surrounding water. By applying an anisotropic smoothing
constraint, the thin structures of the connective tissue were preserved, as seen
in Figure 5.6. The muscle fibers were segmented into two populations based on
the differences in electron densities. The outer part of the muscle fibers had a
lower electron density than the inner parts, and this difference was explained
by an increase in the water binding capacity of the muscle fibers exposed to the
surrounding buffer in the sample container. The percent object volumes for the
different structural components were determined from the label maps obtained.
Additionally, a histogram analysis gave insight to the density changes in the
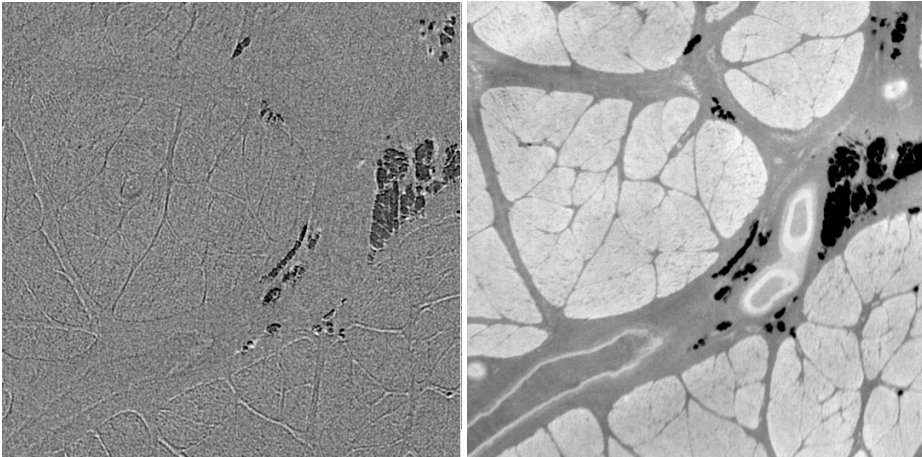different components.

Figure 5.5: Partial visulization of the absorption modality (left) and phase-
contrast modality (right) for a piece of beef after cooking.

Main results

The main findings of the paper showed the increase in water content (i.e. cooking loss) due to cooking. As illustrated in Figure 5.7, shrinkage of the muscle fibers resulted in an increase in the electron density compared to the raw sample. In the cooked sample, the shrinkage has forced the water to be expelled as cooking loss. The increase in the area of the connective tissue in the cooked sample compared to the raw sample indicated partly solubilization, which was further supported by the decrease in electron density of this component. This demonstrates that the meat had undergone a relatively severe heat treatment and reached a temperature above 80°C, and started to gelatinize. The cooking loss was determined to consist of two phases, where the phase closer to the meat had higher protein content and most likely consisted of a gel formed by expelled proteins. The results of the quantitative analysis agreed with previous findings obtained by other imaging methods such as microscopy [162, 148] and MRI [163]. The paper concluded that as the GBI technique transitions to industrial use, the method will be applicable to monitoring the processing steps of meat production. The method may also be suitable for on-line selection of raw materials, which is of great concern for manufacturers as consumers have difficulty in evaluating meat quality [164]. Thus, any type of quality labeling could help increase consumer satisfaction. For off-line use, the results of the paper have proven the GBI technique to be well-suited for characterizing the effect of different processing steps such as salting, drying, freezing and marinating.
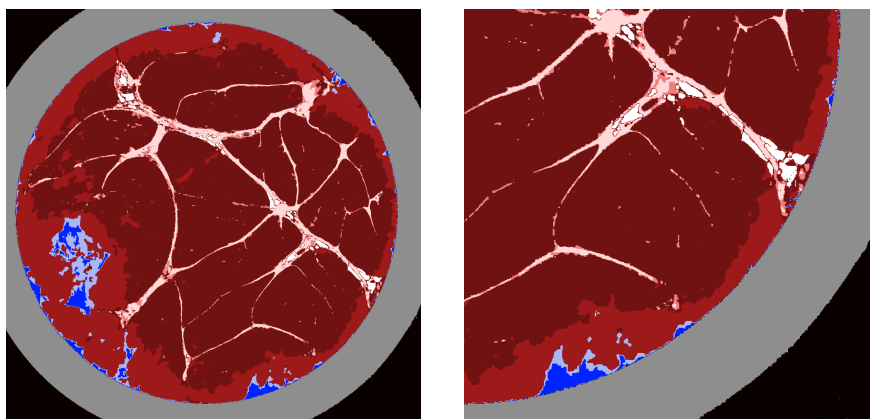
(a) Raw sample.   (b) Selected region of raw sample.

Figure 5.6: Label maps of beef prior to cooking.
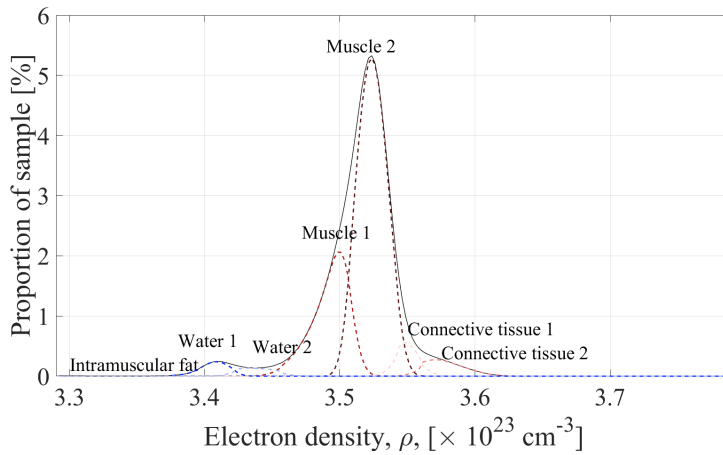
(a) Raw sample.
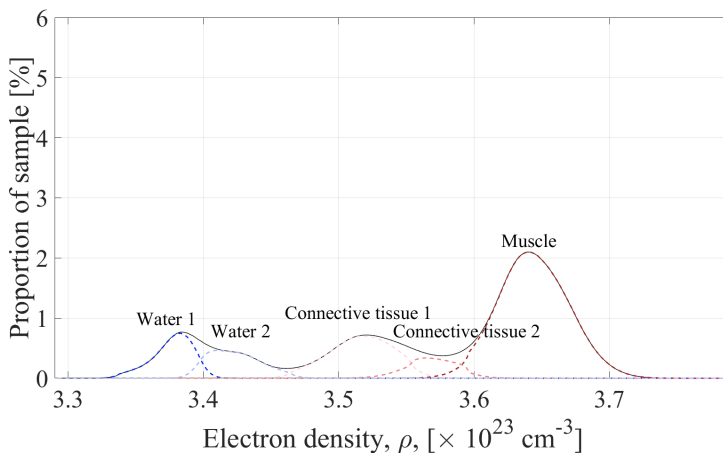
(b) Cooked sample.

Figure 5.7: Histogram analysis for the whole beef sample prior to and after heat treatment.

Main contributions

To summarize, the main contributions of the work include:

- Determining quantitative parameters describing cooking loss from the microstructure of meat using GBI µCT and advanced data analysis.

- Relate quantitative properties to the heat-induced effects on the microstructure of meat, and exploration of the underlying causes of cooking loss.

- Technological and practical demonstrator of the results achievable when combining GBI with the proposed algorithms for characterizing the effect of processing meat.

CHAPTER 6

Novelty and defect detection

This chapter presents how the methodology discussed in Chapter 3 is combined for novelty and defect detection applications. The methods presented here were applied in the data analysis in Papers C and D.

In food manufacturing both the aspects of foreign object and defect detection are immensely important, and development of new analysis techniques is in high demand. As the GBI technique is still primarily seen in synchrotron and laboratory-based settings, a gap between research and industrial use is evident. In order to minimize this gap, Papers C and D focus on demonstrating how GBI can be utilized for novelty and defect detection in food products. Paper C presents image analysis and data analysis techniques to quantitatively assess the gain of using multimodal X-ray imaging for foreign object detection in food. In Paper D a similar approach is taken to assess abnormalities (i.e. defects) in mouse lungs in-vivo. In both papers a model of normality is constructed and new data evaluated based on a statistical approach.

6.1   Novelty detection

Paper C, titled *'Novelty detection of foreign objects in food using multi-modal X-ray imaging'*, demonstrates a method for novelty detection of foreign objects using grating-based X-ray imaging. The study is motivated by the fact that conventional absorption X-ray systems are not sensitive to all foreign objects such as paper, wood chips, light plastics and insects [6]. Experiments were conducted where a selection of common foreign objects (ranging from insects to metals) are placed in seven different food products. The food products were chosen to represent a range of homogeneity in texture, with cheese being the most homogeneous and minced meat being the least. Figure 6.1 shows the dark-field image and absorption image of minced meat with foreign objects present. All foreign objects are distinguishable in the dark-field modality, whilst only some of them can be seen in the absorption modality. Figure 6.2 shows a scatter plot of absorption intensity values versus dark-field intensity values for all food products and foreign objects (the phase-contrast modality is not illustrated in the plot). The distributions of the food products follow a multivariate Gaussian distribution.

For the novelty detection task, the classification problem models 'normal' data and then assigns either a 'normal' or 'abnormal' label to new data based on a given criterion. By manual segmentation of the training data, the 'normal' models of food products were trained using a portion of these pixels. The model was based on a mixture of Gaussians, and the parameters were fitted using the EM algorithm (see Section 3.1.4). For the more homogeneous food products, a single Gaussian was fitted, while two or more were fitted for the more complex food structures. In addition, texture features based on basic image features [165] were calculated and five different food models then created; i) absorption model, ii) phase-contrast model, iii) dark-field model, iv) multivariate intensity model and v) multivariate intensity model including texture features. Given the food models (or 'normal' models) a threshold criterion θ of the Mahalanobis distance measure was determined such that unseen pixel values x were assigned a normal label ($l = 1$) or abnormal label ($l = -1$) according to
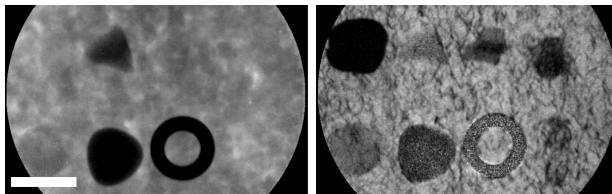
$$l = \begin{cases} 1 & \text{if } x \geq \theta \\ -1 & \text{otherwise.} \end{cases} \tag{6.1}$$

Main results

Examining the ROC curves in Figure 6.3, for varying threshold values of the Mahalanobis distance, reveals that the dark-field model has the minimum dis-

(a) Color image of foreign objects in minced meat.

(b) Absorption modality.   **(c)** Dark-field modality.

Figure 6.1: In a) foreign objects placed in minced meat imaged by GBI. The dark-field image in c) shows higher contrast of foreign objects compared to the absorption modality in b). The white bar represents 1 cm.

tance to perfect classification amongst the three GBI modalities. Further, the model combining all three modalities and the texture features outperforms the other four models. These ROC curves illustrate the results for sliced cheese only. For five out of seven food products, the combined intensity and texture model resulted in the minimum distance to perfect classification. The remaining two models were minced meat and rye bread. Here, the multivariate intensity model outperforms the model containing texture features. As minced meat and rye bread both contain complex textures, it was concluded that a further analysis of the texture features would be required before including them in the model. The object based error rates were evaluated, where the ratio of detected objects versus true number of objects was determined. This was done for several size thresholds when eliminating small objects. By removing small objects, likely to be caused by image noise and artifacts, the number of false positives rapidly decreased. The true positive rate for several of the food products also dropped as the filtering size was increased. A tradeoff is therefore needed, and the balance between detecting true positives and eliminating false positives should be considered. The paper concluded that the pixel-wise and the object based results clearly illustrate the advantage of GBI for foreign object detection in food. The
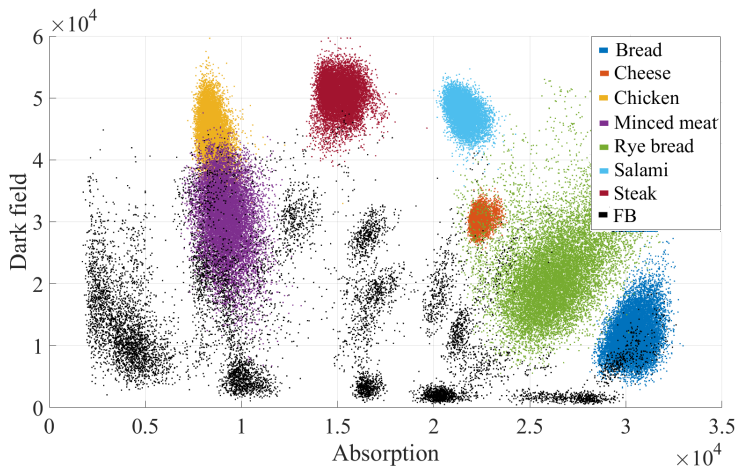
Figure 6.2: Scatterplot of pixel values from each of the food products along with foreign bodies (FB).

most gain was obtained when detecting organic matter and plastics, as was previously shown by Nielsen et al. [49]. This is a significant improvement compared to conventional X-ray systems, since the detection of paper, wood, hair, plastic and insects still remains a challenge with currently available systems [6]. The results demonstrated indicate the strong potential for dark-field X-ray imaging as an alternative to currently available systems.

Main contributions

To summarize, the main contributions of the work include:

- Design of study to determine the feasibility of GBI for foreign object detection in food.

- Evaluation of novelty detection methods to detect foreign objects from GBI images.

- Comparison of univariate and multivariate models.

- Evaluation of the extent to which texture features can be used to obtain higher model accuracy.
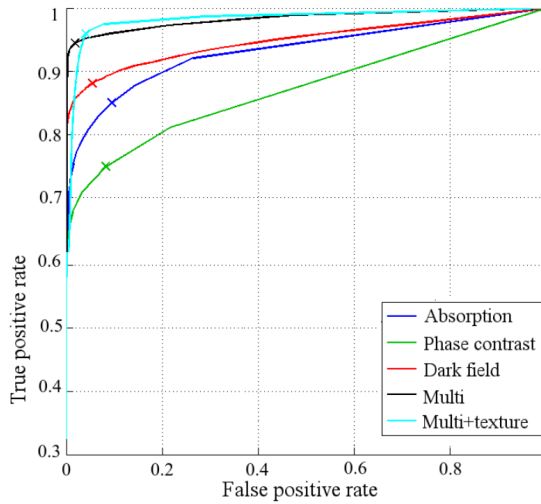
Figure 6.3: Comparison of the receiver operating characteristic curves for different models constructed for sliced cheese.

6.2   Defect detection

Novelty detection in food products is not only concerned with finding foreign objects, but also in detecting defects of the products themselves. These defects include damaged tissue of meat and fish, textural defects in cheese and cellular damage in fruits. Another aspect to defect detection in food products can be disease related. Until now, the contributions presented have described applications for food quality and safety during and after processing. Food quality inspection for meat, poultry and fish starts much earlier in the production chain, even before slaughtering. Phenotyping for animal breeding is a well established trade [29, 166], where various techniques are used to estimate quality traits of animals such as body composition. Animal welfare is also an important topic, where animal breeders and slaughterhouses are under strict guidelines to secure animal well-being [167, 168]. Paper D, titled '*Computer-aided diagnosis of pulmonary diseases using x-ray darkfield radiography*', demonstrates a method for in-vivo defect analysis of animals. A custom preclinical small-animal X-ray dark-field scanner was used to obtain images of mouse lungs [54]. The purpose was to evaluate the systems ability to detect the presences of pulmonary diseases, and to determine to what extent they affect the lung tissue. The outcome of this study is expected to influence future applications for monitoring defects during processing, as well as animal well-being. Furthermore, monitoring temporal changes during food processing could also benefit from the methods demonstrated in pa-

Figure 6.4: Deviation maps for a control-, emphysema- and fibrosis lung. The emphysema maps show the same lung at different stages of emphysema. The color scale illustrates the magnitude of deviation.

per D.

Computer aided-diagnosis of lung diseases is a very active research field [169, 170, 171], where both radiography and tomography X-ray images of lungs are analyzed. Radiography offers limited sensitivity, and typically low contrast of lung tissue. Other drawbacks of lung radiography include difficulties of analysis presented by overlapping structures in the chest such as the heart and clavicles. These problems can be overcome by high-resolution CT [172, 173], providing higher sensitivity at the cost of higher radiation exposure. The advances in GBI have provided the means of measuring lungs by radiography with superior contrast of the lung regions [174, 54]. However, quantitative analysis has been performed by manual selection of regions of interest. Paper D demonstrates a computer-aided diagnosis (CAD) scheme for the automatic segmentation of the lung region from GBI. Additionally, quantitative analysis methods for detecting pulmonary diseases from the lung regions are demonstrated.

The segmentation method used in the developed CAD scheme is based on AAM (see Section 3.2.3), where the shape and texture of the lungs are combined in a single statistical model. The model was trained on the dark-field images due to superior contrast of the lungs in this modality. The lung segmentation obtained from the AAM model was evaluated by determining the similarity coefficients compared to ground truth annotations. Due to severe destruction of some of the lungs, the dark-field images occasionally lacked data support to obtain an
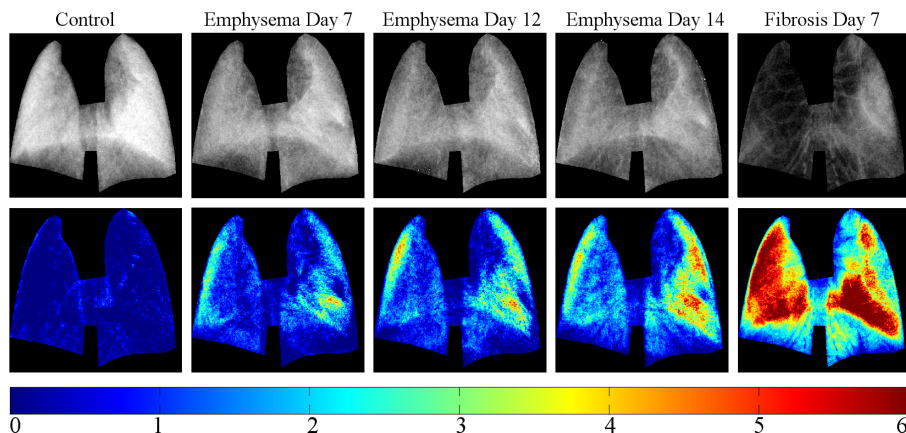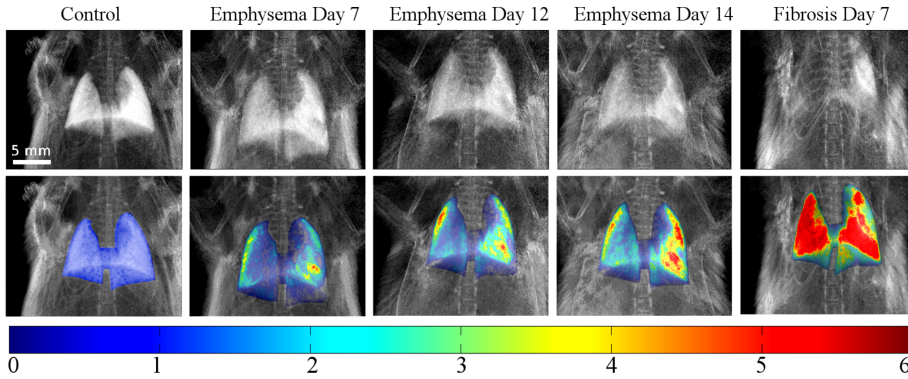
Figure 6.5: Deviation maps for a control-, emphysema- and fibrosis lung. The emphysema maps show the same lung at different stages of emphysema. The color scale illustrates the magnitude of deviation.

acceptable segmentation. Thus, another AAM was trained on the absorption modality, and used for segmentation in these rare cases. From the AAM model, a model of normality for healthy lungs was created by calculating the pixel-wise mean and standard deviation for 15 healthy lungs warped into the mean shape. Unseen lung images were then compared to determine the presence of pulmonary disease, and to what extent they affected the lung tissue. This was done by calculating the T-test statistic for each pixel, i.e. for each pixel the magnitude of standard deviation from the healthy model was determined. Intensity and shape features were then extracted, and a classification determined whether the lung was healthy, emphysematous or fibrosis.

Main results

The CAD scheme provides i) a quantitative analysis on a pixelwise-basis to determine regions affected by pulmonary disease and ii) a lung-based classification of healthy, emphysema diseased and fibrosis diseased lungs. System performance was assessed by i) determining the quality of the segmentations and ii) validating emphysema and fibrosis recognition by a linear support vector machine using leave-one-out cross-validation. A SVM was chosen, due to the limited amount of observations and ease of training, and the linear kernel was chosen to avoid over-fitting and limiting the effort of parameter tuning. Based on the combined intensity and shape features the linear SVM classified all healthy lungs versus diseased correctly, and obtained a 92.65% accuracy when classifying between emphysema lungs and fibrosis. The data included in this study consisted of
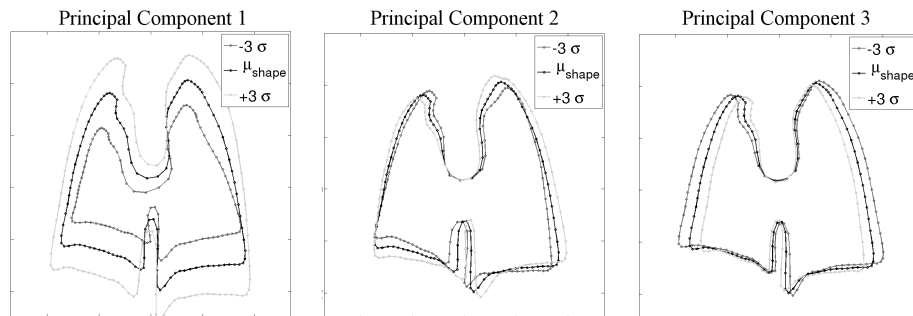
Figure 6.6: First three principal components of the shape parameters after Procrustes alignment (excluding scaling).

cases of pulmonary diseases ranging from mild, moderate and severe. In cases of mild and moderate fibrosis, conventional X-ray transmission images do not provide a clear signal difference between healthy and fibrotic lung tissue [54], and therefore the result of the CAD classification is of great significance. Figure 6.4 shows segmented lung regions and the corresponding deviation maps while Figure 6.5 shows the deviation maps overlayed on the original dark-field images. These deviation maps are considered as a visual aid for radiologists to assess the severity of a pulmonary disease and to determine the regions in the lung that are affected. The main findings of the paper show how progression in emphysema is detected by the CAD scheme for a lung imaged at three separate occasions. This is valuable information in a diagnostic setting, where the success of a treatment could be directly assessed. Another important finding is that by applying PCA to the shape of the lungs, the first PC reveals how the size of the lung is the main contributor to the variation of the shape, see Figure 6.6. The expansion of the emphysema lungs is quite apparent as is illustrated in Figure 6.7. Given a larger data set, future implementations will focus on replacing the handcrafted features and classification steps with deep learning techniques such as deep convolutional neural networks [175, 176].

The pixel-wise deviation maps illustrated here relate to the normal food models proposed for foreign object detection. Thus, a threshold of the T-test statistic can be determined to evaluate regions deviating severely from what is expected. In this setting the scheme could be adjusted for on-line detection of defects in food products.
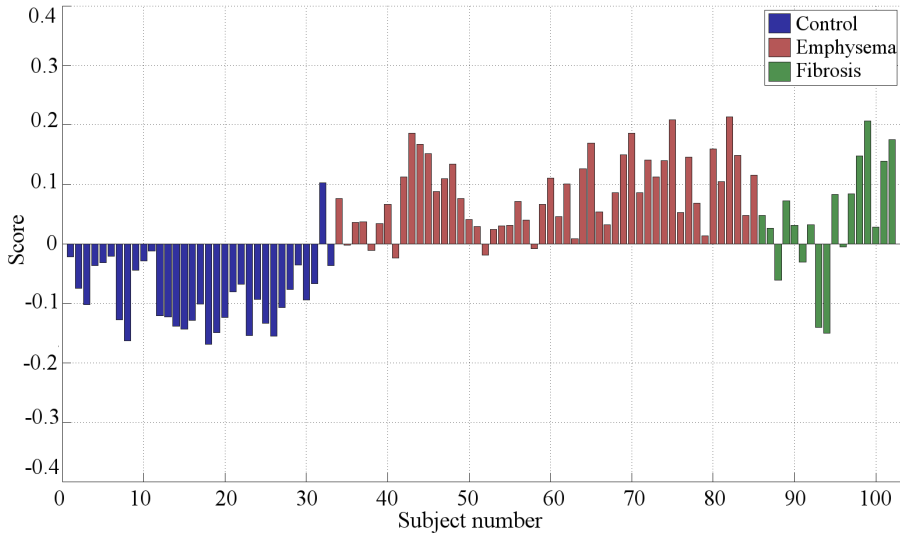
Figure 6.7: Bar plot illustrating the normalized first shape principal component score for all lungs.

Main contributions

To summarize, the main contributions of the work include:

- Development of a computer-aided diagnosis scheme for dark-field images of lungs to identify and assess pulmonary diseases.

- Demonstration of the complementary capabilities of GBI for segmentation of lungs.

- Construction of a model of normality for healthy lungs, to which other lungs are compared to determine both presence and severity of pulmonary disease.

- Interpretation of disease progression for longitudinal studies.

- Analysis of variation in lung shape caused by emphysema.

- Extraction of relevant shape and intensity features for classification between healthy and diseased, and emphysema and fibrosis lungs.

Conclusions

This thesis has presented the application of grating-based X-ray imaging for determining food quality and food safety. For this purpose, relevant methodology from image analysis, statistics and statistical learning has been described and applied to specific problems relevant for food production and food science. Given the multimodal nature of GBI, the data analysis in this thesis has investigated methods accordingly. The problems addressed have been; i) the segmentation of complex µCT data from synchrotron sources, ii) the quantitative analysis of microstructure from synchrotron GBI µCT, iii) novelty detection of foreign objects in food, and finally iv) a defect detection scheme for detection of pulmonary diseases in lungs.

For the purpose of quantitatively analyzing the microstructure of GBI µCT, an extensive segmentation framework was developed. The framework combines Bayesian labeling, where parameters are estimated by EM, and a flexible MRF segmentation method. The segmentation framework can handle both univariate and multivariate data, either 2D or 3D, and energy minimization is approximated via graph cuts. The smoothing constraint can be chosen as isotropic or anisotropic, depending on the structures present in the image. In addition to segmented label maps for visualization and quantification, the segmentation framework provides a histogram analysis for further evaluation and interpretation of the data.

The segmentation framework was applied to GBI µCT images of meat products. The purpose was to evaluate the stability and cooking-loss due to heat treatment. The non-destructive and non-invasive nature of the GBI technique, allowed for imaging of the same sample prior to and after cooking. The results obtained from the quantitative analysis were comparable to existing analysis

techniques, establishing the methods applicability for studies of 3D microstructure of meat products. This serves as a technological demonstrator of the feasibility of the technique to monitor processing steps such as freezing, drying, salting and marinating.

The applicability of the GBI technique for monitoring food products was further evaluated by imaging common foreign objects typically found in food products. A novelty detection scheme was developed, and a comparison of univariate versus multivariate models was made. In addition, the gain of adding texture features to the detection scheme was evaluated. Texture features proved beneficial when imaging food products of homogeneous texture, while more complex food products require extensive tuning of the texture features. The main findings showed significant increase in the detection accuracy of organic- and light foreign objects such as insects and light plastics using dark-field imaging. This is of great relevance and importance for the food industry, as these objects still remain challenging to detect with currently available techniques.

Finally, a scheme for defect detection was demonstrated. This was done by the development of a CAD scheme to detect pulmonary diseases in lungs from dark-field images. The scheme automatically segments lungs based on AAM, which are then compared to a model of normality. The deviation maps created, highlight regions affected by emphysema or fibrosis, and provide a valuable diagnostics tool to assist radiologists. This is specifically important since radiologists are not trained to interpret dark-field images. Additionally, it was shown how the development of emphysema is captured by the scheme. Finally, a concrete classification of lungs as either healthy, emphysematous or fibrosis was demonstrated. A combined model of intensity and texture features obtains a perfect classification of healthy versus diseased lungs, even when the disease is present in mild form. The scheme can easily be adjusted to detect defects on-line in food products. This can be achieved by adding a classification step based on a simple threshold of the pixel-wise deviation maps.

The objectives of this thesis have been met by combining topics within the fields of image analysis, statistics and statistical learning. Its contribution has been to evaluate and demonstrate the applicability of GBI imaging combined with advanced analysis techniques for applications towards food. Four original papers have been introduced and presented. The results highlight the feasibility of GBI for determining food quality and food safety. The results presented in this thesis will play an important role as the GBI technique matures towards industrial applications. The technique is expected to have widespread impact within the fields of food science and food production.

Future outlook

The grating-based X-ray technique has emerged from synchrotron sources, and been further developed as a suitable method for laboratory-setups. Efforts in developing commercial GBI scanners have been made [177, 178, 54], and the first commercially available phase-contrast µCT has been developed (SkyScan-1294, Bruker 2016). Such systems will become valuable for the off-line study of food products from a food science and food engineering perspective. The results presented in this thesis already provide a valuable proof-of-principal of using GBI for such applications.

For the GBI technique to become a feasible option for on-line inspection during food manufacturing, the high through-put required needs to be considered. The physical stepping of the gratings in GBI sets a restriction to the speed of the data acquisition. This limits the technique in terms of feasibility towards food manufacturing. However, recent efforts have proposed scanning methods [179, 180], where the implementation would result in scanning times equivalent to conventional X-ray systems. These results indicate that a conveyor belt solution can be practically implemented within the coming years. As GBI will evolve towards an industrial solution, the work presented in this thesis will serve as an important technological demonstrator for food manufacturing applications.

Bibliography

[1] J. A. Caswell, *Economics of food safety*. Springer Science & Business Media, 2012.

[2] K. G. Grunert, "Food quality and safety: consumer perception and demand," *European Review of Agricultural Economics*, vol. 32, no. 3, pp. 369–391, 2005.

[3] A. Wilcock, M. Pun, J. Khanona, and M. Aung, "Consumer attitudes, knowledge and behaviour: a review of food safety issues," *Trends in Food Science & Technology*, vol. 15, no. 2, pp. 56–66, 2004.

[4] J. Trienekens and P. Zuurbier, "Quality and safety standards in the food industry, developments and challenges," *International Journal of Production Economics*, vol. 113, no. 1, pp. 107 – 122, 2008.

[5] A. P. Craig, A. S. Franca, and J. Irudayaraj, "Surface-enhanced raman spectroscopy applied to food safety," *Annual review of food science and technology*, vol. 4, pp. 369–380, 2013.

[6] Q. Chen, C. Zhang, J. Zhao, and Q. Ouyang, "Recent advances in emerging imaging techniques for non-destructive detection of food quality and safety," *TrAC Trends in Analytical Chemistry*, vol. 52, pp. 261 – 274, 2013.

[7] Z. Xiong, D.-W. Sun, H. Pu, W. Gao, and Q. Dai, "Applications of emerging imaging techniques for meat quality and safety detection and evaluation: A review," *Critical reviews in food science and nutrition*, no. just-accepted, pp. 00–00, 2015.

[8] Y.-Z. Feng and D.-W. Sun, "Application of hyperspectral imaging in food safety inspection and control: a review," *Critical reviews in food science and nutrition*, vol. 52, no. 11, pp. 1039–1058, 2012.

[9] J. Qin, K. Chao, M. S. Kim, R. Lu, and T. F. Burks, "Hyperspectral and multispectral imaging for evaluating food safety and quality," *Journal of Food Engineering*, vol. 118, no. 2, pp. 157–171, 2013.

[10] D. Wu and D.-W. Sun, "Advanced applications of hyperspectral imaging technology for food quality and safety analysis and assessment: A review — part ii: Applications," *Innovative Food Science & Emerging Technologies*, vol. 19, pp. 15 – 28, 2013.

[11] M. F. Marcone, S. Wang, W. Albabish, S. Nie, D. Somnarain, and A. Hill, "Diverse food-based applications of nuclear magnetic resonance (nmr) technology," *Food Research International*, vol. 51, no. 2, pp. 729–747, 2013.

[12] F. Mariette, "Investigations of food colloids by nmr and mri," *Current Opinion in Colloid & Interface Science*, vol. 14, no. 3, pp. 203–211, 2009.

[13] A. Spyros, P. Dais, and P. Belton, *NMR spectroscopy in food analysis.* Royal Society of Chemistry Cambridge, UK, 2013.

[14] A. Gowen, B. Tiwari, P. Cullen, K. McDonnell, and C. O'Donnell, "Applications of thermal imaging in food quality and safety assessment," *Trends in food science & technology*, vol. 21, no. 4, pp. 190–200, 2010.

[15] R. Vadivambal and D. S. Jayas, "Applications of thermal imaging in agriculture and food industry—a review," *Food and Bioprocess Technology*, vol. 4, no. 2, pp. 186–199, 2011.

[16] T. Awad, H. Moharram, O. Shaltout, D. Asker, and M. Youssef, "Applications of ultrasound in analysis, processing and quality control of food: A review," *Food Research International*, vol. 48, no. 2, pp. 410–427, 2012.

[17] B.-K. Cho and J. Irudayaraj, "Foreign object and internal disorder detection in food materials using noncontact ultrasound imaging," *Journal of Food Science*, vol. 68, no. 3, pp. 967–974, 2003.

[18] W. Jun, M. S. Kim, B.-K. Cho, P. D. Millner, K. Chao, and D. E. Chan, "Microbial biofilm detection on food contact surfaces by macro-scale fluorescence imaging," *Journal of Food Engineering*, vol. 99, no. 3, pp. 314–322, 2010.

[19] M. Kim, Y. Chen, and P. Mehl, "Hyperspectral reflectance and fluorescence imaging system for food quality and safety," *Transactions of the ASAE*, vol. 44, no. 3, p. 721, 2001.

[20] R. Zhang, Y. Ying, X. Rao, and J. Li, "Quality and safety assessment of food and agricultural products by hyperspectral fluorescence imaging," *Journal of the Science of Food and Agriculture*, vol. 92, no. 12, pp. 2397–2408, 2012.

[21] T. Brosnan and D.-W. Sun, "Improving quality inspection of food products by computer vision—-a review," *Journal of Food Engineering*, vol. 61, no. 1, pp. 3–16, 2004.

[22] C.-J. Du and D.-W. Sun, "Learning techniques used in computer vision for food quality evaluation: a review," *Journal of food engineering*, vol. 72, no. 1, pp. 39–55, 2006.

[23] R. P. Haff and N. Toyofuku, "X-ray detection of defects and contaminants in the food industry," *Sensing and Instrumentation for Food Quality and Safety*, vol. 2, no. 4, pp. 262–273, 2008.

[24] N. Kotwaliwale, K. Singh, A. Kalne, S. N. Jha, N. Seth, and A. Kar, "X-ray imaging methods for internal quality evaluation of agricultural produce," *Journal of food science and technology*, vol. 51, no. 1, pp. 1–15, 2014.

[25] K. Lim and M. Barigou, "X-ray micro-computed tomography of cellular food products," *Food research international*, vol. 37, no. 10, pp. 1001–1012, 2004.

[26] L. Schoeman, P. Williams, A. du Plessis, and M. Manley, "X-ray micro-computed tomography (μct) for non-destructive characterisation of food microstructure," *Trends in Food Science & Technology*, vol. 47, pp. 10–24, 2016.

[27] W. C. Röntgen, "Über eine neue art von strahlen," *Annalen der Physik*, vol. 300, no. 1, pp. 1–11, 1898.

[28] M. F. i Furnols, M. F. Teran, and M. Gispert, "Estimation of lean meat content in pig carcasses using x-ray computed tomography and pls regression," *Chemometrics and intelligent laboratory systems*, vol. 98, no. 1, pp. 31–37, 2009.

[29] M. Font-i Furnols, A. Carabús, C. Pomar, and M. Gispert, "Estimation of carcass composition and cut composition from computed tomography images of live growing pigs of different genotypes," *animal*, vol. 9, no. 01, pp. 166–178, 2015.

[30] P. A. Picouet, F. Teran, M. Gispert, and M. F. i Furnols, "Lean content prediction in pig carcasses, loin and ham by computed tomography (ct) using a density model," *Meat science*, vol. 86, no. 3, pp. 616–622, 2010.

[31] M. Vester-Christensen, S. G. Erbou, M. F. Hansen, E. V. Olsen, L. B. Christensen, M. Hviid, B. K. Ersbøll, and R. Larsen, "Virtual dissection of pig carcasses," *Meat science*, vol. 81, no. 4, pp. 699–704, 2009.

[32] J.-S. Kwon, J.-M. Lee, and W.-Y. Kim, "Real-time detection of foreign objects using x-ray imaging for dry food manufacturing line," in *Consumer Electronics, 2008. ISCE 2008. IEEE International Symposium on*, pp. 1–4, IEEE, 2008.

[33] D. Mery, I. Lillo, H. Loebel, V. Riffo, A. Soto, A. Cipriano, and J. M. Aguilera, "Automated fish bone detection using x-ray imaging," *Journal of Food Engineering*, vol. 105, no. 3, pp. 485–492, 2011.

[34] Y. Tao, Z. Chen, H. Jing, and J. Walker, "Internal inspection of deboned poultry using x–ray imaging and adaptive thresholding," *Transactions of the ASAE*, vol. 44, no. 4, p. 1005, 2001.

[35] J. Arnau, E. Fulladosa, N. Garcia-Gil, X. Serra, M. Gùrdia, P. Gou, J. Comaposada, P. Picouet, I. Muñoz, *et al.*, "Processing and control technologies to reduce salt content in dry-cured ham and dry-fermented sausages.," *Journées de la Recherche Porcine en France*, vol. 45, pp. 89–95, 2013.

[36] M. De Prados, E. Fulladosa, P. Gou, I. Muñoz, J. Garcia-Perez, and J. Benedito, "Non-destructive determination of fat content in green hams using ultrasound and x-rays," *Meat science*, vol. 104, pp. 37–43, 2015.

[37] E. Fulladosa, I. Muñoz, X. Serra, J. Arnau, and P. Gou, "X-ray absorptiometry for non-destructive monitoring of the salt uptake in bone-in raw hams during salting," *Food Control*, vol. 47, pp. 37–42, 2015.

[38] R. Haff and D. Slaughter, "Real-time x-ray inspection of wheat for infestation by the granary weevil, sitophilus granarius (l.)," *Transactions of the ASAE*, vol. 47, no. 2, p. 531, 2004.

[39] D. Narvankar, C. Singh, D. Jayas, and N. White, "Assessment of soft x-ray imaging for detection of fungal infection in wheat," *Biosystems Engineering*, vol. 103, no. 1, pp. 49–56, 2009.

[40] S. Neethirajan, D. Jayas, and N. White, "Detection of sprouted wheat kernels using soft x-ray image analysis," *Journal of Food Engineering*, vol. 81, no. 3, pp. 509–513, 2007.

[41] S. Neethirajan, C. Karunakaran, D. Jayas, and N. White, "Detection techniques for stored-product insects in grain," *Food Control*, vol. 18, no. 2, pp. 157–162, 2007.

[42] M. Bernau, P. Kremer, E. Lauterbach, E. Tholen, B. Petersen, E. Pappenberger, and A. Scholz, "Evaluation of carcass composition of intact boars using linear measurements from performance testing, dissection, dual energy x-ray absorptiometry (dxa) and magnetic resonance imaging (mri)," *Meat Science*, vol. 104, pp. 58 – 66, 2015.

[43] S. Kelkar, C. J. Boushey, and M. Okos, "A method to determine the density of foods using x-ray imaging," *Journal of food engineering*, vol. 159, pp. 36–41, 2015.

[44] M. Bech, O. Bunk, T. Donath, R. Feidenhans, C. David, and F. Pfeiffer, "Quantitative x-ray dark-field computed tomography," *Physics in medicine and biology*, vol. 55, no. 18, p. 5529, 2010.

[45] F. Pfeiffer, T. Weitkamp, O. Bunk, and C. David, "Phase retrieval and differential phase-contrast imaging with low-brilliance x-ray sources," *Nature physics*, vol. 2, no. 4, pp. 258–261, 2006.

[46] F. Pfeiffer, M. Bech, O. Bunk, P. Kraft, E. F. Eikenberry, C. Brönnimann, C. Grünzweig, and C. David, "Hard-x-ray dark-field imaging using a grating interferometer," *Nature materials*, vol. 7, no. 2, pp. 134–137, 2008.

[47] M. Bech, T. H. Jensen, O. Bunk, T. Donath, C. David, T. Weitkamp, G. Le Duc, A. Bravin, P. Cloetens, and F. Pfeiffer, "Advanced contrast modalities for x-ray radiology: Phase-contrast and dark-field imaging using a grating interferometer," *Zeitschrift fuer medizinische Physik*, vol. 20, no. 1, pp. 7–16, 2010.

[48] T. H. Jensen, A. Böttiger, M. Bech, I. Zanette, T. Weitkamp, S. Rutishauser, C. David, E. Reznikova, J. Mohr, L. B. Christensen, *et al.*, "X-ray phase-contrast tomography of porcine fat and rind," *Meat science*, vol. 88, no. 3, pp. 379–383, 2011.

[49] M. S. Nielsen, T. Lauridsen, L. B. Christensen, and R. Feidenhans, "X-ray dark-field imaging for detection of foreign bodies in food," *Food control*, vol. 30, no. 2, pp. 531–535, 2013.

[50] F. Pfeiffer, O. Bunk, C. David, M. Bech, G. Le Duc, A. Bravin, and P. Cloetens, "High-resolution brain tumor visualization using three-dimensional x-ray phase contrast tomography," *Physics in medicine and biology*, vol. 52, no. 23, p. 6923, 2007.

[51] K. Scherer, L. Birnbacher, M. Chabior, J. Herzen, D. Mayr, S. Grandl, A. Sztrókay-Gaul, K. Hellerhoff, F. Bamberg, and F. Pfeiffer, "Bidirectional x-ray phase-contrast mammography," *PloS one*, vol. 9, no. 5, p. e93502, 2014.

[52] S. Grandl, K. Scherer, A. Sztrókay-Gaul, L. Birnbacher, K. Willer, M. Chabior, J. Herzen, D. Mayr, S. D. Auweter, F. Pfeiffer, *et al.*, "Improved visualization of breast cancer features in multifocal carcinoma using phase-contrast and dark-field mammography: an ex vivo study," *European radiology*, vol. 25, no. 12, pp. 3659–3668, 2015.

[53] K. Scherer, E. Braig, K. Willer, M. Willner, A. A. Fingerle, M. Chabior, J. Herzen, M. Eiber, B. Haller, M. Straub, *et al.*, "Non-invasive differentiation of kidney stone types using x-ray dark-field radiography," *Scientific reports*, vol. 5, 2015.

[54] A. Yaroshenko, F. G. Meinel, M. Bech, A. Tapfer, A. Velroyen, S. Schleede, S. Auweter, A. Bohla, A. Ö. Yildirim, K. Nikolaou, *et al.*, "Pulmonary emphysema diagnosis with a preclinical small-animal x-ray dark-field scatter-contrast scanner," *Radiology*, vol. 269, no. 2, pp. 427–433, 2013.

[55] M. S. Nielsen, T. Lauridsen, M. Thomsen, T. H. Jensen, M. Bech, L. B. Christensen, E. V. Olsen, M. Hviid, R. Feidenhans'l, and F. Pfeiffer, "X-ray tomography using the full complex index of refraction," *Physics in Medicine and Biology*, vol. 57, no. 19, p. 5971, 2012.

[56] C. Kottler, V. Revol, R. Kaufmann, C. Urban, K. Knop, U. Sennhauser, I. Jerjen, T. Lü¨thi, F. Cardot, P. Niedermann, *et al.*, "Phase sensitive x-ray imaging: towards its interdisciplinary applications," in *AIP Conference Proceedings*, vol. 1236, p. 213, 2010.

[57] J. M. Aguilera and D. W. Stanley, *Microstructural principles of food processing and engineering*. Springer Science & Business Media, 1999.

[58] J. M. Aguilera, "Why food microstructure?," *Journal of Food Engineering*, vol. 67, no. 1–2, pp. 3 – 11, 2005.

[59] N. Müller-Fischer and E. J. Windhab, "Influence of process parameters on microstructure of food foam whipped in a rotor–stator device within a wide static pressure range," *Colloids and Surfaces A: Physicochemical and Engineering Aspects*, vol. 263, no. 1–3, pp. 353 – 362, 2005. A collection of papers presented at the 5th European Conference on Foams, Emulsions, and Applications, {EUFOAM} 2004, University of Marne-la-Vallee, Champs sur Marne (France), 5-8 July, 2004.

[60] F. Vergeldt, G. van Dalen, A. Duijster, A. Voda, S. Khalloufi, L. van Vliet, H. V. As, J. van Duynhoven, and R. van der Sman, "Rehydration kinetics of freeze-dried carrots," *Innovative Food Science & Emerging Technologies*, vol. 24, pp. 40 – 47, 2014.

[61] D. Álvarez and S. Barbut, "Effect of inulin, β-glucan and their mixtures on emulsion stability, color and textural parameters of cooked meat batters," *Meat Science*, vol. 94, no. 3, pp. 320 – 327, 2013.

[62] E. E. Kheadr, J. Vachon, P. Paquin, and I. Fliss, "Effect of dynamic high pressure on microbiological, rheological and microstructural quality of cheddar cheese," *International Dairy Journal*, vol. 12, no. 5, pp. 435–446, 2002.

[63] I. D. Mert, G. Sumnu, and S. Sahin, "Microstructure of gluten-free baked products," in *Imaging Technologies and Data Processing for Food Engineers*, pp. 197–242, Springer, 2016.

[64] J. L. Skytte, O. Ghita, P. F. Whelan, U. Andersen, F. Møller, A. B. Dahl, and R. Larsen, "Evaluation of yogurt microstructure using confocal laser scanning microscopy and image analysis," *Journal of food science*, vol. 80, no. 6, pp. E1218–E1228, 2015.

[65] T. Defraeye, V. Lehmann, D. Gross, C. Holat, E. Herremans, P. Verboven, B. E. Verlinden, and B. M. Nicolai, "Application of mri for tissue characterisation of 'braeburn'apple," *Postharvest biology and technology*, vol. 75, pp. 96–105, 2013.

[66] H. Van As and J. van Duynhoven, "Mri of plants and foods," *Journal of Magnetic Resonance*, vol. 229, pp. 25–34, 2013.

[67] E. N. Landis and D. T. Keane, "X-ray microtomography," *Materials characterization*, vol. 61, no. 12, pp. 1305–1316, 2010.

[68] M. A. Rao, S. S. Rizvi, A. K. Datta, and J. Ahmed, *Engineering properties of foods*. CRC Press, 2014.

[69] R. Diener, J. Mitchell, *et al.*, "Using an x-ray image scan to sort bruised apples.," *Agric. Engng.*, vol. 51, pp. 356–7, 1970.

[70] M. Graves, "X-ray bone detection in further processed poultry production," in *Machine vision for the inspection of natural products*, pp. 421–449, Springer, 2003.

[71] J.-A. Jiang, H.-Y. Chang, K.-H. Wu, C.-S. Ouyang, M.-M. Yang, E.-C. Yang, T.-W. Chen, and T.-T. Lin, "An adaptive image segmentation algorithm for x-ray quarantine inspection of selected fruits," *Computers and electronics in agriculture*, vol. 60, no. 2, pp. 190–200, 2008.

[72] M. van Dael, S. Lebotsa, E. Herremans, P. Verboven, J. Sijbers, U. Opara, P. Cronje, and B. Nicolaï, "A segmentation and classification algorithm for online detection of internal disorders in citrus using x-ray radiographs," *Postharvest Biology and Technology*, vol. 112, pp. 205 – 214, 2016.

[73] R. J. Kopanic, B. W. Sheldon, C. Wright, *et al.*, "Cockroaches as vectors of salmonella: laboratory and field trials," *Journal of Food Protection*, vol. 57, no. 2, pp. 125–131, 1994.

[74] M. Iwasa, S.-I. Makino, H. Asakura, H. Kobori, and Y. Morimoto, "Detection of escherichia coli o157: H7 from musca domestica (diptera: Muscidae) at a cattle farm in japan," *Journal of Medical Entomology*, vol. 36, no. 1, pp. 108–112, 1999.

[75] C. Karunakaran and D. Jayas, "X-ray imaging," in *Imaging with Electromagnetic Spectrum*, pp. 33–55, Springer, 2014.

[76] D. Attwood, *Soft x-rays and extreme ultraviolet radiation: principles and applications.* Cambridge university press, 2007.

[77] M. Bech, *X-ray imaging with a grating interferometer.* PhD thesis, Graduate School of Science, University of Copenhagen, 2009.

[78] T. H. Jensen, *Refraction and scattering based x-ray imaging.* PhD thesis, Graduate School of Science, University of Copenhagen, 2010.

[79] A. W. Chao, K. H. Mess, M. Tigner, and F. Zimmermann, *Handbook of accelerator physics and engineering.* World scientific, 2013.

[80] A. A. de Moura Meneses, A. Giusti, A. P. De Almeida, L. P. Nogueira, D. Braz, R. C. Barroso, and C. Eduardo deAlmeida, "Automated segmentation of synchrotron radiation micro-computed tomography biomedical images using graph cuts and neural networks," *Nuclear Instruments and Methods in Physics Research Section A: Accelerators, Spectrometers, Detectors and Associated Equipment*, vol. 660, no. 1, pp. 121–129, 2011.

[81] J. Als-Nielsen and D. McMorrow, *Elements of modern X-ray physics.* John Wiley & Sons, 2011.

[82] G. Michael, "X-ray computed tomography," *Physics Education*, vol. 36, no. 6, p. 442, 2001.

[83] J. Hsieh, R. C. Molthen, C. A. Dawson, and R. H. Johnson, "An iterative approach to the beam hardening correction in cone beam ct," *Medical physics*, vol. 27, no. 1, pp. 23–29, 2000.

[84] G. Van Gompel, K. Van Slambrouck, M. Defrise, K. J. Batenburg, J. de Mey, J. Sijbers, and J. Nuyts, "Iterative correction of beam hardening artifacts in ct," *Medical physics*, vol. 38, no. S1, pp. S36–S49, 2011.

[85] C. H. Yan, R. T. Whalen, G. S. Beaupre, S. Y. Yen, and S. Napel, "Reconstruction algorithm for polychromatic ct imaging: application to beam hardening correction," *Medical Imaging, IEEE Transactions on*, vol. 19, no. 1, pp. 1–11, 2000.

[86] M. J. Willemink, P. A. de Jong, T. Leiner, L. M. de Heer, R. A. Nievelstein, R. P. Budde, and A. M. Schilham, "Iterative reconstruction techniques for computed tomography part 1: technical principles," *European radiology*, vol. 23, no. 6, pp. 1623–1631, 2013.

[87] M. S. Nielsen, "Novel x-ray imaging modalities - seeing through food," Master's thesis, Niels Bohr Institute, University of Copenhagen, Copenhagen, 2012.

[88] F. Pfeiffer, M. Bech, O. Bunk, T. Donath, B. Henrich, P. Kraft, and C. David, "X-ray dark-field and phase-contrast imaging using a grating interferometer," *Journal of Applied Physics*, vol. 105, no. 10, p. 102006, 2009.

[89] J.-P. Guigay, S. Zabler, P. Cloetens, C. David, R. Mokso, and M. Schlenker, "The partial talbot effect and its use in measuring the coherence of synchrotron x-rays," *Journal of synchrotron radiation*, vol. 11, no. 6, pp. 476–482, 2004.

[90] C. David, B. Nöhammer, H. Solak, and E. Ziegler, "Differential x-ray phase contrast imaging using a shearing interferometer," *Applied physics letters*, vol. 81, no. 17, pp. 3287–3289, 2002.

[91] A. Momose, "Phase-sensitive imaging and phase tomography using x-ray interferometers," *Optics Express*, vol. 11, no. 19, pp. 2303–2314, 2003.

[92] T. Weitkamp, A. Diaz, C. David, F. Pfeiffer, M. Stampanoni, P. Cloetens, and E. Ziegler, "X-ray phase imaging with a grating interferometer," *Optics express*, vol. 13, no. 16, pp. 6296–6304, 2005.

[93] F. Pfeiffer, C. Kottler, O. Bunk, and C. David, "Hard x-ray phase tomography with low-brilliance sources," *Physical review letters*, vol. 98, no. 10, p. 108105, 2007.

[94] T. Weitkamp, C. David, C. Kottler, O. Bunk, and F. Pfeiffer, "Tomography with grating interferometers at low-brilliance sources," in *SPIE Optics+ Photonics*, pp. 63180S–63180S, International Society for Optics and Photonics, 2006.

[95] T. Hastie, R. Tibshirani, J. Friedman, and J. Franklin, "The elements of statistical learning: data mining, inference and prediction," *The Mathematical Intelligencer*, vol. 27, no. 2, pp. 83–85, 2005.

[96] A. P. Dempster, N. M. Laird, and D. B. Rubin, "Maximum likelihood from incomplete data via the em algorithm," *Journal of the royal statistical society. Series B (methodological)*, pp. 1–38, 1977.

[97] C. J. Wu, "On the convergence properties of the em algorithm," *The Annals of statistics*, pp. 95–103, 1983.

[98] T. Hastie, R. Tibshirani, and G. Walther, "Estimating the number of data clusters via the gap statistic," *J Roy Stat Soc B*, vol. 63, pp. 411–423, 2001.

[99] R. De Maesschalck, D. Jouan-Rimbaud, and D. L. Massart, "The mahalanobis distance," *Chemometrics and intelligent laboratory systems*, vol. 50, no. 1, pp. 1–18, 2000.

[100] S. Z. Li, *Markov random field modeling in image analysis*. Springer Science & Business Media, 2009.

[101] T. F. Cootes, G. J. Edwards, and C. J. Taylor, "Active appearance models," *IEEE Transactions on Pattern Analysis & Machine Intelligence*, no. 6, pp. 681–685, 2001.

[102] M. N. Murty and V. S. Devi, *Pattern recognition: An algorithmic approach*. Springer Science & Business Media, 2011.

[103] G. F. Newell and E. W. Montroll, "On the theory of the ising model of ferromagnetism," *Reviews of Modern Physics*, vol. 25, no. 2, p. 353, 1953.

[104] P. Clifford, "Markov random fields in statistics," *Disorder in physical systems: A volume in honour of John M. Hammersley*, pp. 19–32, 1990.

[105] R. B. Potts, "Some generalized order-disorder transformations," in *Mathematical proceedings of the cambridge philosophical society*, vol. 48, pp. 106–109, Cambridge Univ Press, 1952.

[106] F.-Y. Wu, "The potts model," *Reviews of modern physics*, vol. 54, no. 1, p. 235, 1982.

[107] V. Kolmogorov and R. Zabin, "What energy functions can be minimized via graph cuts?," *Pattern Analysis and Machine Intelligence, IEEE Transactions on*, vol. 26, no. 2, pp. 147–159, 2004.

[108] L. R. Ford Jr and D. R. Fulkerson, *Flows in networks*. Princeton university press, 2015.

[109] Y. Boykov, O. Veksler, and R. Zabih, "Fast approximate energy minimization via graph cuts," *Pattern Analysis and Machine Intelligence, IEEE Transactions on*, vol. 23, no. 11, pp. 1222–1239, 2001.

[110] V. Grau, J. C. Downs, and C. F. Burgoyne, "Segmentation of trabeculated structures using an anisotropic markov random field: application to the study of the optic nerve head in glaucoma," *Medical Imaging, IEEE Transactions on*, vol. 25, no. 3, pp. 245–255, 2006.

[111] J. Weickert, "Coherence-enhancing diffusion filtering," *International Journal of Computer Vision*, vol. 31, no. 2-3, pp. 111–127, 1999.

[112] P. Perona and J. Malik, "Scale-space and edge detection using anisotropic diffusion," *Pattern Analysis and Machine Intelligence, IEEE Transactions on*, vol. 12, no. 7, pp. 629–639, 1990.

[113] M. J. Black, G. Sapiro, D. H. Marimont, and D. Heeger, "Robust anisotropic diffusion," *Image Processing, IEEE Transactions on*, vol. 7, no. 3, pp. 421–432, 1998.

[114] M. B. Stegmann, B. K. Ersbøll, and R. Larsen, "Fame-a flexible appearance modeling environment," *Medical Imaging, IEEE Transactions on*, vol. 22, no. 10, pp. 1319–1331, 2003.

[115] T. F. Cootes, G. J. Edwards, and C. J. Taylor, "Active appearance models," in *Computer Vision—ECCV'98*, pp. 484–498, Springer, 1998.

[116] C. Goodall, "Procrustes methods in the statistical analysis of shape," *Journal of the Royal Statistical Society. Series B (Methodological)*, pp. 285–339, 1991.

[117] F. J. Rohlf and D. Slice, "Extensions of the procrustes method for the optimal superimposition of landmarks," *Systematic Biology*, vol. 39, no. 1, pp. 40–59, 1990.

[118] T. F. Cootes, C. J. Taylor, D. H. Cooper, and J. Graham, "Active shape models-their training and application," *Computer vision and image understanding*, vol. 61, no. 1, pp. 38–59, 1995.

[119] T. F. Cootes and C. J. Taylor, "Statistical models of appearance for medical image analysis and computer vision," in *Medical Imaging 2001*, pp. 236–248, International Society for Optics and Photonics, 2001.

[120] D. Cristinacce and T. Cootes, "Automatic feature localisation with constrained local models," *Pattern Recognition*, vol. 41, no. 10, pp. 3054–3067, 2008.

[121] T. F. Cootes, M. C. Ionita, C. Lindner, and P. Sauer, "Robust and accurate shape model fitting using random forest regression voting," in *Computer Vision–ECCV 2012*, pp. 278–291, Springer, 2012.

[122] C. Lindner, S. Thiagarajah, J. Wilkinson, T. Consortium, G. Wallis, and T. F. Cootes, "Fully automatic segmentation of the proximal femur using random forest regression voting," *Medical Imaging, IEEE Transactions on*, vol. 32, no. 8, pp. 1462–1472, 2013.

[123] L. R. Dice, "Measures of the amount of ecologic association between species," *Ecology*, vol. 26, no. 3, pp. 297–302, 1945.

[124] P. Jaccard, "The distribution of the flora in the alpine zone.," *New phytologist*, vol. 11, no. 2, pp. 37–50, 1912.

[125] H. J. Kuijf, P. Moeskops, B. D. de Vos, W. H. Bouvy, J. de Bresser, G. J. Biessels, M. A. Viergever, and K. L. Vincken, "Supervised novelty detection in brain tissue classification with an application to white matter hyperintensities," in *SPIE Medical Imaging*, pp. 978421–978421, International Society for Optics and Photonics, 2016.

[126] A. S. Minhas and M. R. Reddy, "Neural network based approach for anomaly detection in the lungs region by electrical impedance tomography," *Physiological Measurement*, vol. 26, no. 4, p. 489, 2005.

[127] L. Tarassenko, P. Hayton, N. Cerneaz, and M. Brady, "Novelty detection for the identification of masses in mammograms," in *Artificial Neural Networks, 1995., Fourth International Conference on*, pp. 442–447, IET, 1995.

[128] G. Ginesu, D. D. Giusto, V. Märgner, and P. Meinlschmidt, "Detection of foreign bodies in food by thermal image processing," *Industrial Electronics, IEEE Transactions on*, vol. 51, no. 2, pp. 480–490, 2004.

[129] S. Calderara, U. Heinemann, A. Prati, R. Cucchiara, and N. Tishby, "Detecting anomalies in people's trajectories using spectral graph analysis," *Computer Vision and Image Understanding*, vol. 115, no. 8, pp. 1099–1111, 2011.

[130] D. Ryan, S. Denman, C. Fookes, and S. Sridharan, "Textures of optical flow for real-time anomaly detection in crowds," in *Advanced Video and Signal-Based Surveillance (AVSS), 2011 8th IEEE International Conference on*, pp. 230–235, IEEE, 2011.

[131] S. Wu, B. E. Moore, and M. Shah, "Chaotic invariants of lagrangian particle trajectories for anomaly detection in crowded scenes," in *Computer Vision and Pattern Recognition (CVPR), 2010 IEEE Conference on*, pp. 2054–2060, IEEE, 2010.

[132] M. A. Pimentel, D. A. Clifton, L. Clifton, and L. Tarassenko, "A review of novelty detection," *Signal Processing*, vol. 99, pp. 215–249, 2014.

[133] R. Kohavi *et al.*, "A study of cross-validation and bootstrap for accuracy estimation and model selection," in *Ijcai*, vol. 14, pp. 1137–1145, 1995.

[134] A. Liaw and M. Wiener, "Classification and regression by randomforest," *R news*, vol. 2, no. 3, pp. 18–22, 2002.

[135] J. Schmidhuber, "Deep learning in neural networks: An overview," *Neural Networks*, vol. 61, pp. 85–117, 2015.

[136] K.-B. Duan and S. S. Keerthi, "Which is the best multiclass svm method? an empirical study," in *Multiple classifier systems*, pp. 278–285, Springer, 2005.

[137] G. H. Golub and C. Reinsch, "Singular value decomposition and least squares solutions," *Numerische mathematik*, vol. 14, no. 5, pp. 403–420, 1970.

[138] A. Momose, T. Takeda, Y. Itai, and K. Hirano, "Phase–contrast x–ray computed tomography for observing biological soft tissues," *Nature medicine*, vol. 2, no. 4, pp. 473–475, 1996.

[139] R. Beichel, A. Bornik, C. Bauer, and E. Sorantin, "Liver segmentation in contrast enhanced ct data using graph cuts and interactive 3d segmentation refinement methods," *Medical physics*, vol. 39, no. 3, pp. 1361–1373, 2012.

[140] S. Esneault, C. Lafon, and J.-L. Dillenseger, "Liver vessels segmentation using a hybrid geometrical moments/graph cuts method," *Biomedical Engineering, IEEE Transactions on*, vol. 57, no. 2, pp. 276–283, 2010.

[141] R. J. Schneider, D. P. Perrin, N. V. Vasilyev, G. R. Marx, P. J. del Nido, and R. D. Howe, "Mitral annulus segmentation from 3d ultrasound using graph cuts," *Medical Imaging, IEEE Transactions on*, vol. 29, no. 9, pp. 1676–1687, 2010.

[142] H. Einarsdottir, "Segmentation toolbox for tomographic image data," in *3rd Annual Conference of the COST Action FA1102 (FAIM III)*, 2014.

[143] J. Crouse and M. Koohmaraie, "Effect of freezing of beef on subsequent postmortem aging and shear force," *Journal of Food Science*, vol. 55, no. 2, pp. 573–574, 1990.

[144] C. Leygonie, T. J. Britz, and L. C. Hoffman, "Impact of freezing and thawing on the quality of meat: Review," *Meat science*, vol. 91, no. 2, pp. 93–98, 2012.

[145] A. A. Kader, "Fruit maturity, ripening, and quality relationships," in *International Symposium Effect of Pre-& Postharvest factors in Fruit Storage 485*, pp. 203–208, 1997.

[146] B. Nicolai and L. Piazza, "Food microstructure," *Innovative Food Science & Emerging Technologies*, vol. 24, pp. 1–1, 2014.

[147] R. Miklos, M. S. Nielsen, H. Einarsdóttir, R. Feidenhans'l, and R. Lametsch, "Novel x-ray phase-contrast tomography method for quantitative studies of heat induced structural changes in meat," *Meat Science*, vol. 100, pp. 217 – 221, 2015.

[148] E. Tornberg, "Effects of heat on meat proteins–implications on structure and quality of meat products," *Meat science*, vol. 70, no. 3, pp. 493–508, 2005.

[149] J.-L. Damez and S. Clerjon, "Quantifying and predicting meat and meat products quality attributes using electromagnetic waves: An overview," *Meat science*, vol. 95, no. 4, pp. 879–896, 2013.

[150] J. B. Roerdink and A. Meijster, "The watershed transform: Definitions, algorithms and parallelization strategies," *Fundamenta informaticae*, vol. 41, no. 1, 2, pp. 187–228, 2000.

[151] D. Legland, K. Kiêu, and M.-F. Devaux, "Computation of minkowski measures on 2d and 3d binary images," *Image Analysis and Stereology*, vol. 26, pp. 83–93, 2007.

[152] R. Klette and A. Rosenfeld, *Digital geometry: Geometric methods for digital picture analysis.* Elsevier, 2004.

[153] H. Wadell, "Volume, shape, and roundness of quartz particles," *The Journal of Geology*, pp. 250–280, 1935.

[154] S. Barbut, "Importance of fat emulsification and protein matrix characteristics in meat batter stability," *Journal of Muscle Foods*, vol. 6, no. 2, pp. 161–177, 1995.

[155] T. Harrigan and R. Mann, "Characterization of microstructural anisotropy in orthotropic materials using a second rank tensor," *Journal of Materials Science*, vol. 19, no. 3, pp. 761–767, 1984.

[156] T. Hildebrand, A. Laib, R. Müller, J. Dequeker, and P. Rüegsegger, "Direct three-dimensional morphometric analysis of human cancellous bone: microstructural data from spine, femur, iliac crest, and calcaneus," *Journal of bone and mineral research*, vol. 14, no. 7, pp. 1167–1174, 1999.

[157] J. Wood, R. Richardson, G. Nute, A. Fisher, M. Campo, E. Kasapidou, P. Sheard, and M. Enser, "Effects of fatty acids on meat quality: a review," *Meat science*, vol. 66, no. 1, pp. 21–32, 2004.

[158] M. Wu, Y. L. Xiong, J. Chen, X. Tang, and G. Zhou, "Rheological and microstructural properties of porcine myofibrillar protein–lipid emulsion composite gels," *Journal of food science*, vol. 74, no. 4, pp. E207–E217, 2009.

[159] Y.-S. Choi, J.-H. Choi, D.-J. Han, H.-Y. Kim, M.-A. Lee, H.-W. Kim, J.-Y. Jeong, and C.-J. Kim, "Characteristics of low-fat meat emulsion systems with pork fat replaced by vegetable oils and rice bran fiber," *Meat Science*, vol. 82, no. 2, pp. 266–271, 2009.

[160] R. Miklos, X. Xu, and R. Lametsch, "Application of pork fat diacylglycerols in meat emulsions," *Meat science*, vol. 87, no. 3, pp. 202–205, 2011.

[161] H. Vural, I. Javidipour, and O. O. Ozbas, "Effects of interesterified vegetable oils and sugarbeet fiber on the quality of frankfurters," *Meat Science*, vol. 67, no. 1, pp. 65–72, 2004.

[162] J. Bendall and D. Restall, "The cooking of single myofibres, small myofibre bundles and muscle strips from beef m. psoas and m. sternomandibularis muscles at varying heating rates and temperatures," *Meat Science*, vol. 8, no. 2, pp. 93–117, 1983.

[163] M. Bouhrara, S. Clerjon, J.-L. Damez, C. Chevarin, S. Portanguen, A. Kondjoyan, and J.-M. Bonny, "Dynamic mri and thermal simulation to interpret deformation and water transfer in meat during heating," *Journal of agricultural and food chemistry*, vol. 59, no. 4, pp. 1229–1235, 2011.

[164] K. G. Grunert, L. Bredahl, and K. Brunsø, "Consumer perception of meat quality and implications for product development in the meat sector—a review," *Meat science*, vol. 66, no. 2, pp. 259–272, 2004.

[165] M. Crosier and L. D. Griffin, "Using basic image features for texture classification," *International Journal of Computer Vision*, vol. 88, no. 3, pp. 447–460, 2010.

[166] E. Gjerlaug-Enger, J. Kongsro, J. Ødegård, L. Aass, and O. Vangen, "Genetic parameters between slaughter pig efficiency and growth rate of different body tissues estimated by computed tomography in live boars of landrace and duroc," *animal*, vol. 6, no. 01, pp. 9–18, 2012.

[167] M. Dawkins, *Animal suffering: the science of animal welfare.* Springer Science & Business Media, 2012.

[168] T. Grandin, *Improving animal welfare: a practical approach.* CABI, 2015.

[169] A. El-Baz, G. M. Beache, G. Gimel'farb, K. Suzuki, K. Okada, A. Elnakib, A. Soliman, and B. Abdollahi, "Computer-aided diagnosis systems for lung cancer: challenges and methodologies," *International journal of biomedical imaging*, vol. 2013, 2013.

[170] G. Coppini, M. Miniati, S. Monti, M. Paterni, R. Favilla, and E. M. Ferdeghini, "A computer-aided diagnosis approach for emphysema recognition in chest radiography," *Medical engineering & physics*, vol. 35, no. 1, pp. 63–73, 2013.

[171] P. J. Mazzone, N. Obuchowski, M. Phillips, B. Risius, B. Bazerbashi, and M. Meziane, "Lung cancer screening with computer aided detection chest radiography: design and results of a randomized, controlled trial," *PloS one*, vol. 8, no. 3, p. e59650, 2013.

[172] M. C. Godoy, T. J. Kim, C. S. White, L. Bogoni, P. de Groot, C. Florin, N. Obuchowski, J. S. Babb, M. Salganicoff, D. P. Naidich, *et al.*, "Benefit of computer-aided detection analysis for the detection of subsolid and solid lung nodules on thin-and thick-section ct," *American Journal of Roentgenology*, vol. 200, no. 1, pp. 74–83, 2013.

[173] R. Wiemker, P. Rogalla, T. Blaffert, D. Sifri, O. Hay, E. Shah, R. Truyen, and T. Fleiter, "Aspects of computer-aided detection (cad) and volumetry of pulmonary nodules using multislice ct," *The British journal of radiology*, 2014.

[174] F. G. Meinel, A. Yaroshenko, K. Hellbach, M. Bech, M. Müller, A. Velroyen, F. Bamberg, O. Eickelberg, K. Nikolaou, M. F. Reiser, *et al.*, "Improved diagnosis of pulmonary emphysema using in vivo dark-field radiography," *Investigative radiology*, vol. 49, no. 10, pp. 653–658, 2014.

[175] M. Anthimopoulos, S. Christodoulidis, L. Ebner, A. Christe, and S. Mougiakakou, "Lung pattern classification for interstitial lung diseases using a deep convolutional neural network," *Transactions on Medical Imaging*, 2016.

[176] H.-C. Shin, H. R. Roth, M. Gao, L. Lu, Z. Xu, I. Nogues, J. Yao, D. Mollura, and R. M. Summers, "Deep convolutional neural networks for computer-aided detection: Cnn architectures, dataset characteristics and transfer learning," *Transactions on Medical Imaging*, 2016.

[177] T. Koehler, H. Daerr, G. Martens, N. Kuhn, S. Löscher, U. van Stevendaal, and E. Roessl, "Slit-scanning differential x-ray phase-contrast mammography: Proof-of-concept experimental studies," *Medical physics*, vol. 42, no. 4, pp. 1959–1965, 2015.

[178] A. Tapfer, M. Bech, A. Velroyen, J. Meiser, J. Mohr, M. Walter, J. Schulz, B. Pauwels, P. Bruyndonckx, X. Liu, *et al.*, "Experimental results from a preclinical x-ray phase-contrast ct scanner," *Proceedings of the National Academy of Sciences*, vol. 109, no. 39, pp. 15691–15696, 2012.

[179] C. Kottler, F. Pfeiffer, O. Bunk, C. Grünzweig, and C. David, "Grating interferometer based scanning setup for hard x-ray phase contrast imaging," *Review of scientific instruments*, vol. 78, no. 4, p. 043710, 2007.

[180] A. Momose, W. Yashiro, H. Maikusa, and Y. Takeda, "High-speed x-ray phase imaging and x-ray phase tomography with talbot interferometer and

white synchrotron radiation," *Optics express*, vol. 17, no. 15, pp. 12540–12545, 2009.

Part III

Publications

Analysis of micro-structure in raw and heat treated meat emulsions from multimodal X-ray tomography

CrossMark

Analysis of micro-structure in raw and heat treated meat emulsions from multimodal X-ray microtomography

Hildur Einarsdóttir [a,*], Mikkel Schou Nielsen [b], Rikke Miklos [c], René Lametsch [c], Robert Feidenhans'l [b], Rasmus Larsen [a], Bjarne Kjær Ersbøll [a]

[a] Department of Applied Mathematics and Computer Science, Technical University of Denmark, Matematiktorvet Bldg. 303B, DK-2800 Kgs. Lyngby, Denmark
[b] Niels Bohr Institute, University of Copenhagen, Blegdamsvej 17, DK-2100 Copenhagen, Denmark
[c] Department of Food Science, University of Copenhagen, Rolighedsvej 30, DK-1958 Frederiksberg C, Denmark

ARTICLE INFO

ABSTRACT

This study presents a novel non-destructive X-ray technique for analyzing meat emulsions before and after heat treatment. The method is based on X-ray grating-interferometry where three complementary imaging modalities are obtained simultaneously measuring the absorption, refraction and scattering properties of the sample. Enhanced contrast capabilities of this X-ray technique makes studies on materials with similar attenuation properties possible. The emulsion samples were imaged both in a raw and cooked state. Additionally, different fat types were used in the emulsions in order to compare microstructural differences when either pork fat or sunflower oil was added. From the reconstructed tomograms the different constituents in the emulsions were segmented using a multivariate segmentation method. From this, a quantitative analysis was performed between the different samples, determining properties such as percent object volumes, porosity, average structure thickness and cooking loss. The grating-based X-ray technique and multivariate segmentation made the analysis of the microstructure possible which further gives insight to how both heat treatment, and the use of different lipid types, affect the final protein network quality.

Industrial relevance: Meat emulsions have previously been thoroughly studied, and the use of various fat substitutes and protein stabilizers has been investigated. The grating-based multimodal X-ray tomography method presented here is a feasible method to investigate the microstructural changes induced by heat treatment. It provides high-resolution three dimensional spatial information and in contrast to 2D imaging methods, quantitative parameters can be extracted by image analysis for the entire sample volume. Additionally, the non-destructive method allows for imaging the same sample before and after cooking.

© 2013 Elsevier Ltd. All rights reserved.

1. Introduction

The most important functional characteristics in comminuted meat products are the gel-forming abilities of the myofibrillar proteins. During comminution, salt-soluble myofibrillar proteins are extracted that, when heated, create a dense protein network referred to as gel (Tornberg, 2005). Some of the solubilized proteins will emulsify the added fat by forming an interfacial protein film around the fat globules, which are further stabilized by the protein gel (Barbut, 1995; Wu, Xiong, Chen, Tang, & Zhou, 2009). The fat globules act as fillers, reducing the porosity and increasing the stability of the gel. Differences in the physicochemical properties of saturated and unsaturated lipids, i.e. emulsification properties and physical state, will affect the distribution of fat and the influence on the gel stability and thereby the quality of the final product. Due to health aspects, substitution of animal fat with vegetable oil has generated interest in the meat processing industry

(Wood et al., 2004). The lower melting point of the vegetable oil facilitates an even distribution of small oil droplets in the meat batter leading to formation of a homogeneous gel structure. However, the higher mobility of the oil compared to the solid animal fat is a challenge. The coalescence of oil droplets may lead to channel formation in the protein network facilitating moisture transportation during heat treatment which can be observed as increased cooking losses (Barbut, 1995).

Studies on the quality of meat emulsions rely on a variety of measurements. These include determination of pH values, cooking loss, color composition, texture profiles, apparent viscosity, and emulsion stability (Choi et al., 2009, 2010; Gordon & Barbut, 1991; Shao, Zou, Xu, Wu, & Zhou, 2011). Current imaging techniques used to analyze the quality of meat emulsions have mainly focused on two dimensional measurements from either scanning- and transmission electron microscopy (Álvarez et al., 2012; Totosaus & Pérez-Chabela, 2009), light micrographs (Álvarez & Barbut, 2013; Youssef & Barbut, 2009, 2010), or confocal laser scanning microscopy (Sorapukdee, Kongtasorn, Benjakul, & Visessanguan, 2012). Due to the similar attenuation properties of the soft materials in meat emulsions, the use of X-ray microcomputed

tomography (μCT) has been limited. In Santos-Garcés et al. (2012) a feasibility study of X-ray μCT for microstructure analysis of fermented sausages demonstrated that absorption tomography provided contrast between meat, fat and air holes. Although this μCT analysis identified fat particles and air holes, the technique was not accurate enough to distinguish between pork lean and fat when these constituents were emulsified. Novel X-ray techniques based on grating-interferometry provide new imaging modalities that can be obtained simultaneously with absorption tomography (Bech et al., 2010). These modalities, phase contrast and dark-field imaging, measure the electron density and the diffusion length of the sample. Enhanced contrast capabilities of this X-ray technique makes studies on materials with similar attenuation properties, such as soft tissue, possible. Previous studies have demonstrated superior contrast with X-ray phase-contrast CT compared to conventional CT in a study of pork rind and fat (Jensen et al., 2011), and demonstrated the potential for improved segmentation when using multivariate analysis by combining conventional CT with phase-contrast CT for bivariate segmentation of a piece of pork back fat and a piece of beef muscle tissue (Nielsen et al., 2012).

In this paper, the novel X-ray technique is used to investigate the differences in microstructures of meat emulsions in three dimensions. Such analysis allows for determining structural parameters of the entire sample instead of inferring from partial information obtained by two dimensional imaging techniques. The information obtained from a three dimensional analysis is believed to further increase the understanding of emulsion microstructure. Additionally, the non-destructive technique offers the possibility to study the same sample in both raw and cooked condition. The samples used were raw and heat treated meat emulsions (10% protein, 25% fat, 60% moisture) prepared with either pork fat (lard) or sunflower oil. Absorption, phase contrast and dark-field tomograms were obtained at a synchrotron facility using a grating interferometer. From the reconstructed tomograms the different constituents in the emulsions were segmented using a multivariate segmentation method. A quantitative analysis was performed by measuring geometrical parameters in order to determine the microstructural differences of the emulsions when using lard or sunflower oil and also the effect heat treatment has on the emulsion quality.

2. Materials and methods

2.1. X-ray modalities

In Fig. 1 the three types of physical interactions — absorption, refraction and scattering — obtained from the absorption, phase-contrast and dark-field imaging modalities of grating-based interferometry are illustrated. The effect on an incoming Gaussian shaped beam profile (black) is depicted when elements with different physical properties are measured. The profiles shown in color represent what is recorded when a material is present. In green, the effect from an absorptive material is shown to attenuate the beam, while in blue, the effect of a refractive material is seen to cause a transverse shift in the position of the beam profile. Lastly, the small-angle scattering from a material with ordered micro-structures causes the beam profile, here shown in red, to broaden. By separating the attenuation, transverse shift and broadening of the beam, it is thus possible to measure three complementary imaging modalities. For further details on the X-ray modalities, the reader is referred to Bech, Jensen, et al. (2010) and Pfeiffer (2012).

2.2. Grating-based interferometry

One method to separate the three X-ray interactions is grating-based imaging (GBI), which relies on an X-ray interferometer consisting of periodic gratings for measurements. A schematic of a setup for GBI is shown in Fig. 2. Grating G1 produces a periodic intensity modulation, consisting of periodic fringes, transverse to the beam direction. The change in position, mean value and amplitude of the periodic fringes
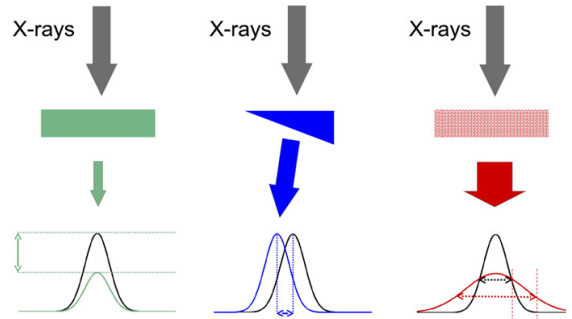

Fig. 1. The incoming X-ray beam changes when a sample is present. The effect on the beam from an absorptive material is shown in green, a refractive material in blue and a material with a homogeneous distribution of micro-structures in red.

can be probed using a second grating, G2, by physically moving one of the gratings in several steps, acquiring a projection image between each movement of the grating. From the same series of scans, both the absorption, refraction and small-angle scattering can be extracted giving an inherent pixel correspondence. Tomograms are then created for each modality using filtered back-projection. This results in absorption, phase-contrast and dark-field image volumes, measuring the attenuation length, electron density and the linear diffusion coefficient of the sample, respectively (Bech et al., 2010; Weitkamp, David, Kottler, Bunk, & Pfeiffer, 2006). GBI using synchrotron sources was first demonstrated in the beginning of the 2000s (David, Nohammer, Solak, & Ziegler, 2002; Momose, 2003; Weitkamp et al., 2005), and later adapted to laboratory-based setups (Pfeiffer, Weitkamp, Bunk, & David, 2006). The method can be applied using polychromatic sources but a certain degree of spatial coherence is needed. In a laboratory setup, spatial coherence can be achieved either by using a microfocus source or by using a third grating G0, which acts as an array of line sources for use with source sizes up to a square millimeter.

2.3. Meat emulsion samples

The meat emulsions used in this study were prepared in batches of 1 kg in a food processor (CombiMax 600, Braun, Germany). Thawed meat (480 g), potato starch (5 g), curing salt (NaCl with 0.6% nitrite) (17 g) and crushed ice (248 g) were comminuted at highest speed for 2 min. The temperature at this point was 1 °C in all batters. After addition of 250 g of either hand chopped cubes of lard or sunflower oil the batter was comminuted for 2 min. The temperature was measured (approx. 12 °C), and comminuting was continued for 1 min. End
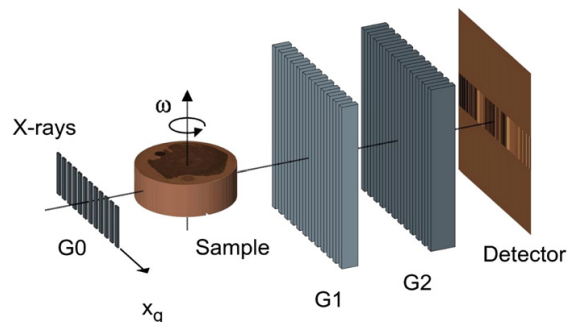

Fig. 2. A schematic of a X-ray tomography setup using a grating interferometer. Reprinted from Nielsen et al., 2012.

temperature was 14 °C. A portion of both the animal fat and sunflower oil batches was placed in sample containers. The samples were then centrifuged at 5000 g for 10 min, and had the lid closed under the surface of degassed PBS. The PBS-buffer was degassed to avoid bubble formation during scanning. The samples were imaged in this raw state prior to cooking. For the heating of the samples, a 200 mL glass of water was heated in a microwave oven up to boiling point. The sample in the container was then immediately placed in the water and left to stand for 10 min for the sunflower oil sample and 15 min for the pork fat sample. Both samples were then placed in a cold-water bath, 10 min for the sunflower oil sample and 15 min for the pork fat sample. The cooked samples were then imaged again. The increased times for the animal fat sample was to ensure that the sample was heated to a homogeneous temperature and likewise cooled to a stable cooling temperature. No difference due to heating and cooling times was observed in the data and therefore the shorter times for the sunflower oil sample are not believed to have affected the final result.

2.4. Tomography measurements

Absorption, phase-contrast and dark-field μCT scans of both the raw and cooked meat emulsions were obtained at the TOMCAT beamline at the Swiss Light Source, Paul Scherrer Institut (PSI), Villigen, Switzerland. The setup is described in detail in McDonald et al. (2009). For this study the energy was set to 25 kV, and the third fractional Talbot distance (Weitkamp et al., 2006) was used. The full volumes obtained were $1720 \times 1720 \times 513$ voxels, with an effective voxel size at sample of $7.4\ \mu m \times 7.4\ \mu m \times 7.4\ \mu m$. The total scan time was between 80 and 90 min per sample. Differences in scan time were due to fluctuations in motor movement times.

2.5. Image segmentation

Before quantitative parameters can be extracted it is necessary to segment the data volumes. This is done by classifying each voxel to a label l representing one of the elements present in the sample. These elements consist of the sample container and constituents including meat, fat, oil and salt. The set of possible labels for the classification task is given as $L = (l_1,...,l_k)$. As the data obtained from GBI is multivariate, each voxel v_i can be represented by a vector of the three intensities $\mathbf{x}_i = (x_{i1}, x_{i2}, x_{i3})$, $i = 1,...,N$ where N is the number of voxels and (x_{i1}, x_{i2}, x_{i3}) represent the absorptive, refractive, and scatter intensities of the i-th voxel, respectively. In order to determine the likelihood of label l_j, $j = 1,...,k$, for voxel v_i and given $\mathbf{x}_i$, the data is modeled as a mixture of multivariate Gaussian distributions using an expectation-maximization (EM) algorithm (Hastie, Tibshirani, & Friedman, 2009). For each volume the number of known constituents is used as the number of Gaussians to fit, and the result obtained from the EM algorithm is multivariate normal distributions describing the constituents. From the distributions, the mean $\boldsymbol{\mu}_j = (\mu_{j1}, \mu_{j2}, \mu_{j3})$ and covariance matrix $\boldsymbol{\Sigma}_j$ for each constituent label l_j is known and the maximum likelihood label estimate for each voxel v_i can then be found for the label distribution that maximizes

$$P(x_i|\boldsymbol{\mu}_j, \boldsymbol{\Sigma}_j) = \frac{1}{(2\pi)^{3/2}\left(|\boldsymbol{\Sigma}_j|\right)^{1/2}} \exp\left(-\frac{1}{2}\left(x_i - \boldsymbol{\mu}_j\right)^{\top} \boldsymbol{\Sigma}_j^{-1}\left(x_i - \boldsymbol{\mu}_j\right)\right) \quad (1)$$

where the exponential term is the Mahalanobis distance providing a relative measure of the voxels distance to a given distribution.

In order to account for image noise and partial volume voxels the spatial context of the data is modeled by a Markov random field (MRF). Here, the data volume is considered as a random field defined on a set of sites, $\mathbf{S}$, where each site represents a voxel v_i. Each site has an associated stochastic variable, f_i, where $I \in \mathbf{S}$. The stochastic variables can take on a value within the set of labels $\mathbf{L}$, i.e. $f_i \in \mathbf{L}$. Subsequently

the neighborhood for each site i is defined as $\mathbf{N}_i$, which consists of six neighboring sites (voxels to the left, right, top, bottom, front and back). The probability of site i having label f_i is then given by

$$P(f_i|f_j, j \in \{S \setminus i\}) = P(f_i|f_{\mathbf{N}_i}) \quad (2)$$

where $\mathbf{S}$ is the set of sites and $f_{\mathbf{N}i} = f_j, j \in \mathbf{N}_i$. Given the possible set of labels $\mathbf{L}$ the smoothed labeling is found by minimizing the energy $E(f)$ of the labeling f

$$\arg \min_f \left(-\sum_{i \in S} D(f_i) + \sum_{i,j \in \mathbf{N}_i} V\left(f_i, f_j\right) \right) \quad (3)$$

where $D(f_i)$ is the probability of label f to voxel site i given by Eq. (1), and $V(f_i, f_j)$ is the separation cost of f on the neighboring pixel sites i and j given by

$$V\left(f_i, f_j\right) = \begin{cases} -\beta_{ij} \text{ for } f_i = f_j \\ \beta_{ij} \text{ otherwise} \end{cases}. \quad (4)$$

Here β is a parameter denoting the amount of desired homogeneity (smoothing). Hence the smoothness of the resulting segmentation can be steered by altering β. Fig. 3 illustrates the neighborhood relation of the MRF. To find the optimal segmentation solution the multi-labeling problem is solved using graph cuts with alpha expansions as described in Boykov, Veksler, and Zabih (2001).

2.6. Object labeling

In order to measure certain parameters for the segmented objects, such as mean volume and mean surface area, a labeling scheme is required. A normal connected components labeling algorithm (Sedgewick, 1998) will label multiple objects as a single object even if only one voxel connects them. Therefore a more sophisticated labeling scheme is required to separate connected objects. A custom region-growing labeling algorithm was developed for this purpose. The region-growing method relies on the distance map of a binary volume of the objects in question. The region is 'eroded' by eliminating all voxels that have a Euclidean distance smaller than a given threshold to the surrounding phase. The new binary volume is then labeled with conventional connected components labeling scheme. These labels are subsequently 'flooded' to previously eroded voxels starting with the largest distance under the threshold and iterating towards the edge between the object and surrounding phase.

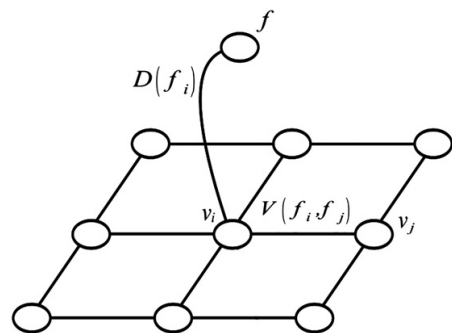**Fig. 3.** The Markov random field illustrated for voxel v_i (only the left, right, top and bottom neighbors are shown). The cost of assigning label f to voxel site i is given by minimizing the energy of all possible labeling configurations.
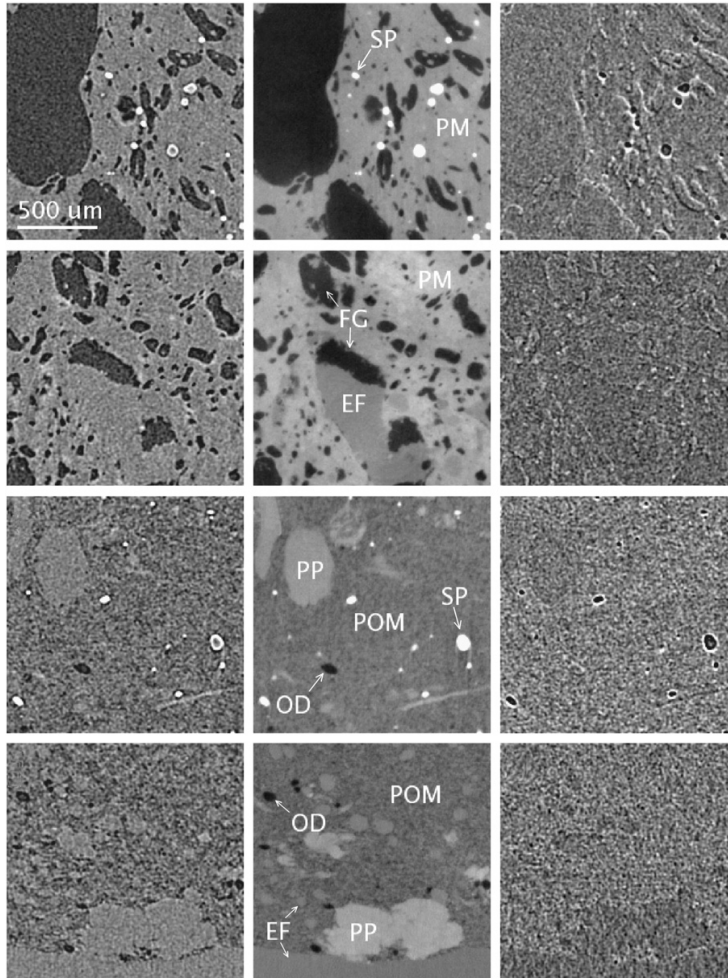
Fig. 4. Partial transverse slices from each modality for the emulsion samples where the top row shows the raw lard sample, row two the cooked lard sample, row three shows the raw sunflower oil sample and the bottom row shows the sunflower oil sample in cooked state. The left column shows the absorption modality, middle column shows the phase contrast modality and the right column shows the dark-field modality. Labels for the constituents are given in the phase contrast images: FG — fat globules; EF — expressible fluid; OD — oil droplet; POM — mixture of protein, oil, starch and moisture; PM — mixture of protein, starch and moisture; SP — salt particle. The images have been contrast enhanced for clarity.

The flooding of voxel labels is done at random to avoid directional artifacts.

2.7. Quantitative parameters

The following 3D geometric parameters for the constituents (fat, protein network, salt, expressible fluid (jelly) and oil droplets) were calculated using custom software written in Matlab: (i) the percent object volume (POV), percentage of volume for each constituent present in the sample volume; (ii) percent loss (PL), the percentage of volume for expressible fluid and fat segregated from the protein network; (iii) porosity (P), the fraction of the volume of pores (fat, salt, expressible fluid and oil droplets) within the protein network; (iv) scaled degree of anisotropy (DA), the degree of 3D asymmetry in the emulsion structure; (v) structure thickness (ST), the average of the local thickness of the protein network; (vi) mean volume (MV), a measure of the average volume of fat and expressible fluid; (vii) mean

sphericity (SP) of the expressible fluid and fat globules, which is found by

$$\psi = \frac{\pi^{\frac{1}{3}}\left(6V_p\right)^{\frac{2}{3}}}{A_p} \tag{5}$$

where V_p is the volume of the particle and A_p is the surface area[1].

3. Results and discussion

3.1. Tomography results

A partial transverse slice from each tomographic reconstruction of the emulsion samples obtained at TOMCAT is shown in Fig. 4. A

---

[1] The sphericity of a sphere is 1 and any particle which is not a sphere will have sphericity of less than 1.
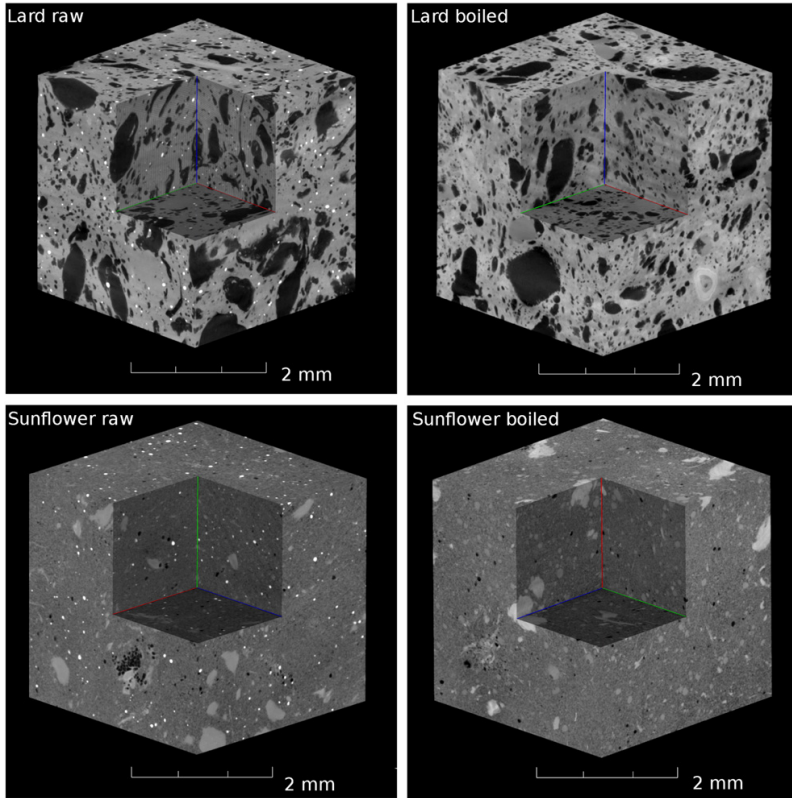
Fig. 5. Partial 3D visualization of the phase contrast sample volumes with VolView.

screenshot from a 3D visualization of the phase contrast modality using VolView can be seen in Fig. 5. Here, the pork fat is seen as darker globules in the lard emulsions and the slightly lighter regions in the emulsions with sunflower oil are pure protein that has not been mixed with the rest of the emulsion. In both the absorption and phase contrast slices the protein network has a darker intensity for the sunflower oil emulsions than the emulsions mixed with pork lard. This is due to the mixture of oil and meat, inseparable due to resolution limitations. It is apparent that the phase contrast modality results in the highest contrast between the different constituents, and the expressible fluid is only distinguishable in the phase contrast modality. Although the dark-field modality seems mainly to consist of noise, further inspection shows that high contrasts can be seen at edges were different constituents meet. This is most notable at the salt–protein interface. The salt particles are completely dissolved after heat treatment. Additionally, expressible fluid has formed in both emulsion samples during cooking and as a result of this the protein mixture has obtained a slightly higher intensity in the phase contrast modality indicating an increased electron density.
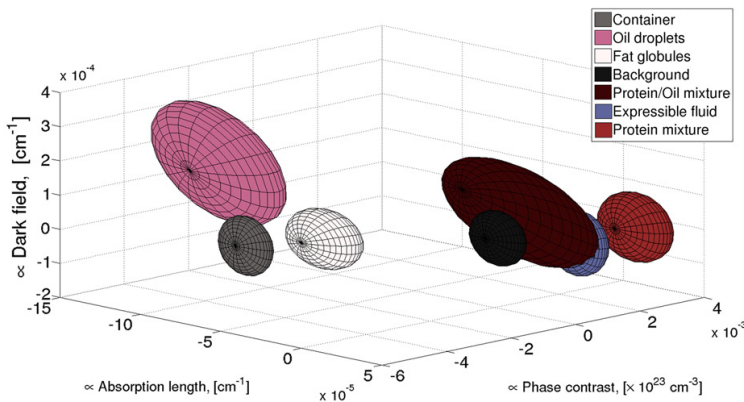

Fig. 6. The result from the EM algorithm represented by the covariance matrices of the distributions.
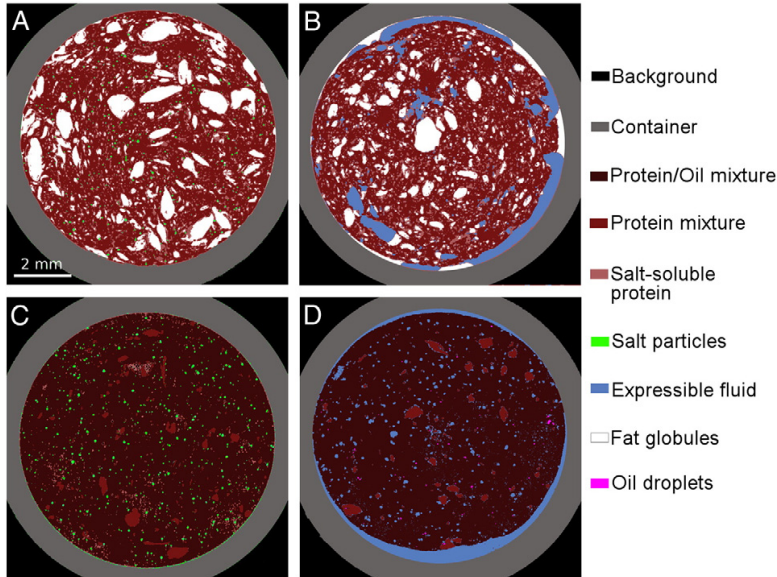
Fig. 7. A slice from each of the segmented volumes. A) Raw lard sample, B) boiled lard sample, C) raw sunflower oil sample and D) boiled sunflower oil sample.

It is apparent that the different modalities obtained provide complementary information, giving more detail of the sample imaged than previously possible with conventional X-ray absorption imaging.

3.2. Segmentation and object labeling

The mixture of Gaussians model obtained with the EM algorithm is illustrated in Fig. 6, where all constituents excluding salt are shown. The protein–oil mixture and oil phase have a higher variance in the dark field modality than the other constituents. This imaging modality can reveal information on features below the detector resolution (Pfeiffer et al., 2008). Thus oil droplets smaller than the resolution of the detector may be the cause for the high scattering in these two phases. The most distinct separation of the constituents is seen in the phase contrast modality. The absorption modality also contributes valuable information for the segmentation step. Thus, by combining the three modalities obtained in the X-ray grating interferometry tomography, additional information is available for the segmentation allowing for a better separation of the phases.

The segmentation results for each data volume can be seen in Fig. 7, where the color labeling scheme is explained to the right. These segmentation results were compared with annotations performed manually by two experts on a single slice from the phase contrast volumes. A confusion matrix is given in Table 1, giving the rate of correctly classified voxels. The main error of the segmentation constitutes of expressible fluid voxels incorrectly labeled as protein. However, the expressible fluid is essentially protein that has solubilized, and therefore it can be difficult to determine precisely which voxels belong to the expressible fluid phase and which belong to protein. The bias of the annotation therefore varies with the user annotating the data. Additionally, most constituents interface with the protein network, and partial volume voxels containing both protein and another constituent are therefore the main cause for misclassification. Overall the segmentation accuracy of the multivariate contextual method is approximately 97%.

To highlight the importance of correct labeling of objects, before performing a further quantitative analysis, the results from the custom region growing method are compared with the standard connected components method in Fig. 8. Here the labeled objects are the fat globules in the raw lard sample. The standard method results in a large portion of the fat globules being labeled as a single object (represented in gray). The region growing method better separates single fat globules, giving a more realistic labeling result, and thereby also a more correct result from the quantitative analysis. The custom algorithm was calibrated to minimize the amount of 'over' segmentation. To validate the performance of the custom labeling algorithm, a ground truth was obtained by randomly selecting 20 objects labeled by the manual method and having two experts determine the number of globules it consisted of using 3D slicer visualization software. The results of the custom labeling method was then compared to this ground truth, resulting in a (94.85 ± 2.96) % labeling accuracy compared to the (8.42 ± 1.36) % of the manual labeling algorithm.

Table 1
Confusion matrix determined by the actual constituent labels and the predicted labels given in percentages (%). The ground truth labels are determined by two manual annotations, and the results are given as the mean $\pm$ the standard deviation from these annotations.

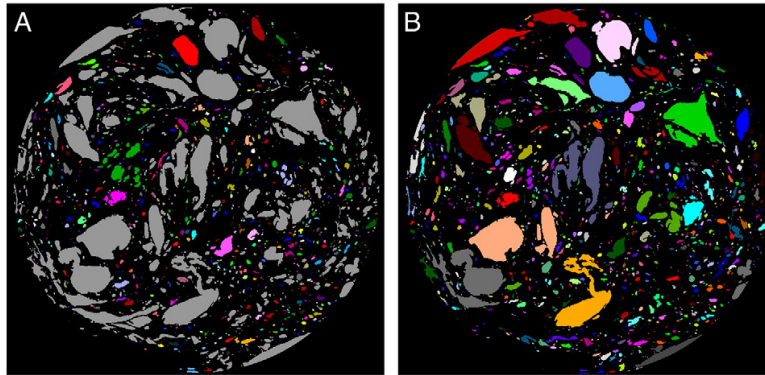|		Predicted class				
		Jelly	Oil	Fat	Salt	Protein
Actual class	Jelly	93.35 ± 3.04	–	0.2 ± 0.14	–	6.40 ± 2.90
	Oil	–	96.4 ± 1.9	–	–	3.6 ± 4.95
	Fat	0.07 ± 0.05	–	98.9 ± 1.13	–	1.05 ± 1.06
	Salt	–	–	–	99.05 ± 0.64	0.95 ± 0.64
	Protein	1.1 ± 0.42	0.2 ± 0.28	0.35 ± 0.50	0.1 ± 0.0	98.25 ± 0.35

Fig. 8. Labeling results of fat globules from A) the normal connected components algorithm and B) the custom region growing algorithm applied to the segmented raw lard volume. Colors represent the separate objects labeled by the algorithms.

3.3. Quantitative analysis

Given the segmentations, a quantitative analysis of the emulsion microstructures was performed. Table 2 gives the percentage object volumes (POVs) for the constituents of the samples. The raw protein phase for the lard sample is found to be 73.9%, salt is 0.8% and fat 25.3%. When comparing the POV to the weighted ingredients (480 g meat, 5 g starch, 1.7 g salt, 248 g ice, 250 g fat) it is noted that the combined weight percentage of the meat, starch and ice amounts to 73.3% of the 1 kg batch. Since these ingredients are all segmented as the single protein mixture phase, the results fit well. The same goes for the sunflower oil sample. Here, the POV for the segmented protein and sunflower oil mixture was found at 98.3% and the POV for salt 1.7%, which is precisely the weighted percentage of these ingredients for the sunflower oil batch. Although weighted percentages and volume percentages are not the same measure, these results are reassuring. For the lard sample, the protein mixture volume decreases by 14.5% due to cooking loss after heat treatment. A smaller shrinkage is observed in the emulsion prepared with sunflower oil, and the protein network volume in this sample decreases by 11%. The cooking percent loss (PL) due to heat treatment is two-fold. First, the loss of expressible fluid is determined as the expressible fluid segregated from the emulsion. Secondly, the segregated fat located at the outer rim of the container is also considered as cooking loss. This combined cooking loss gives some insight into the moisture reserving capability of the emulsion. The expressible fluid cooking loss for the lard sample (7.4%) is slightly lower than for the sunflower oil sample (8.3%), corresponding to the findings of Barbut (1995). However, the POV of the entire expressible fluid (including fluid trapped in the cooked emulsion) for the sunflower oil sample (12.7%) is lower than for the lard sample (15.6%). These results agree with previous findings (Choi et al., 2009; Vural, Javidipour, & Ozbas, 2004). The same results obtained for the lard sample have previously been shown in Miklos, Xu, and Lametsch (2011), where the water separation was found to be 15.2% of the total sample weight when lard was used. Additionally for the lard sample, 2.7% of the fat is segregated from the emulsion, contributing to the overall cooking loss of 10.1%.

Based on the segmented and labeled results, additional quantitative parameters were extracted, given in Table 3. The porosity of the lard sample is greater than for the sunflower oil sample due to the resolution limitations. The large fat globules are detectable, however the oil droplets are too small to be distinguished in the protein mixture. The porosity due to expressible fluid can however be detected and therefore the increase in porosity after heat treatment should preferably be considered. For the lard sample the porosity increases by 9.5% while only a 3.1% increase in porosity is observed for the sunflower oil sample. It is worth noting that the use of sunflower oil resulted in a larger number of expressible fluid populations. The mean volume of these populations is however smaller than for the lard sample. The scaled degree of anisotropy also reflects the homogeneity of the protein structure in the sunflower oil sample which has a greater 3D symmetry implying a more heterogeneous and stable protein network. The relative structure thickness of the protein network for both samples is found to decrease by approximately 21% due to heat treatment. Considering the pore structure of the samples, the expressible fluid populations within the cooked sunflower oil sample have a smaller average volume and higher sphericity, which contributes to the resulting homogeneity of the protein network. An interesting result is that the number of fat globules doubles after heat treatment, resulting in a decreased mean volume and surface area for the globules. During heating, within a temperature range of 43–70 °C, the fat within the protein encapsulated globules is in an expanding liquid form while the thin shell surrounding is in a semi-solid rigid state (Jones & Mandigo, 1982). The internal pressure in the globules can therefore cause ruptures to the shell at weak points, causing fat droplets to escape from the larger globules. These quantitative parameters illustrate how the use of sunflower oil results in a more stable and homogeneous protein network.

4. Conclusions

This paper has presented the use of a novel non-destructive X-ray technique to measure the microstructure of meat emulsions and the effect heat treatment and different lipid types have on the protein network. By utilizing the modalities obtained from the grating interferometer,

Table 2
Percent object volumes (POVs) for the constituents in the raw and cooked samples of meat emulsions containing either lard fat or sunflower oil. Cooking percent loss (PL) is given for the expressible fluid and fat segregated from the cooked emulsion.

Parameter[a]	Lard raw	Lard cooked	Sunflower oil raw	Sunflower oil cooked
POVs				
POV-meat matrix	73.9	59.4	98.1	87.1
POV-jelly	–	15.6	–	12.7
POV-fat	25.3	25.0	–	–
POV-salt	0.8	–	1.7	–
POV-oil droplets	–	–	0.2	0.2
Cooking loss				
PL-jelly	–	7.4[b]	–	8.3[b]
PL-fat	–	2.7[c]	–	–

[a] Percent object volumes: POV, percent object volume (%); PL, percent loss (%).
[b] Percent loss of expressible fluid segregated from the cooked emulsion.
[c] Percent loss of fat segregated from the cooked emulsion.

Table 3
Three dimensional μCT geometric parameters for the raw and cooked samples of meat emulsions containing either lard fat or sunflower oil.

Parameter[a]	Lard raw	Lard cooked	Sunflower oil raw	Sunflower oil cooked
Meat matrix				
P-meat matrix	26.1[b]	35.6[b]	1.9[b]	5.0[b]
DA-meat matrix	0.45[c]	1[c]	0.12[c]	0.16[c]
ST-meat matrix	80.16	62.97	152.25	119.80
Pores[d]				
MV-fat	$3.2350 \cdot 10^5 \pm 1.7628 \cdot 10^7$	$1.7637 \cdot 10^5 \pm 1.6865 \cdot 10^7$	–	–
MV-jelly	–	$1.1297 \cdot 10^5 \pm 3.5930 \cdot 10^6$	–	$8.0778 \cdot 10^4 \pm 4.6515 \cdot 10^5$
MS-fat	$1.5344 \cdot 10^5 \pm 4.1755 \cdot 10^6$	$8.6519 \cdot 10^4 \pm 3.0862 \cdot 10^6$	–	–
MS-jelly	–	$7.6314 \cdot 10^4 \pm 1.2983 \cdot 10^6$	–	$8.0637 \cdot 10^4 \pm 2.6443 \cdot 10^5$
N-fat	173,995	341,994	–	–
N-jelly	–	49,072	–	63,750
SP-fat	0.7297 ± 0.1245	0.7848 ± 0.12	–	–
SP-jelly	–	0.6488 ± 0.1305	–	0.8055 ± 0.1388

[a] Quantitative parameters: P, porosity (%); DA, degree of anisotropy (dimensionless); ST, structure thickness (μm); MV, mean volume (μm^3); MS, mean surface area (μm^2); N, number of objects (dimensionless); SP, sphericity (dimensionless).
[b] Pores include fat globules, salt, oil droplets and expressible fluid within the protein network.
[c] DA is scaled such that a perfectly isotropic cylinder has the value 0, and the most anisotropic structure (the cooked lard sample) has the value 1.
[d] Results are given by the mean ± the standard deviation.

complementary contrasts were obtained, making it possible to distinguish expressible fluid from the protein network in the emulsions. Without the three modalities obtained from the grating-based technique, deriving microstructural parameters would not be feasible. The X-ray technique is presently the only one allowing for all three modalities and therefore shows great potential for imaging the microstructure of both meat emulsions and other food related products.

For the analysis of the data, a segmentation method based on Gaussian mixture models and MRF labeling with graph cuts was implemented. Quantitative parameters that represent the emulsion structure were then extracted. These parameters include the POVs of the different constituents and the porosity, degree of anisotropy and average structure thickness of the protein network. The results confirmed the difference in homogeneity of the protein network, which had already been inspected visually. As this study was limited to a single sample of each emulsion type due to limited beamtime no attempts were made to compare these findings with other quality parameters such as texture profile measurements, color composition, sensory panel evaluation, and apparent viscosity. Nevertheless, it has been shown that grating based X-ray imaging combined with multivariate contextual segmentation is a feasible method for the investigation of microstructural changes of meat emulsions due to heat treatment, and can serve as a valuable tool for further investigations.

Acknowledgments

References

Álvarez, D., & Barbut, S. (2013). Effect of inulin, β-glucan and their mixtures on emulsion stability, color and textural parameters of cooked meat batters. *Meat Science, 94*(3), 320–327.
Álvarez, D., Xiong, Y. L., Castillo, M., Payne, F. A., & Garrido, M.D. (2012). Textural and viscoelastic properties of pork frankfurters containing canola–olive oils, rice bran, and walnut. *Meat Science, 92*(1), 8–15.
Barbut, S. (1995). Importance of fat emulsification and protein matrix characteristics in meat batter stability. *Journal of Muscle Foods, 6*, 161–177.
Bech, M., Bunk, O., Donath, T., Feidenhans'l, R., David, C., & Pfeiffer, F. (2010). Quantitative x-ray dark-field computed tomography. *Physics in Medicine and Biology, 55*(18), 5529.
Bech, M., Jensen, T. H., Bunk, O., Donath, T., David, C., Weitkamp, T., et al. (2010). Advanced contrast modalities for X-ray radiology: Phase-contrast and dark-field imaging using a grating interferometer. *Zeitschrift für Medizinische Physik, 20*, 7–16.
Boykov, Y., Veksler, O., & Zabih, R. (2001). Fast approximate energy minimization via graph cuts. *IEEE Transactions on Pattern Analysis and Machine Learning, 23*(11), 1222–1239.
Choi, Y. S., Choi, J. H., Han, D. J., Kim, H. Y., Lee, M.A., Kim, H. W., et al. (2009). Characteristics of low-fat meat emulsion systems with pork fat replaced by vegetable oils and rice bran fiber. *Meat Science, 82*(2), 266–271.
Choi, Y. S., Choi, J. H., Han, D. J., Kim, H. Y., Lee, M.A., Kim, H. W., et al. (2010). Optimization of replacing pork back fat with grape seed oil and rice bran fiber for reduced-fat meat emulsion systems. *Meat Science, 84*(1), 212–218.
David, C., Nohammer, B., Solak, H. H., & Ziegler, E. (2002). Differential x-ray phase contrast imaging using a shearing interferometer. *Applied Physics Letters, 81*(17), 3287–3289.
Gordon, A., & Barbut, S. (1991). Raw meat batter stabilization: Morphological study of the role of interfacial protein film. *Canadian Institute of Food Science and Technology Journal, 24*(3), 136–142.
Hastie, T., Tibshirani, R., & Friedman, J. H. (2009). *The elements of statistical learning* (2nd ed.)New York: Springer (Chapter 8).
Jensen, T. H., Böttiger, A., Bech, M., Zanette, I., Weitkamp, T., Rutishauser, S., et al. (2011). X-ray phase-contrast tomography of porcine fat and rind. *Meat Science, 88*(3), 379–383.
Jones, K. W., & Mandigo, R. W. (1982). Effects of chopping temperature on the microstructure of meat emulsions. *Journal of Food Science, 47*, 1930–1935.
McDonald, S. A., Marone, F., Hintermuller, C., Mikuljan, G., David, C., Pfeiffer, F., et al. (2009). Advanced phase-contrast imaging using a grating interferometer. *Journal of Synchrotron Radiation, 16*, 562–572.
Miklos, R., Xu, X., & Lametsch, R. (2011). Application of pork fat diacylglycerols in meat emulsions. *Meat Science, 87*, 202–205.
Momose, A. (2003). Phase-sensitive imaging and phase tomography using X-ray interferometers. *Optical Express, 11*(19), 2303–2314.
Nielsen, M. S., Lauridsen, T., Thomsen, M., Jensen, T. H., Bech, M., Christensen, L. B., et al. (2012). X-ray tomography using the full complex index of refraction. *Physics in Medicine and Biology, 57*(19), 5971.
Pfeiffer, F. (2012). Milestones and basic principles of grating-based X-ray and neutron phase-contrast imaging. *AIP Conference Proceedings, 1466*, 2–11.
Pfeiffer, F., Bech, M., Bunk, O., Kraft, P., Eikenberry, E. F., Brönnimann, Ch., et al. (2008). Hard-X-ray dark-field imaging using a grating interferometer. *Nature Materials, 7*, 134–137.
Pfeiffer, F., Weitkamp, T., Bunk, O., & David, C. (2006). Phase retrieval and differential phase-contrast imaging with low-brilliance X-ray sources. *Nature Physics, 2*, 258–261.
Santos-Garcés, E., Laverse, J., Gou, P., Fulladosa, E., Frisullo, P., & Del Nobile, M.A. (2012). Feasibility of X-ray microcomputed tomography for microstructure analysis and its relationship with hardness in non-acid lean fermented sausages. *Meat Science, 93*, 639–644.
Sedgewick, R. (1998). *Algorithms in C* (3rd ed.): Addison-Wesley, 11–20.
Shao, J. H., Zou, Y. F., Xu, X. L., Wu, J. Q., & Zhou, G. H. (2011). Evaluation of structural changes in raw and heated meat batters prepared with different lipids using Raman spectroscopy. *Food Research International, 44*(9), 2955–2961.
Sorapukdee, S., Kongtasorn, C., Benjakul, S., & Visessanguan, W. (2012). Influences of muscle composition and structure of pork from different breeds on stability and textural properties of cooked meat emulsion. *Food chemistry, 138*, 1892–1901.
Tornberg, E. (2005). Effects of heat on meat proteins — Implications on structure and quality of meat products. *Meat Science, 70*, 493–508.
Totosaus, A., & Pérez-Chabela, M. L. (2009). Textural properties and microstructure of low-fat and sodium-reduced meat batters formulated with gellan gum and dicationic salts. *LWT—Food Science and Technology, 42*(2), 563–569.
Vural, H., Javidipour, I., & Ozbas, O. O. (2004). Effects of interesterified vegetable oils and sugarbeet fiber on the quality of frankfurters. *Meat Science, 67*, 65–72.

Weitkamp, T., David, C., Kottler, C., Bunk, O., & Pfeiffer, F. (2006). Tomography with grating interferometers at low-brilliance sources. *In Optics & Photonics. International Society for Optics and Photonics* (pp. 63180S–63180S).

Weitkamp, T., Diaz, A., David, C., Pfeiffer, F., Stampanoni, M., Cloetens, P., et al. (2005). X-ray phase imaging with a grating interferometer. *Optical Express*, *13*(16), 6296–6304.

Wood, J.D., Richardson, R. I., Nute, G. R., Fisher, A. V., Campo, M. M., Kasapidou, E., et al. (2004). Effects of fatty acids on meat quality: A review. *Meat Science*, *66*, 21–32.

Wu, M. G., Xiong, Y. L., Chen, J., Tang, X. Y., & Zhou, G. H. (2009). Rheological and microstructural properties of porcine myofibrillar protein-lipid emulsion composite gels. *Journal of Food Science*, *74*, E207–E217.

Youssef, M. K., & Barbut, S. (2009). Effects of protein level and fat/oil on emulsion stability, texture, microstructure and color of meat batters. *Meat Science*, *82*(2), 228–233.

Youssef, M. K., & Barbut, S. (2010). Physicochemical effects of the lipid phase and protein level on meat emulsion stability, texture, and microstructure. *Journal of food science*, *75*(2), S108–S114.

Novel X-ray phase-contrast tomography method for quantitative studies of heat induced structural changes in meat

Novel X-ray phase-contrast tomography method for quantitative studies of heat induced structural changes in meat

Rikke Miklos [a,*], Mikkel Schou Nielsen [b], Hildur Einarsdóttir [c], Robert Feidenhans'l [b], René Lametsch [a]

[a] *Department of Food Science, Faculty of Science, University of Copenhagen, Frederiksberg C, Denmark*
[b] *Niels Bohr Institute, Faculty of Science, University of Copenhagen, Copenhagen, Denmark*
[c] *Department of Applied Mathematics and Computer Science, Technical University of Denmark, Kgs. Lyngby, Denmark*

ARTICLE INFO

ABSTRACT

The objective of this study was to evaluate the use of X-ray phase-contrast tomography combined with 3D image segmentation to investigate the heat induced structural changes in meat. The measurements were performed at the Swiss synchrotron radiation light source using a grating interferometric setup. The non-destructive method allowed the same sample to be measured before and after cooking. Heat denaturation resulted in a 36% decrease in the volume of the muscle fibers, while solubilization of the connective tissues increased the volume from 8.4% to 24.9%. The cooking loss was quantified and separated into a water phase and a gel phase formed by the sarcoplasmic proteins in the exudate. The results show that X-ray phase contrast tomography offers unique possibilities in studies both the meat structure and the different meat component such as water, fat, connective tissue and myofibrils in a qualitative and quantitative manner without prior sample preparation as isolation of single muscle components, calibration or histology.

© 2014 Elsevier Ltd. All rights reserved.

1. Introduction

Cooking of meat results in immediate and extensive structural changes of the meat proteins. These conformational changes are caused by the denaturation of the different meat proteins and include transversal and longitudinal shrinkage of the muscle fibers, aggregation and gel formation of the sarcoplasmic proteins and the shrinkage and solubilization of the connective tissue (Tornberg, 2005). The structural alterations are affected by heating time and temperature and are determinant of the eating quality of the meat (Christensen, Bertram, Aaslyng, & Christensen, 2011). The heat induced structural changes of meat are conventionally studied by microscopy or indirect quantitative methods as differential scanning calorimetry (DSC), turbidity measurements or protein solubility.

During the last decades X-ray computed tomography (CT) has generated interest as a valuable method in non-destructive three-dimensional imaging of microstructure of meat (Frisullo, Marino, Laverse, Albenzio, & Del Nobile, 2010; Furnols, Teran, & Gispert, 2009; Hollo, Szucs, Tozser, Hollo, & Repa, 2007) and meat products (Frisullo, Laverse, Marino, & Del Nobile, 2009; Santos-Garces et al., 2013). CT has shown to be able to visualize the content and distribution of lean meat, bones and fat, whereas detection of connective tissue is challenged by similarities in attenuation of connective tissue and muscle fibers. Recently, a novel grating based X-ray phase-contrast tomographic method with increased contrast has been demonstrated (Bech et al., 2010; Weitkamp et al., 2005). Where the image contrast formation in absorption tomography is based on differences in attenuation of the X-rays, the phase-contrast modality uses the refraction of X-rays caused by variation in electron densities for image generation, which results in improved contrast towards differences in mass density in soft tissues and serves to overcome challenges caused by similar attenuation properties of sample components. The superior contrast for soft tissues provided by X-ray phase-contrast CT compared to absorption CT has been demonstrated in a study of pork fat and rind (Jensen et al., 2011). With the use of phase-contrast even small density variations in the rind and variation in the fatty acid composition within the fat fraction were detected indicating the potential of the use of the phase-contrast modality in structure studies of meat.

The objective of this study was to evaluate the potential of the use of X-ray phase-contrast tomography to study the heat induced changes in the structure of meat. The non-destructive characteristics of the method allowed the same sample to be measured before and after heat treatment. The measurements were performed at a synchrotron facility with a grating interferometric setup. Advanced data segmentation allowed quantitative parameters as changes in volume of myofibrils and connective tissue, gel formation and cooking loss to be extracted from the data.

---

* Corresponding author. Tel.: +45 35333263.
E-mail addresses: miklos@food.ku.dk (R. Miklos), schou@nbi.ku.dk (M.S. Nielsen), hildr@dtu.dk (H. Einarsdóttir), robert@nbi.ku.dk (R. Feidenhans'l), rla@food.ku.dk (R. Lametsch).

2. Materials and methods

2.1. Sample preparation

One piece of raw beef *Semimembranosus* bought in the local supermarket was cut to fit into a 1.5 mL sample tube (Ø = 10 mm). The meat was placed with the fiber direction longitudinal to the tube. When placed in the tube, the lid was closed under the surface of degassed PBS buffer (0.01 M phosphate buffered saline, 0.138 M NaCl, 2.7 mM KCl, pH 7,4; Sigma-Aldrich) to avoid air bubble formation during the measurements. After measurements of the raw sample the exact same sample was heat treated by placing the sample tube in a glass of hot water (95 °C) for 30 min. After heat treatment the sample was cooled in tab water for 15 min and subsequently measured again.

2.2. X-ray tomography

Absorption and phase-contrast CT scans of the sample were obtained by use of a grating interferometer setup at the TOMCAT beam line, Swiss Light Source (SLS) at the Paul Scherrer Institute (PSI). The technique has been explained previously elsewhere (Bech et al., 2010), and the setup is described in detail in McDonald et al. (2009). Measurements were made at a photon energy of 25 keV and the third Talbot fractional distance was used (Weitkamp, David, Kottler, Bunk, & Pfeiffer, 2006) with a grating period of the phase-grating, called G1, of 3.9 μm and a period of 2 μm of the analyzer grating, called G2. The height of the grating lines was designed for photon energy of 25 keV. The sample was kept in a water bath during the measurements in order to reduce the difference in refractive index between the sample container and its surroundings. The scan time was around 90 min per tomogram, and three tomograms were conducted at three different heights in the sample. The volume of the sample in each tomogram was 0.25 mL giving a full volume of around 0.75 mL imaged per sample. Each volume consists of 1720 × 1720 × 513 voxels with an effective voxel size of 7.4 μm × 7.4 μm × 7.4 μm. Due to limited allocated time on the beamline only one sample was measured.

2.3. Data processing

The X-ray tomograms were reconstructed at the TOMCAT beam line using a local implementation of the filtered back-projection algorithm for absorption and phase-contrast tomography as described in Pfeiffer, Kottler, Bunk, and David (2007). The phase-contrast intensity values were calibrated to absolute electron density values through a linear regression using the sample container consisting of polyethylene and the surrounding water as references. The spatial resolution in the phase contrast images was estimated to be 23 μm by using the edge between container and surrounding water as a reference.

2.4. Data segmentation

A two-step segmentation algorithm was implemented as described in Grau, Downs, and Burgoyne (2006). The first step is to model the data as a mixture of Gaussians using an expectation–maximization (EM) algorithm (Dempster, Laird, & Rubin, 1977). This iterative process finds the maximum likelihood of parameters where the model depends on unobserved latent variables. The spatial information of the data is then incorporated into the segmentation process by modeling the data as a Markov random field (MRF) (Li, 2003). It models the a priori probability of neighborhood dependencies, and the field can either be isotropic or anisotropic. For the segmentation of connective tissue, the local information of the structure orientation and coherence is extracted to steer the smoothing (anisotropy) of the final segmentation. The MRF smoothing parameter β was set to 0.7.

3. Results and discussion

Absorption and phase contrast images of transverse cut of the raw and cooked beef sample are presented in Fig. 1. The grayscale images are reconstructed from a single slice of the data sets. The dark ring surrounding the samples is the sample tube. The absorption images (Fig. 1A+B) appear noisy and hardly any contrast between the muscle components is seen. In the absorption image of the raw meat (Fig. 1A) only the intra muscular fat can be separated from the muscle structure. In the cooked meat (Fig. 1B) the structure of the muscle fibers and connective tissue is faintly observed. In comparison, superior contrast is provided in the phase contrast images (Fig. 1C+D), where muscle fibers, connective tissue, intra muscular fat and the surrounding water phase appear clearly separated. In the phase contrast images intensity differences reflect differences in electron density of the structural components where the light intensity increases with increasing densities. In the raw meat (Fig. 1C) the muscle fiber part of the muscle is represented by the gray areas, whereas the connective tissue, mainly the perimysium, is the white areas. The small black spots are intramuscular fat. Towards the edge of the samples darker gray areas are seen representing a water phase. Due to changes in electron density of the muscle components as a consequence of heating an intensity shift is seen in the image of the cooked sample (Fig. 1, D) compared to the raw sample. In the cooked sample muscle fibers have contracted and thus increased in density, which is seen as the white areas: The connective tissue has decreased in density due to absorption of water and appears as light gray. The most remarkable changes in the structure are the shrinkage of both the total sample volume and the individual fiber bundles. In the cooked sample the fiber bundles appear clearly separated by the surrounding perimysium. The shrinkage of the myofibrils has forced water to be expelled, which can be observed as an increase in the
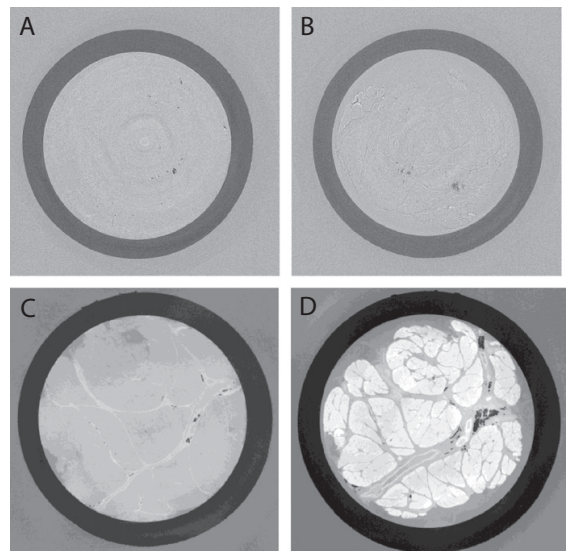

Fig. 1. Transverse sample cut reconstructed from the absorption (A+B) and the phase contrast (C+D) tomograms of raw (A+C) and cooked beef (B+D). In A+B the contrast is formed by differences in absorption of the X-rays by the sample components. Only fat (black) can be separated from the muscle (gray). In C+D the contrast is formed based on differences in refraction of the X-rays caused by differences in the electron density of the sample components. In C the components can be identified as: muscle (gray), fat (black), connective tissue (white), water (dark gray). In D the components can be identified as muscle (white), connective tissue (light gray), water (dark gray) and fat (black).

area of the water phase surrounding the meat. The area of the perimysium is increased indicating partly solubilization.

From the 3D data sets the observed difference in microstructure can be further explored by data segmentation of the full sample volumes. Due to the limited contrast provided from the absorption tomograms, the quantitative analysis were only performed on the phase contrast data sets. A 3D visualization of the segmented X-ray phase contrast tomograms of the raw and cooked beef is presented in Fig. 2A+B. An example of a segmented slice of the raw and cooked sample from the phase contrast tomograms is presented in Fig. 3A+B respectively, while the quantitative distribution of the structure components is presented in the corresponding histograms in Fig. 3C+D. From Fig. 3, A+C it is seen that the main components water (blue), muscle fibers (red) connective tissue (pink) and intra muscular fat (white) can be clearly separated. The use of the two-step data segmentation procedure further enabled segmentation of structural variations within these components, even though that no clear peak separation is observed in the histograms (Grau et al., 2006). In the raw sample (Fig. 3A) the muscle fibers from the inner and outer part of the sample can be separated into two populations based on differences in the electron densities. The outer part of the muscle fibers has a lower electron density compared to the inner part (Fig. 3C). This difference can be explained by an increase in the water binding capacity in the meat exposed to the surrounding buffer that had a relatively high pH (7.4) (Puolanne & Halonen, 2010). In the cooked meat shrinkage of the muscle fibers resulted in an increase in the electron density (Fig. 3D) compared to the raw sample (Fig. 3C). No difference between the inner and outer part is observed in the cooked sample as the shrinkage has forced the extra cellular water to be expelled as cooking loss. The connective tissue is segmented into two different populations. As seen in Fig. 3A+C this is mainly based on local variation in the electron densities of the perimysium in the junctions of the fiber bundles. The increase in the area of the connective tissue in the cooked sample compared to the raw sample indicating partly solubilization is further supported by the decrease in electron density of this component. This demonstrates that the meat has been undergoing a relatively severe heat treatment and reached a temperature above 80 °C and has started to gelatinize (Tornberg, 2005). In the water phase local variations in the protein content, ascribed to expelled sarcoplasmic proteins, result in two different populations that enable separation of the water phase based on the protein content. However, a strict division in exudate from the meat and the surrounding buffer is not possible. In Fig. 3 these water populations are designated as Water 1 and Water 2, where Water 2 has the highest protein content. In the raw sample the surrounding water phase is mainly constituted by buffer, but a small amount of exudate are detected in the regions at the surface of the meat. In the cooked sample the cooking loss results in an increase in the volume of the water phase, where the Water 2 population most likely will consist of a gel formed by expelled denatured sarcoplasmic proteins (Davey & Gilbert, 1974; Tornberg, 2005).

The volume changes of the main components are summarized in Table 1. In the table the volumes of the gel-like structure are included in the water phase. The observed heat induced changes in the muscle structure are similar to previously observations on the subject studied by other imaging methods as microscopy (Bendall & Restall, 1983; Tornberg, 2005) or MRI (Bouhrara et al., 2011). Compared to microscopy both MRI and X-ray tomography are non-destructive and three dimensional methods. Whereas, X-ray phase contrast tomography provides information about the electron density MRI, which is based on information about the proton density.

The superior contrast provided by phase contrast imaging compared to standard X-ray absorption imaging has previously been demonstrated by Jensen et al. (2011) in porcine fat and rind. Together with the present result for raw and cooked meat it is emphasized that the phase contrast modality is advantageous in the use of X-ray tomography for structure studies of meat as the small variation in the atomic composition between the structural components is insufficient to provide an absorption based contrast between main components as connective tissue and muscle fibers, while the variations in electron densities result in a high contrast even between structural deviations within the individual components, which demonstrates the potential of the method. Besides a better understanding of the interactions between the denaturation of the muscle fibers and the connective tissue, phase contrast X-ray tomography may be applied in studies of processing steps as salting, marinating, freezing or heating, that will result in changes in the electron density of the muscle fibers either caused by denaturation or affected water binding capacity. As indicated in the quantitative analysis of this study, increased water binding as a consequence of increased pH and salt affected the electron densities sufficiently to be detected.

In addition to monitoring of processing steps the non-destructive characteristics also contribute to the potential in relation to on-line selection of raw materials as fat, muscle and connective tissue can be non-invasively detected and quantified. Quality deteriorations as soft fat or PSE/DFD meat may be linked to variations in the electron density and used as marker in specifications for rejection or selection of raw materials for a specific production.

4. Conclusion

Phase contrast tomography offers unique possibilities to study structural changes of meat caused by cooking. The non-destructive characteristics of the method enabled studies to be made on the exact same sample before and after heat treatment. The high contrast in the data set made it possible to both visualize and quantify structural variation within the individual meat components. Even though the method might have an on-line potential, the relatively long measuring time currently limits the method to experimental purposes.
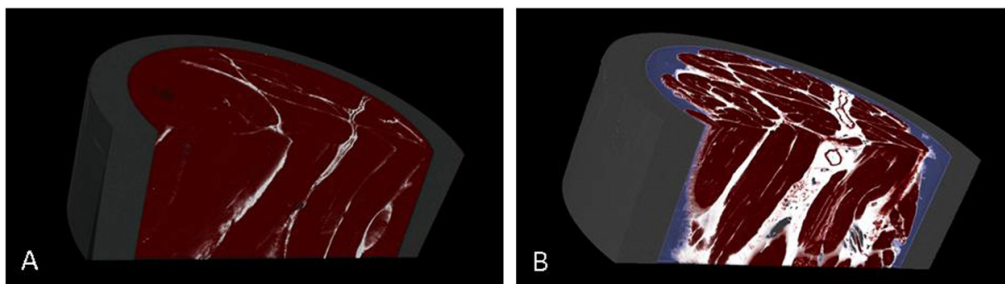

Fig. 2. 3D visualization of segmented X-ray phase contrast tomograms of raw (A) and cooked beef (B). Muscle tissue is shown in red, connective tissue in white, intramuscular fat in gray and the water phase is shown in blue.
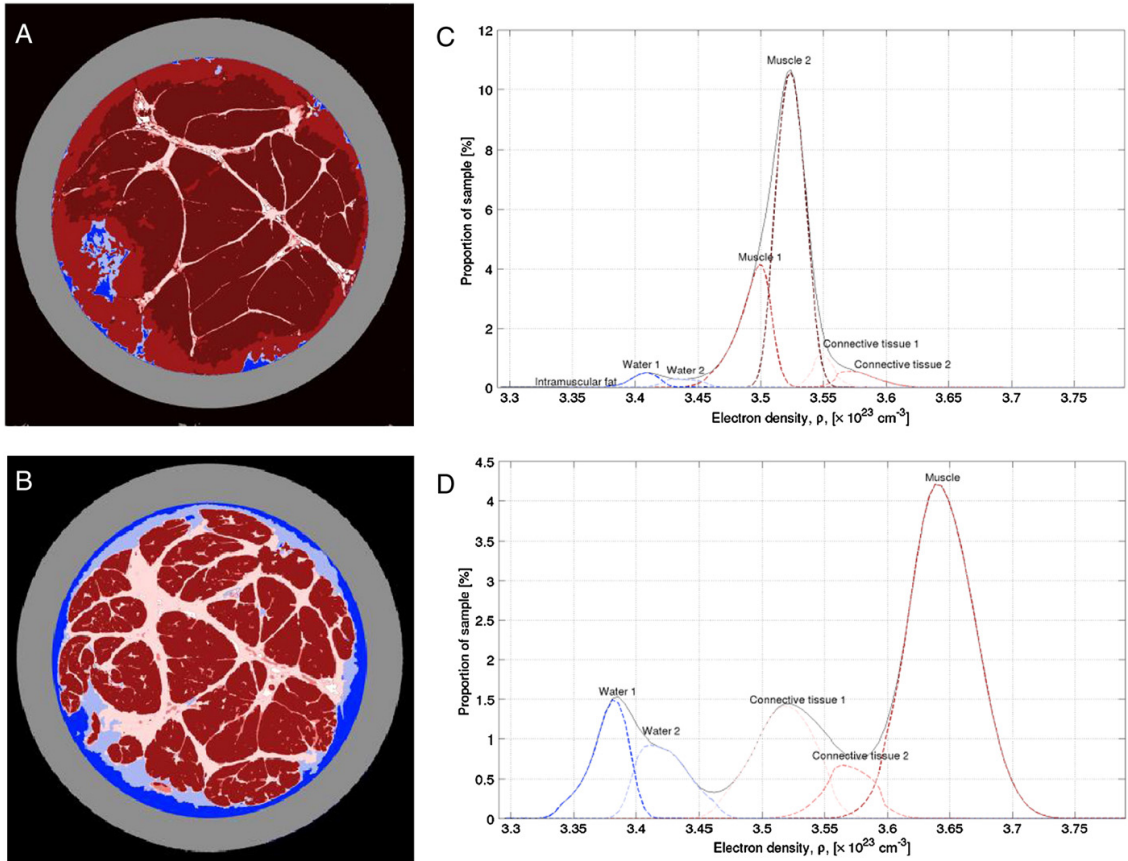
Fig. 3. Segmentation of beef sample in raw and cooked state. A+B: Examples of segmented slices from the datasets obtained from the raw and the cooked sample respectively. Muscle tissue is shown in red (1) or brown (2), connective tissue in light pink (1) or pink (2), water in blue (1) or light blue (2) and intramuscular fat in white. C+D: Histograms of the structure components generated from the full 3D data sets.

Table 1
Partial object volumes (POV) for the soft materials in the raw and cooked beef sample.

Component	Raw	Cooked
POV		
Water	4.87	19.54
Muscle fibers	86.18	54.96
Connective tissue	8.41	24.89
Intramuscular fat	0.54	0.61

References

Bech, M., Jensen, T. H., Bunk, O., Donath, T., David, C., Weitkamp, T., Le Duc, G., Bravin, A., Cloetens, P., & Pfeiffer, F. (2010). Advanced contrast modalities for X-ray radiology: Phase-contrast and dark-field imaging using a grating interferometer. *Zeitschrift für Medizinische Physik, 20*, 7–16.

Bendall, J. R., & Restall, D. J. (1983). The cooking of single myofibers, small myofiber bundles and muscle strips from beef M-Psoas and M-Sternomandibularis muscles at varying heating rates and temperatures. *Meat Science, 8*, 93–117.

Bouhrara, M., Clerjon, S., Damez, J. L., Chevarin, C., Portanguen, S., Kondjoyan, A., & Bonny, J. -M. (2011). Dynamic MRI and thermal simulation to interpret deformation and water transfer in meat during heating. *Journal of Agricultural and Food Chemistry, 59*, 1229–1235.

Christensen, L, Bertram, H. C., Aaslyng, M. D., & Christensen, M. (2011). Protein denaturation and water–protein interactions as affected by low temperature long time treatment of porcine Longissimus dorsi. *Meat Science, 88*, 718–722.

Davey, C. L., & Gilbert, K. V. (1974). Temperature-dependent cooking toughness in beef. *Journal of the Science of Food and Agriculture, 25*, 931–938.

Dempster, A. P., Laird, N. M., & Rubin, D. B. (1977). Maximum likelihood from incomplete data via the EM algotrithm. *Journal of the Royal Statistical Society. Series B (Methodological), 1–38.*

Frisullo, P., Laverse, J., Marino, R., & Del Nobile, M. A. (2009). X-ray computed tomography to study processed meat microstructure. *Journal of Food Engineering, 94*, 283–289.

Frisullo, P., Marino, R., Laverse, J., Albenzio, M., & Del Nobile, M. A. (2010). Assessment of intramuscular fat level and distribution in beef muscles using X-ray microcomputed tomography. *Meat Science, 85*, 250–255.

Furnols, M. F. I., Teran, M. F., & Gispert, M. (2009). Estimation of lean meat content in pig carcasses using X-ray computed tomography and PLS regression. *Chemometrics and Intelligent Laboratory Systems, 98*, 31–37.

Grau, V., Downs, J. C., & Burgoyne, C. F. (2006). Segmentation of trabeculated structures using an anisotropic Markov random field: Application to the study of the optic nerve head in glaucoma. *Medical Imaging, IEEE Transactions on, 25*(3), 245–255.

Hollo, G., Szucs, E., Tozser, J., Hollo, I., & Repa, I. (2007). Application of X-ray computer tomography (CT) in cattle production. *Asian-Australasian Journal of Animal Sciences, 20*, 1901–1908.

Jensen, T. H., Bottiger, A., Bech, M., Zanette, I., Weitkamp, T., Rutishauser, S., David, C., Reznikova, E., Mohr, J., Christensen, L. B., Olsen, E. V., Feidenhans'l, R., & Pfeiffer, F.

(2011). X-ray phase-contrast tomography of porcine fat and rind. *Meat Science, 88,* 379–383.

Li, S. Z. (2003). Modelling image analysis problems using Markow random fields. *Handbook of Statistics (S0073–6333), 21*(13), 473–513.

McDonald, S. A., Marone, F., Hintermuller, C., Mikuljan, G., David, C., Pfeiffer, F., & Stampanoni, M. (2009). Advanced phase-contrast imaging using a grating interferometer. *Journal of Synchrotron Radiation, 16,* 562–572.

Pfeiffer, F., Kottler, C., Bunk, O., & David, C. (2007). Hard X-ray phase tomography with low-brilliance sources. *Physical Review Letters, 98,* 108105.

Puolanne, E., & Halonen, M. (2010). Theoretical aspects of water-holding in meat. *Meat Science, 86,* 151–165.

Santos-Garces, E., Laverse, J., Gou, P., Fulladosa, E., Frisullo, P., & Del Nobile, M. A. (2013). Feasibility of X-ray microcomputed tomography for microstructure analysis and its

relationship with hardness in non-acid lean fermented sausages. *Meat Science, 93,* 639–644.

Tornberg, E. (2005). Effects of heat on meat proteins—Implications on structure and quality of meat products. *Meat Science, 70,* 493–508.

Weitkamp, T., David, C., Kottler, C., Bunk, O., & Pfeiffer, F. (2006). Tomography with grating interferometers at low-brilliance sources. *International Society for Optics and Photonics, 6.*

Weitkamp, T., Diaz, A., David, C., Pfeiffer, F., Stampanoni, M., Cloetens, P., & Ziegler, E. (2005). X-ray phase imaging with a grating interferometer. *Optics Express, 13,* 6296–6304.

Novelty detection of foreign objects in food using multi-modal X-ray imaging

ELSEVIER

CONTROL
FOOD CONTROL
CONTROL
CONTROL
CONTROL
CONTROL
CONTROL

CrossMark

Novelty detection of foreign objects in food using multi-modal X-ray imaging

Hildur Einarsdóttir [a, *], Monica Jane Emerson [a], Line Harder Clemmensen [a], Kai Scherer [b], Konstantin Willer [b], Martin Bech [b, c], Rasmus Larsen [a], Bjarne Kjær Ersbøll [a], Franz Pfeiffer [b, d]

[a] Department of Applied Mathematics and Computer Science, Technical University of Denmark, Richard Petersens Plads, Building 324, 2800 Kgs. Lyngby, Denmark
[b] Lehrstuhl für Biomedizinische Physik, Physik-Department & Institut für Medizintechnik, Technische Universität München, James-Franck-Straße 1, 85748 Garching, Germany
[c] Department for Medical Radiation Physics, Lund University, 22185 Lund, Sweden
[d] Institut für Diagnostische und Interventionelle Radiologie, Klinikum Rechts der Isar, Technische Universität München, 81675 München, Germany

ARTICLE INFO

ABSTRACT

In this paper we demonstrate a method for novelty detection of foreign objects in food products using grating-based multimodal X-ray imaging. With this imaging technique three modalities are available with pixel correspondence, enhancing organic materials such as wood chips, insects and soft plastics not detectable by conventional X-ray absorption radiography. We conduct experiments, where several food products are imaged with common foreign objects typically found in the food processing industry. To evaluate the benefit from using this multi-contrast X-ray technique over conventional X-ray absorption imaging, a novelty detection scheme based on well known image- and statistical analysis techniques is proposed. The results show that the presented method gives superior recognition results and highlights the advantage of grating-based imaging.

© 2016 Elsevier Ltd. All rights reserved.

1. Introduction

X-rays are increasingly used in the food production industry for quality control inspection (Haff & Toyofuku, 2008; Kwon, Lee, & Kim, 2008; Mery et al., 2011; Zwiggelaar, Bull, Mooney, & Czarnes, 1997). They provide a non-destructive method to quantitatively measure food quality traits and detect foreign objects. Foreign objects can be introduced to food products for instance from raw materials or due to malfunctioning of the production line. The detection of foreign objects is not only important in regards to consumer satisfaction, it is also required by regulations to secure consumer safety. In a recent survey of Japanese consumer complaints on contaminants in food, it was revealed that the most challenging foreign materials, which still cannot be adequately detected by conventional X-ray systems, are paper, wood chips, plastic, cartilage and insects (Takashi, 2009). Table 1 shows the contaminants most frequently complained about, and the difficulty level of detecting them using conventional X-ray techniques. Several hazardous contaminants such as blade chips, bones and glass fragments are classified at difficulty level medium, highlighting the need for a more effective detection method.

Recent advances in X-ray imaging have introduced new imaging modalities such as phase contrast and dark field contrast, obtainable by grating-based interferometry (Bech et al., 2010a; Pfeiffer, Weitkamp, Bunk, & David, 2006; Pfeiffer et al., 2008). These modalities have shown to produce enhanced contrast capabilities over the typical absorption X-ray modality (Bech et al., 2010b; Jensen et al., 2011; Pfeiffer et al., 2007). The grating-based approach allows for obtaining three imaging modalities simultaneously, with pixel correspondence. The modalities consist of conventional absorption X-ray, phase contrast imaging and dark-field imaging. A

* Corresponding author. Department of Applied Mathematics and Computer Science, Technical University of Denmark, Matematiktorvet Building 321, Room 223, 2800 Kgs. Lyngby, Denmark.
E-mail address: hildr@dtu.dk (H. Einarsdóttir).

Table 1
Japanese survey results for consumer contaminant complaints (Takashi, 2009) and the level of difficulty of detection with absorption X-ray techniques.

Contaminant	Percentage (%)	Difficulty of detection by X-ray
Insects	24.5	Difficult
Bone (calcified only)	15.2	Medium
Unclear	14.1	N/A
Metal piece	7.3	Easy
Hairs	6.6	Difficult
Needles, wires etc.	6.5	Easy
Plastic and rubber	5.3	Medium
Glass fragments	3.9	Medium
Stone and sand	3.0	Easy
Paper, threads etc.	2.1	Difficult
Vinyl	2.0	Difficult
Fly	1.8	Difficult
Wood chips	1.5	Difficult
Blade chips	1.2	Medium
Staples	1.0	Easy
Rat excrement	0.9	Difficult

Fig. 1. A schematic of a X-ray radiography setup using a grating interferometer.

recent study (Nielsen, Lauridsen, Christensen, & Feidenhans'l, 2013) presented a novel approach for visual detection of organic foreign bodies such as paper and insects in food products using X-ray dark-field imaging. Here, the dark-field modality gave larger contrast-to-noise ratios than absorption radiography for organic foreign objects.

In this paper we build upon these results and provide an extensive and thorough analysis of the novelty detection capabilities of the higher contrast obtained from grating-based X-ray imaging. The purpose of the study is to compare the detection rates between the multimodal X-ray data and conventional absorption X-ray. Additionally, a comparison of detection rates when using only intensity based information versus including texture features is conducted. A novelty detection scheme is developed based on image- and statistical analysis techniques. The algorithm first computes texture features of the image modalities. Next, a model of each food product is created by fitting a Gaussian Mixture Model (GMM) to either the image intensities alone or by including the texture features. Images with foreign bodies are then evaluated by calculating the Mahalanobis distance to the food models for all image pixels. Optimal thresholds for detecting foreign objects are then chosen to minimize false positives and maximize the true positive rate. To determine the gain of using grating-based imaging over conventional absorption radiography, the detection results of both methods are compared by the rates of detected foreign objects versus false positives. This is done both pixel-wise and on an object count bases. To test the novelty detection capabilities of the algorithm we investigate a wide range of foreign bodies of varying sizes in seven different food products. The chosen foreign bodies include objects typically found in the food processing industry that have proven problematic to detect using conventional X-ray techniques.

2. Materials and methods

2.1. Grating-based X-ray imaging

The grating-based interferometer is described in detail in Pfeiffer et al. (2006), (2008). The imaging modalities obtained by grating-based imaging (GBI) consist of three types of physical interactions — attenuation, refraction and scattering. These modalities are refered to as absorption, phase contrast and dark-field imaging, respectively. The setup for GBI is shown in Fig. 1. The phase grating produces a periodic intensity modulation consisting of periodic fringes transverse to the beam direction. The change in position, mean valu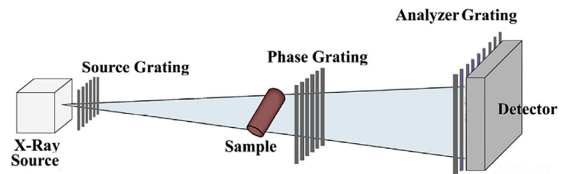e and amplitude of the periodic fringes can be probed using the analyzer grating by moving the source grating in steps through the period in the pattern while recording an image at each step. From this series of scans, the absorption, refraction and small-angle scattering can be recorded by a detector using the same exposures, giving an inherent pixel correspondence.

2.2. Data set

The data set used for training and testing the detection algorithm in this study consists of images of seven different food products (minced meat, steak, turkey schnitzel, salami slices, sliced cheese, wheat bread and rye bread). These products were chosen based on their range in texture homogeneity. The foreign objects used were chosen based on a survey conducted with industrial collaborators within the research project. Table 2 shows the list of foreign objects, along with their density and size. Fig. 2 shows the foreign objects in the three different size groups. In the experiment, a total of 7 food products with 8 different foreign object materials. Each image contains all the foreign objects from a single size group, giving in total 7 × 3 X-ray exposures, each exposure consisting of the three image modalities.

Projection images were obtained at a laboratory GBI setup located at the Chair of Biomedical Physics at the Technische Universität München. The effective energy used was 25 keV, with 9 steps of the phase grating and integration time of 2 s. From the raw data, the three imaging modalities were obtained by sine fitting as described in Bech et al. (2010c). The setup is described in detail in Scherer et al. (2014). The obtained image resolution is 800 × 800 pixels.

2.3. Detection algorithm

For a novelty detection task, the classification problem is concerned with identifying whether a pattern is part of the data or is in fact unknown. In other words it is sought to assign an 'abnormal' label to foreign objects within known 'normal' food products. Therefore, novelty detection only needs the known class for training purposes and usually a distance measure and a threshold for decision making. Both intensity and texture features are

Table 2
Foreign objects used to test the detection algorithm. Both the approximate density and thickness of each object is given.

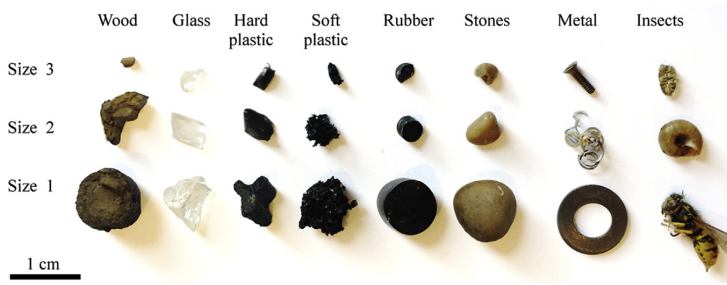| Type	Density (g/cm²)	Thickness (mm)		
		Size 1	Size 2	Size 3
Glass	2.62	5	3	2
Metal	3.82 to 7.82	2	1	0.5
Wood	0.63	6	4	2
Insects	0.12 to 0.47	5	3	2
Hard plastic	0.66	6	3	2
Soft plastic	0.30	5	3	2
Rubber	1.21	4	3	2
Stones	2.23 to 2.50	6	4	3

Fig. 2. Foreign objects used in the experiments. The objects consist of eight different materials in three size groups.

considered for the detection algorithm, and the extraction of these along with threshold selection is briefly discussed in the following sections.

2.3.1. Basic image features

Image texture can contain as important information as the image intensity, and one way of analyzing the image texture is by using Basic Image Features (BIFs). In Crosier and Griffin (2010) BIFs are described as a filter-response space of a set of seven Gaussian derivative filters. These responses describe distinct types of local image structure at a given scale, such as flatness, slopes and blob-like features. Two parameters can be optimized using this method, one is the sensitivity to flatness η, and the other determines the scale of the Gaussian filters, σ.

2.3.2. Gaussian mixture models

A way to incorporate both the intensity and texture features into a single model is to fit a multivariate statistical model, and one such model is the multivariate Gaussian. Given data $\boldsymbol{x} = (x_1,\ldots,x_k)$ of dimensions k, the multivariate Gaussian f_x is described in terms of the means. $\boldsymbol{\mu} = (\mu_1,\ldots,\mu_k)$ and covariance matrix Σ of the data as

$$\Phi(\boldsymbol{x}|\boldsymbol{\mu}, \Sigma) = \frac{1}{\sqrt{(2\pi)^k|\Sigma|}}\exp\left(-\frac{1}{2}(\boldsymbol{x}-\boldsymbol{\mu})^\top \Sigma^{-1}(\boldsymbol{x}-\boldsymbol{\mu})\right) \qquad (1)$$

$$= \frac{1}{Z}\exp\left(-\frac{1}{2}\log|\Sigma| - \frac{1}{2}(\boldsymbol{x}-\boldsymbol{\mu})^\top \Sigma^{-1}(\boldsymbol{x}-\boldsymbol{\mu})\right), \qquad (2)$$

where $|\Sigma|$ is the determinant of Σ. Homogeneous food products can be represented by a single multivariate Gaussian distribution. However, the more complex the food matrix, the worse this assumption holds. Food products such as ryebread will contain an extensive amount of texture, especially when containing seeds and other additives. Thus the Gaussian mixture model (GMM) is used to model these more complex food products. The mixture distribution of L Gaussians is given as

$$\boldsymbol{p}(\boldsymbol{x}) = \sum_{l=1}^{L} \boldsymbol{p}_l \Phi(\boldsymbol{x}|\mu_l, \Sigma_l) \qquad (3)$$

$$= \sum_{l=1}^{L} \frac{1}{Z}\exp\left(\log p_l - \frac{1}{2}\log|\Sigma_l| - \frac{1}{2}(\boldsymbol{x}-\mu_l)^T \Sigma_l^{-1}(\boldsymbol{x}-\mu_l)\right), \qquad (4)$$

where p_l is the prior probability of each mixture. The mixture model can be estimated using the Expectation-Maximization (EM) algorithm, which is an iterative method for finding the maximum a posteriori estimates of parameters in the mixture model (Dempster, Laird, & Rubin, 1977).

2.3.3. Mahalanobis distance maps

Given a multivariate Gaussian, the pixel-wise Mahalanobis distance can be calculated. The Mahalanobis distance is a unitless measure introduced in Mahalanobis (1936). It is a descriptive statistic giving the relative distance measure of a data point's residual from a common point. It is similar to the Euclidean distance, differing in that it takes into account the correlations of the data set and is scale-invariant. The Mahalanobis distance is given by

$$D^2 = (\boldsymbol{x}-\boldsymbol{\mu})^\top \Sigma^{-1}(\boldsymbol{x}-\boldsymbol{\mu}). \qquad (5)$$

Given an image and GMM, we can calculate the Mahalnobis distance for each image pixel i to each Gaussian in the GMM. The Mahalanobis distance map will show regions of deviation from the food model in greater intensity, highlighting areas of potential foreign objects.

2.3.4. Threshold selection

For the one class classifier a threshold value θ must be chosen to determine if an image pixel belongs to the target class, food, or is in fact a foreign object. For each pixel i, if the Mahalanobis distance D^2 is smaller than θ, it is classified as the target class, and as a foreign object otherwise. A foreign object pixel is represented as positive, and the false positive versus the true positive rate is sensitive to the threshold value, and must therefore be carefully chosen. The aim is to eliminate false positives whilst maintaining a high true positive rate. The threshold can thus be chosen by evaluating the cost impact of discarding food products falsely determined to contain foreign objects versus retaining products that do contain foreign objects.

2.3.5. Algorithm

An overview of the proposed novelty detection algorithm is summarized in the following steps:

Training step.

1. Calculate BIFs for food product at a chosen scale, σ, and with given flatness parameter, η,
2. Calculate GMM with chosen number of Gaussians.
3. Determine threshold value for classification.

Testing step.

1. X-ray images acquired for new data.
2. Calculate BIFs with same scale and flatness parameter as used for training.
3. Calculate Mahalanobis distance of each pixel.

4. Apply threshold and filter detected objects of size smaller than a given limit.

3. Results and discussion

Fig. 3 shows an example of images obtained of minced meat, where all three modalities are shown along with their intensity histograms. The modalities capture different details of the minced meat, where absorption shows shadowing due to X-ray attenuation, and phase contrast and dark field enhance the edge details. Fig. 4 shows the X-ray images captured of turkey, with foreign objects from size group 1 present. Additionally, normalized gray profiles at the 250th row of each image is shown to illustrate the contrast differences obtained. An example of images obtained of all food products with foreign objects from size group 2 is given in Fig. 5. It is clearly visible that different contrast is obtained in the three imaging modalities.

3.1. Contrast-to-noise ratios

As an initial comparison of detection results from the three different X-ray modalities, the Contrast-to-Noise Ratio (CNR) was calculated for each foreign object. This contrast measure is defined in Song et al. (2004) and is given by

$$CNR = |\mu_{FB} - \mu_M| \Big/ \left(w_{FB}\sigma_{FB}^2 + w_M\sigma_M^2 \right)^{1/2}, \qquad (6)$$

where μ denotes the mean value and σ^2 is the variance of the foreign object (FB) pixels and food matrix (M) pixels in the images. The area covered by the foreign objects and food matrix differ in the images, therefore the variances are weighted with the factor w which is given by the ratio of the number of pixels of the foreign object or food matrix, relative to the total number of the two. A high CNR value represents a high contrast compared to noise, whereas a low value means there is no significant contrast.

The resulting CNRs are given in Table 3, where the average CNR value for each foreign object is given across all food products. The CNR for glass, metal and stone are significantly higher in the absorption modality compared to the other two. However, for the organic foreign objects, the dark-field modality gives a higher CNR. It is worth noting that the lowest CNR is obtained for rubber making it the most difficult to detect in any of the modalities. The CNR value for phase contrast is quite low as it is not a suitable metric for the modality. Post-processing the images by integration should enhance the CNR values.

3.2. Model comparison

Next, the comparison of constructed food models is made, and to simplify the task, a single Gaussian was fitted to each of the seven food products. This was done either by a) fitting a univariate Gaussian to each of the image modalities (in total three different models), b) a three-dimensional Gaussian fitted to all image modalities, or c) a 66-dimensional Gaussian fitted to the image modalities and texture features (BIF features from 7 filters at three scales are calculated for each image modality, giving in total 63 texture features). In total 5 models where constructed containing features as given in Table 4.

Fig. 6 shows receiver operating characteristic (ROC) curves for the five models for both sliced cheese and rye bread. Here, all foreign objects have been included. The curves show the fraction of true positive pixels (foreign object pixels) out of the actual positives (true positive rate = TPR) versus the fraction of false positives pixels (food product pixels) out of total actual negatives (false positive rate = FPR), at various threshold settings of θ. For perfect classification, the curve should yield a point in the upper left corner at coordinate (0,1) of the ROC space, representing no false negatives or false positives. A random classifier would give a diagonal line from the bottom left to the top right corners. The marker on each curve represents the minimum distance to perfect classification. The ROC curves reveal that the detection rate of the phase contrast model is lowest in both food products. However, a significant gain is present when comparing the dark-field and absorption models. The
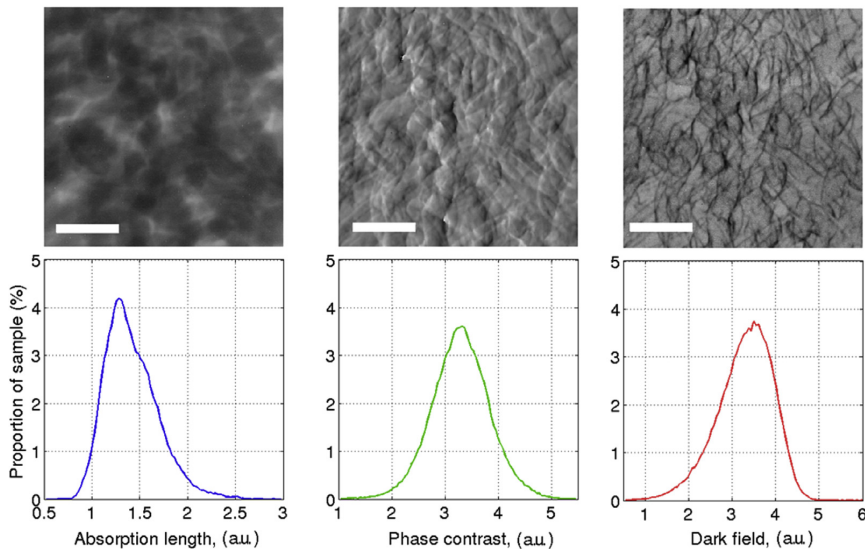

Fig. 3. All three imaging modalities shown for minced meat along with intensity histograms. From left to right: Absorption, phase contrast and dark-field. The white bar represents 0.5 cm.
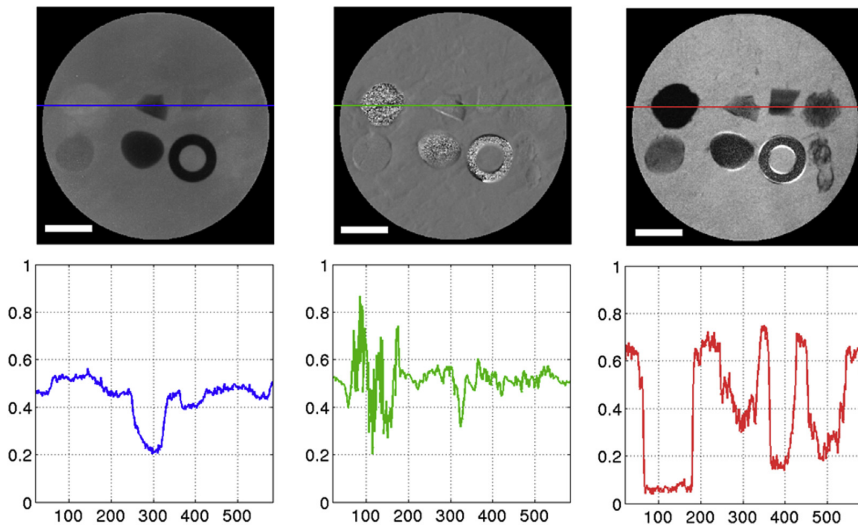
Fig. 4. Normalized gray profile at 250th row of image modalities. From left to right: Absorption, phase contrast and dark-field. The white bar represents 1 cm.
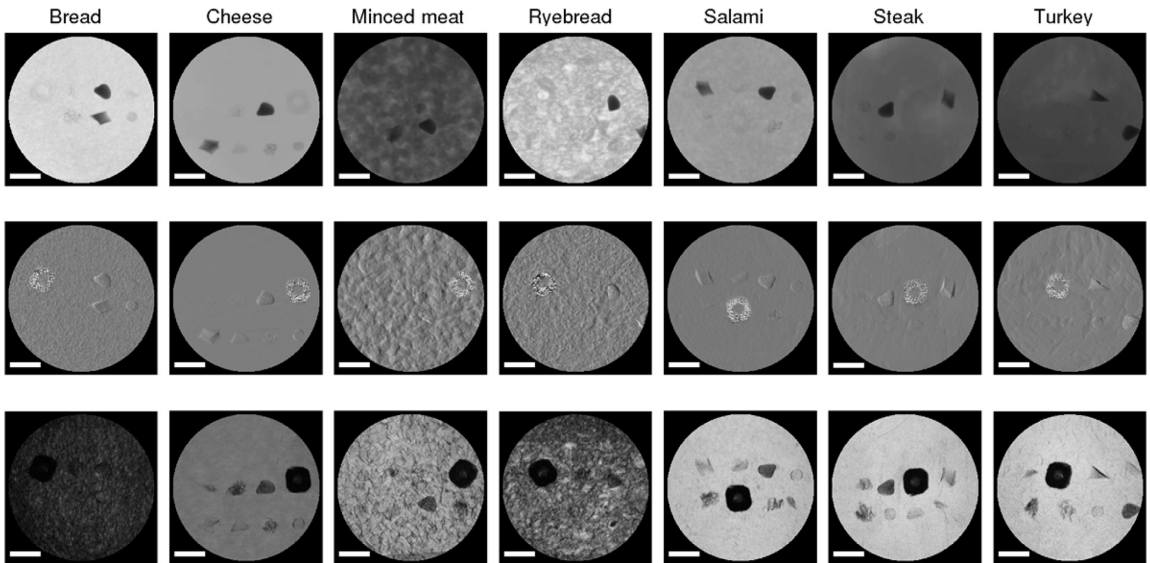

Fig. 5. Images obtained for all food products with foreign objects from size group 2 present. Top: Absorption modality; Middle: Phase contrast modality; Bottom: Dark-field modality. The white bar represents 1 cm.

Table 3
Contrast-to-noise ratios of foreign bodies, compared between imaging modalities.

	Glass	Rubber	Metal	Stone	Hard plastic	Soft plastic	Insect	Wood
Absorption	**39.94**	**13.38**	**62.65**	**64.27**	10.12	4.24	5.85	6.02
Phase contrast	4.52	1.60	8.39	4.76	1.45	1.46	1.43	7.01
Dark-field	10.67	11.44	22.39	39.29	**17.76**	**25.91**	**19.58**	**49.88**

multivariate models also result in a higher TPR, while adding the texture features gives overall a slight advantage. Table 5 gives the

minimum distance to perfect classification for all models and all food products. For all products, except rye bread and minced meat,

Table 4
The different features incorporated in the five food models.

	Absorption	Phase contrast	Dark field	Texture features
Model 1	×			
Model 2		×		
Model 3			×	
Model 4	×	×	×	
Model 5	×	×	×	×

pixels. The sensitivity (TPR = TP/(TP + FN)), specificity (SPC = TN/(FP + TN)) and accuracy (ACC = (TP + TN)/(TP + FP + TN + FN)), is also given. In all cases the sensitivity, specificity and accuracy is lowest for model 1 (absorption alone), giving at average TPR = 65.5%, SPC = 83.6% and ACC = 81.7%. For model 4 (multivariate intensity) the averages are TPR = 87.4%, SPC = 93.8% and ACC = 93.0%, and likewise for model 5 (combined intensity and texture features) the averages are TPR = 88.9%, SPC = 92.7% and

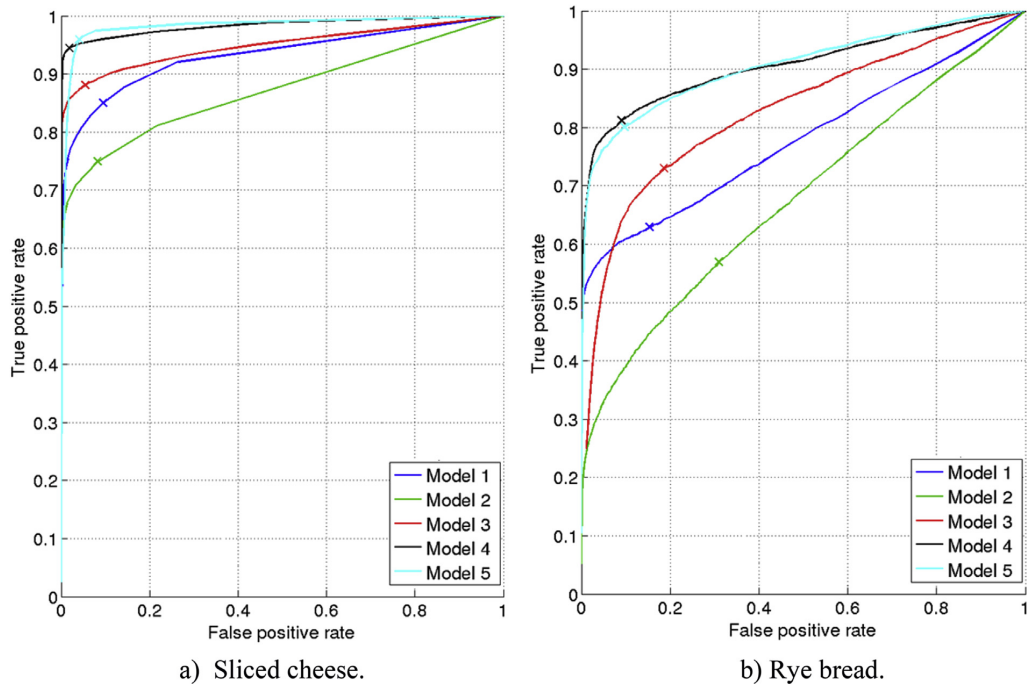a) Sliced cheese.   b) Rye bread.

Fig. 6. Receiver operating characteristic (ROC) curves for different models constructed.

Table 5
Minimum distance from ROC curve to ideal classification for the different food models.

	Cheese	Salami	Turkey	Rye bread	Wheat bread	Minced meat	Steak
Model 1	0.18	0.34	0.57	0.40	0.28	0.51	0.37
Model 2	0.26	0.42	0.37	0.53	0.51	0.54	0.36
Model 3	0.13	0.14	0.13	0.33	0.33	0.21	**0.07**
Model 4	**0.06**	0.11	0.11	**0.21**	0.24	**0.17**	0.08
Model 5	**0.06**	**0.08**	**0.07**	0.22	**0.22**	0.20	**0.07**

the best classification is obtained from the model combining both the multivariate intensity and texture features. For the other two products the models containing only intensity features outperform the model including texture features. Of all the products, rye bread and minced meat are the least homogeneous, and these results highlight the sensitivity to the chosen BIF parameters. An optimization of these parameters should be further explored to gain better classification when including these features in non-homogeneous food models.

Table 6 further illustrates the model comparison results, showing the true positive (TP) count, false positive (FP) count, true negative (TN) count and false negative (FN) count for all image

ACC = 92.3%. A slightly higher sensitivity is obtained when adding texture features, however at the cost of the specificity and accuracy of the classification.

3.3. Object based error rates

For food production purposes, a certain minimum size is typically required for foreign object detection, and objects smaller than this minimum can safely be disregarded. These smaller objects can be excluded by filtering the detected objects in the image by size. This will decrease the number of false positives, and a trade-off between detecting true foreign objects and eliminating false

Table 6
Comparison of pixel-wise classification results between different feature sets.

Food product	Model	TP	FP	TN	FN	Sensitivity	Specificity	Accuracy
Cheese	Model l	7062	3260	30,620	1260	84.9%	90.4%	89.3%
	Model 4	7832	534	33,346	514	93.8%	**98.4%**	**97.5%**
	Model 5	8004	1387	32,495	330	**96.0%**	95.9%	95.9%
Salami	Model l	5008	5716	33,877	2292	68.6%	85.6%	82.9%
	Model 4	6515	1795	37,831	752	89.7%	**95.5%**	**94.6%**
	Model 5	6850	2231	37,353	459	**93.7%**	94.4%	94.3%
Rye bread	Model l	1762	7365	40,456	1102	61.5%	84.6%	83.3%
	Model 4	2312	4506	43,342	527	**81.4%**	90.6%	90.1%
	Model 5	2270	4127	43,698	591	79.3%	**91.4%**	**90.7%**
Wheat bread	Model 1	6720	4595	29,833	2194	75.4%	86.7%	84.3%
	Model 4	7017	4279	30,149	1897	78.7%	87.6%	85.8%
	Model 5	7245	3483	30,944	1669	**81.3%**	**89.9%**	**88.1%**
Minced meat	Model 1	1880	9299	32,385	1544	54.9%	77.7%	76.0%
	Model 4	2890	3488	38,227	502	**85.2%**	**91.6%**	**91.2%**
	Model 5	2874	5400	36,288	546	84.0%	87.0%	86.8%
Steak	Model l	2788	6756	36,678	1454	65.7%	84.4%	82.8%
	Model 4	3941	1365	42,080	290	93.1%	**96.9%**	**96.5%**
	Model 5	3986	2181	41,264	245	**94.2%**	95.0%	94.9%
Turkey	Model l	1796	9593	30,424	1998	47.3%	76.0%	73.5%
	Model 4	3417	1592	38,424	378	90.0%	**96.0%**	**95.5%**
	Model 5	3555	1734	38,282	240	**93.7%**	95.7%	**95.5%**

positives can be made. This was explored by filtering the thresholded results from model 5 (combined multivariate intensity and texture). Fig. 7a shows the true positive rate based on an object count as a function of filtering size and Fig. 7b shows the number of false positives detected. As the filtering size is increased the number of false positives rapidly decreases. However, the TPR also decreases for rye bread minced meat, steak and turkey. It should also be noted that food products containing more texture (rye bread, wheat bread and minced meat) maintain a high number of false positives despite the filtering operation.

To further investigate the effect of filtering by size, the percentage of area detected per foreign object was calculated. This was done by first applying the optimal filter size for each food product in order to minimize the number of false positives obtained. These results are given in Table 7. All foreign objects are detected excluding the rubber piece (size 3) in minced meat and rye bread, the insect (size 1) and hard plastic (size 2) in the rye bread and wood piece (size 3) in the minced meat. As previously stated, these food products contain the most texture, and are therefore more sensitive to the BIF parameters chosen. A reasonable amount of the
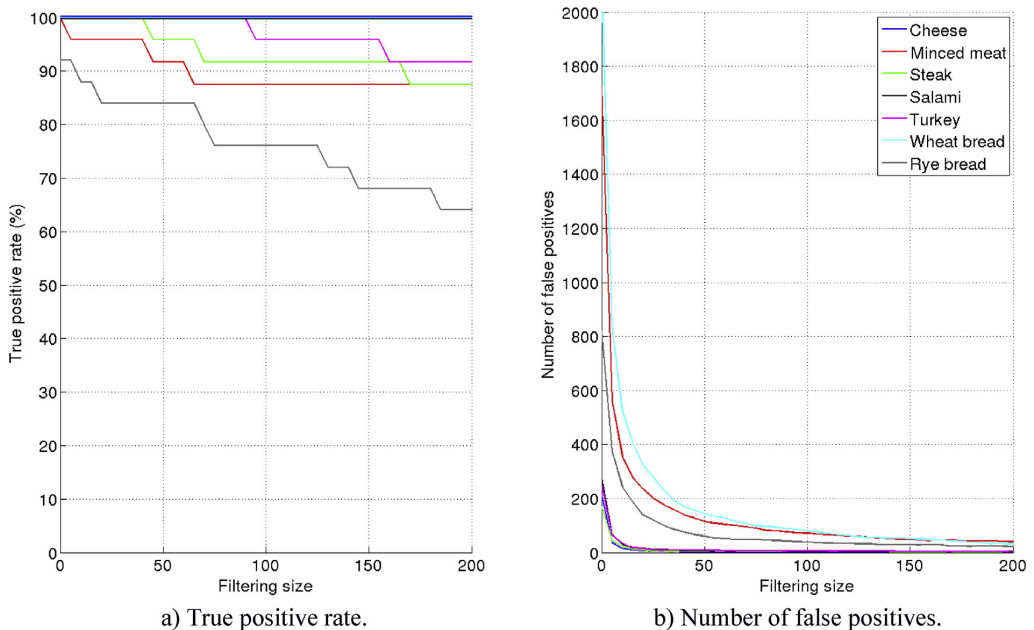

a) True positive rate.

b) Number of false positives.

Fig. 7. True positive rates and false positive rates as a function of filter sizes for excluding detected objects under a certain limit.

Table 7
Percentage of detected area of foreign objects in each size group and food product.

	Cheese			Salami			Turkey			Rump steak		
	Size 1	Size 2	Size 3	Size 1	Size 2	Size 3	Size 1	Size 2	Size 3	Size 1	Size 2	Size 3
Wood	100	100	99.8	100	100	100	100	100	100	100	100	82.2
Glass	100	100	100	100	100	99.5	100	100	92.7	96.8	95.6	69.8
Hard plastic	100	65.4	72.8	100	97.3	45.3	100	5.2	11.7	99.9	7.6	3.2
Soft plastic	100	95.7	97.9	100	95.6	98.6	99.1	99.8	97.5	99.9	85.8	92.7
Rubber	100	100	87.1	100	83.7	91.3	98.2	35.6	21.8	97.3	9.9	6.9
Stones	100	100	100	100	100	100	100	100	100	100	100	100
Metal	100	96.1	100	100	93.5	100	100	64.9	100	100	75.7	100
Insects	98.3	28.2	100	91.7	24.3	100	96.5	98	100	94.6	11.2	98.5

	Minced meat			Wheat bread			Rye bread		
	Size 1	Size 2	Size 3	Size 1	Size 2	Size 3	Size 1	Size 2	Size 3
Wood	100	100	-	100	100	99.8	92.6	92.7	6.3
Glass	84.9	44.0	49.5	100	100	100	99.7	96.4	99.2
Hard plastic	81.1	11.6	0.1	100	79.2	74.1	44.4	-	1.1
Soft plastic	96.9	55.0	91.2	100	33.4	12.5	3.23	0.1	2.8
Rubber	46.9	11.9	-	100	100	99.2	30.3	19.5	-
Stones	100	99.9	100	100	100	100	100	100	100
Metal	100	50.8	100	100	98.4	100	100	2.1	100
Insects	45.3	6.6	29.5	100	11.8	72.9	-	1.6	9.4

area of each foreign object is detected in most cases, despite the filtering of small detected regions. Therefore a compromise can be made, and for production purposes these parameters should be carefully chosen.

Both pixel-wise and object based results indicate a clear advantage when exploiting the mulitmodal capabilities of the grating-based X-ray technique over conventional absorption X-ray. A superior detection of organic matter was demonstrated, and applying multivariate methods for the novelty detection task gave higher detection rates in general. Texture analysis further increased the detection rates for food products which are homogeneous in texture. An optimization of BIF parameters is however needed and should be carefully explored for final algorithm implementations. The sensitive balance between detecting true positives and eliminating false positives should also be considered when designing a novelty detection algorithm, as excluding detected objects below a given size can significantly decrease the number of false positive at the cost of true positive detection rates.

To make the grating-based X-ray technique a feasible option for in-line product quality inspection, some obstacles need to be overcome. The technique currently only allows for a limited field-of-view, due to production methods available for the gratings required in the setup. Additionally, scanning methods for conveyor belt solutions need to be further developed, as this is a key element in increasing image acquisition speeds. Here several attempts have been made (Kottler, Pfeiffer, Bunk, Grünzweig, & David, 2007; Momose, Yashiro, Maikusa, & Takeda, 2009; Momose, 2014), where instead of stepping the gratings the object of interest is moved through an interferometer fringe pattern. These methods could possibly be implemented as a conveyor belt solution, providing high-speed imaging capabilities. Further limitations that need to be overcome are the limits to the energy of the X-ray source that can be used, as higher energy levels will allow for penetrating thicker food products.

4. Conclusions

In this paper the gain of using a grating-based X-ray technique over conventional X-ray imaging for foreign object detection was investigated. A novelty detection algorithm was developed to compare the X-ray imaging modality detection results and also to determine the gain of applying multivariate and texture analysis.

The results give a clear indication of superior detection results from the grating-based method, and especially show promising detection results of organic materials.

References

Bech, M., Bunk, O., Donath, T., Feidenhans'l, R., David, C., & Pfeiffer, F. (2010a). Quantitative x-ray dark-field computed tomography. *Physics in Medicine and Biology, 55*(18), 5529.

Bech, M., Jensen, T. H., Bunk, O., Donath, T., David, C., Weitkamp, T., et al. (2010b). Advanced contrast modalities for X-ray radiology: phase-contrast and dark-field imaging using a grating interferometer. *Zeitschrift fur Medizinische Physik, 20*, 7–16.

Bech, M., Jensen, T. H., Bunk, O., Donath, T., David, C., Weitkamp, T., et al. (2010c). Advanced contrast modalities for X-ray radiology: phase-contrast and dark-field imaging using grating interferometer. *Zeitschrift fuer medizinische Physik, 20*(1), 7–16.

Crosier, M., & Griffin, L. D. (2010). Using basic image features for texture classification. *International Journal of Computer Vision, 88*(3), 447–460.

Dempster, A. P., Laird, N. M., & Rubin, D. B. (1977). Maximum likelihood from incomplete data via th EM algorithm. *Journal of the Royal Statistical Society, 39*(1), 1–38.

Haff, R. P., & Toyofuku, N. (2008). X-ray detection of defects and contaminants in the food industry. *Sensing and Instrumentation for Food Quality and Safety, 2*(4), 262–273.

Jensen, T. H., Böttiger, A., Bech, M., Zanette, I., Weitkamp, T., Rutishauser, S., et al. (2011). X-ray phase-contrast tomography of porcine fat and rind. *Meat Science, 88*(3), 379–383.

Kottler, C., Pfeiffer, F., Bunk, O., Grünzweig, C., & David, C. (2007). Grating interferometer based scanning setup for hard X-ray phase contrast imaging. *Review of Scientific Instruments, 78*(4), 043710.

Kwon, J. S., Lee, J. M., & Kim, W. Y. (2008, April). Real-time detection of foreign objects using X-ray imaging for dry food manufacturing line. In *Consumer electronics, 2008. ISCE 2008. IEEE international symposium on* (pp. 1–4). IEEE.

Mahalanobis, P. C. (1936). On the generalised distance in statistics. *Proceedings of the National Institute of Sciences of India, 2*(1), 49–55.

Mery, D., Lillo, I., Loebel, H., Riffo, V., Soto, A., Cipriano, A., et al. (2011). Automated fish bone detection using X-ray imaging. *Journal of Food Engineering, 105*(3), 485–492.

Momose, A. (2014). *Development for non-destructive testing with X-ray grating interferometry*. Oral presentation at XNPIG2014.

Momose, A., Yashiro, W., Maikusa, H., & Takeda, Y. (2009). High-speed X-ray phase imaging and X-ray phase tomography with Talbot interferometer and white synchrotron radiation. *Optics Express, 17*(15), 12540–12545.

Nielsen, M. S., Lauridsen, T., Christensen, L. B., & Feidenhans'l, R. (2013). X-ray dark-field imaging for detection of foreign bodies in food. *Food Control, 30*(2), 531–535.

Pfeiffer, F., Bech, M., Bunk, O., Kraft, P., Eikenberry, E. F., Bronnimann, C., et al. (2008). Hard X-ray dark field-imaging using a grating interferometer. *Nature Materials, 7*(23), 134–137.

Pfeiffer, F., Bunk, O., David, C., Bech, M., Le Duc, G., Bravin, A., et al. (2007). High-resolution brain tumor visualization using three-dimensional x-ray phase contrast tomography. *Physics in Medicine and Biology, 52*(23), 6923–6930.

Pfeiffer, F., Weitkamp, T., Bunk, O., & David, C. (2006). Phase retrieval and differential phase-contrast imaging with low-brilliance X-ray sources. *Nature Physics, 2*, 258–261.

Scherer, K., Birnbacher, L., Chabior, M., Herzen, J., Mayr, D., Grandl, S., et al. (2014). Bi-directional X-ray phase-contrast mammography. *PloS One, 9*(5), e93502.

Song, X., Pogue, B. W., Jiang, S., Doyley, M. M., Dehghani, H., Tosteson, T. D., & Paulsen, K. D. (2004). Automated region detection based on the contrast-to-noise ratio in near-infrared tomography. *Applied Optics, 43*(5), 1053–1062.

Takashi, A. (2009). Detection for foreign bodies and bones in meat and meat products. In *Proceedings 55th international congress of meat science and technology. Copenhagen, Denmark*.

Zwiggelaar, R., Bull, C. R., Mooney, M. J., & Czarnes, S. (1997). The detection of "soft" materials by selective energy Xray transmission imaging and computer tomography. *Journal of Agricultural Engineering Research, 66*(3), 203–212.

Computer-aided diagnosis of pulmonary diseases using X-ray darkfield radiography

Computer-aided diagnosis of pulmonary diseases using x-ray darkfield radiography

Hildur Einarsdóttir[1]**, Andre Yaroshenko**[2]**, Astrid Velroyen**[2]**, Martin Bech**[2,3]**, Katharina Hellbach**[4]**, Sigrid Auweter**[4]**, Önder Yildirim**[5]**, Felix G Meinel**[4]**, Oliver Eickelberg**[5]**, Maximilian Reiser**[4]**, Rasmus Larsen**[1]**, Bjarne Kjær Ersbøll**[1] **and Franz Pfeiffer**[2]

[1] Department of Applied Mathematics and Computer Science, Technical University of Denmark, Richard Petersens Plads, Building 324, 2800 Kgs. Lyngby, Denmark
[2] Lehrstuhl für Biomedizinische Physik, Physik-Department & Institut für Medizintechnik, Technische Universität München, 85748 Garching, Germany
[3] Department for Medical Radiation Physics, Lund University, 22185 Lund, Sweden
[4] Institute for Clinical Radiology, Ludwig-Maximilians-University Hospital Munich, 80539 Munich, Germany
[5] Comprehensive Pneumology Center, Institute of Lung Biology and Disease, Member of the German Center for Lung Research (DZL), Helmholtz Zentrum München, 85764 Neuherberg, Germany

E-mail: hildr@dtu.dk

CrossMark

Abstract

In this work we develop a computer-aided diagnosis (CAD) scheme for classification of pulmonary disease for grating-based x-ray radiography. In addition to conventional transmission radiography, the grating-based technique provides a dark-field imaging modality, which utilizes the scattering properties of the x-rays. This modality has shown great potential for diagnosing early stage emphysema and fibrosis in mouse lungs *in vivo*. The CAD scheme is developed to assist radiologists and other medical experts to develop new diagnostic methods when evaluating grating-based images. The scheme consists of three stages: (i) automatic lung segmentation; (ii) feature extraction from lung shape and dark-field image intensities; (iii) classification between healthy, emphysema and fibrosis lungs. A study of 102 mice was conducted with 34 healthy, 52 emphysema and 16 fibrosis subjects. Each image was manually annotated to build an experimental dataset. System performance was assessed by: (i) determining the quality of the segmentations; (ii) validating emphysema and fibrosis recognition by a linear support vector machine using leave-one-out cross-validation. In terms of

segmentation quality, we obtained an overlap percentage (Ω) 92.63 $\pm$ 3.65%, Dice Similarity Coefficient (DSC) 89.74 $\pm$ 8.84% and Jaccard Similarity Coefficient 82.39 $\pm$ 12.62%. For classification, the accuracy, sensitivity and specificity of diseased lung recognition was 100%. Classification between emphysema and fibrosis resulted in an accuracy of 93%, whilst the sensitivity was 94% and specificity 88%. In addition to the automatic classification of lungs, deviation maps created by the CAD scheme provide a visual aid for medical experts to further assess the severity of pulmonary disease in the lung, and highlights regions affected.

Keywords: X-ray radiography, dark-field imaging, lung segmentation, active appearance model, pulmonary disease, Grating based interferometry

(Some figures may appear in colour only in the online journal)

1. Introduction

Pulmonary diseases are one of the leading causes of death worldwide, and are characterized by structural abnormalities of the lung. Between the most frequent disorders are pulmonary emphysema and fibrosis. A common approach to diagnose these disorders is chest radiography (Sutinen *et al* 1965, Pratt 1987). However, this technique offers only a limited sensitivity, and the poor contrast of lung tissue makes it difficult to diagnose mild to moderate cases. In case of an unclear diagnosis the patient is forwarded to high resolution CT (Thurlbeck and Müller 1994), which offers substantially enhanced sensitivity at the disadvantage of a very high radiation exposure dose, which limits especially frequent follow-up examinations. Typically, for both cases, a computer-aided diagnostic (CAD) approach is designed to assist radiologists to assess the severity of the disease. Different features can be extracted from the acquired data, and both intensity values of the lung regions and shape features can be analyzed. In Coppini *et al* (2013) a CAD scheme to detect emphysema was developed based on shape features extracted from chest radiography. Similarly, a CAD scheme for detecting pneumoconiosis from chest radiography based on intensity features was demonstrated in Yu *et al* (2011).

Recent advances in x-ray techniques have introduced new imaging modalities such as phase-contrast and dark field, obtainable by grating-based interferometry (Pfeiffer *et al* 2006, Pfeiffer *et al* 2008). These modalities allow for visualizing the refraction and scattering properties of the x-rays, in addition to the conventional attenuation-based x-ray imaging. Dark-field imaging has shown promising results in visualizing the respiratory system of a mouse *in vivo* (Bech *et al* 2013, Yaroshenko *et al* 2014a) and further to diagnose pulmonary emphysema in *ex vivo* murine lungs (Schleede *et al* 2012, Yaroshenko *et al* 2013). A prototype *in vivo* small-animal scanner was developed based on grating interferometry (Tapfer *et al* 2012), which makes it possible to acquire dark field radiographies of mice *in vivo*. The dark-field contrast reveals the information about tissue air interfaces of the lung. Recently, a study has been reported that first showed that dark field lead to a better diagnostic value for the diagnosis of pulmonary emphysema in living mice (Meinel *et al* 2014). The conventional x-ray transmission images revealed only slight indirect signs of pulmonary disease, while the dark-field images clearly showed a significant difference between healthy and emphysematous lungs. A further study (Hellbach *et al* 2015) demonstrated that by visual assessment of dark-field radiographs, different stages of emphysema can be determined. Early stages of the disorder

were not visible on conventional transmission images, whilst mild to moderate stages could easily be distinguished in the dark-field images.

In this paper, we further build upon these results and develop a CAD scheme to analyze the images obtained from the small-animal scanner. The purpose of this scheme is to assist radiologist to interpret the new imaging modality, as they have limited diagnostic training and experience with dark-field images. The scheme consists of three main steps: (i) Lung segmentation; (ii) feature extraction; (iii) classification. The lung segmentation is based on an active appearance model (Cootes and Taylor 2001), and models for both the absorption and dark-field data are created. From the segmented lung regions, a model of a healthy lung is created. This is done by calculating the pixel-wise mean and standard deviation of 15 control lungs. For all subsequent lungs, a deviation map is created to determine regions affected by pulmonary disease. For the feature extraction step, both intensity and shape features are considered. Classification results, based on the two features sets both independently and combined, are presented. The final classification is then performed by a linear support vector machine (SVM) (Cortes and Vapnik 1995) and is twofold. First a classification between 'healthy versus diseased' is made, and if classified as non-healthy, a classification of 'emphysema versus fibrosis' is made. The results of the developed CAD scheme are demonstrated on a dataset of 102 lung images, consisting of 34 healthy lungs, 52 emphysematous and 16 fibrosis.

2. Materials and methods

2.1. Grating-based imaging

The grating-based interferometer is described in detail in Pfeiffer *et al* (2006) and Pfeiffer (2008). The imaging modalities obtained with a grating interferometer consist of three types of physical interactions—attenuation, refraction and scattering. The imaging modalities are refered to as absorption, phase contrast and dark-field imaging. The setup for grating-based imaging (GBI) is shown in figure 1. The phase grating produces a periodic intensity modulation consisting of periodic fringes transverse to the beam direction. The change in position, mean value and amplitude of the periodic fringes can be probed using an analyzer grating by moving one of the gratings in steps through the period in the pattern while recording an image at each step. The source grating may be added to obtain coherent virtual line sources from standard x-ray generators with source sizes of more than a square millimeter (Pfeiffer *et al* 2006). From this series of scans, the absorption, refraction and small-angle scattering can be recorded by a detector using the same exposures, giving an inherent pixel correspondence. For this study, only the absorption and dark-field modalities are used.

2.2. Dataset

Animal experiments were performed with permission of the responsible Institutional Animal Care and Use Committee. Either emphysema or fibrosis was induced in female mice and compared to control subjects. Emphysema was induced using elastase and the protocol is described in Meinel *et al* (2014). For fibrosis, the mice received orotracheally 3.0 units/kg body weight of bleomycin dissolved in 80 μl sterile phosphate-buffered saline (PBS). The control animals received 80 μl sterile PBS. The fibrosis animals were imaged 14 d after instillation and sacrificed shortly after. For this purpose the lungs were fixated in 4% paraformaldehyde. During imaging the mice were anesthetized using intra- peritoneal injection of medetomidine (500 μg kg^{-1}), midazolam (5 mg kg^{-1}), and fentanyl (50 μg kg^{-1}) (Meinel *et al* 2014). The successful
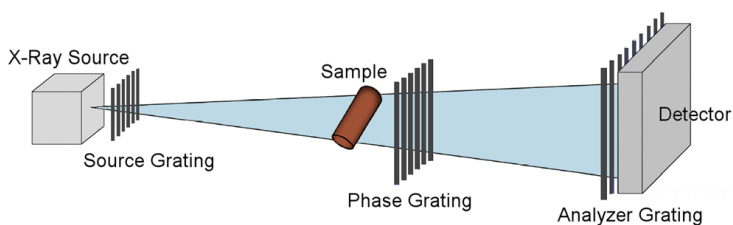
Figure 1. A schematic of a x-ray radiography setup using a grating interferometer.

induction of emphysema and fibrosis in mice was confirmed by (quantitative) histology. To assess the severity of emphysema and fibrosis the histological sections were analyzed using a light microscope equipped with a computer-assisted stereologic toolbox. For emphysema the mean chord length (mean alveoli size) and for fibrosis the mean tissue percentage (amount of solid tissue) were quantified. Further details on the emphysema quantification can be found in Meinel *et al* (2014).

A total of 102 radiographs where obtained from two separate groups of mice *in vivo* using a prototype small-animal x-ray dark-field scanner as described in Meinel *et al* (2014) using the same image protocol. The radiographs consist of absorption and dark-field images from each scan, with pixel correspondence between the modalities, resulting in a total of 204 images. Three groups were included in the dataset: control (34), emphysema (52) and fibrosis (16). The images of emphysema mice where part of a longitudinal study, and therefore the same mice were measured several times during a period of 21 d. For the acquisition of the dark-field images, five images for different source grating positions were acquired with an exposure time of 3.3 s per image, resulting in a total acquisition time of approximately 17 s. The total acquisition dose for a dark-field projection image is approximately 1.8 mGy. The dose estimation method is described in Meinel *et al* (2014).

2.3. CAD scheme for classification of pulmonary disease

The CAD scheme for classifying pulmonary disease consists of the following phases:

1. Lung segmentation.
2. Feature extraction (both shape and intensity).
3. Classification between healthy, emphysematous and fibrosis lungs.

Each step will be described in detail in the following sections.

2.3.1. Lung segmentation.

The aim of the segmentation process is to extract the lung regions for further feature extraction. For this task, the well established active appearance model (AAM) algorithm is utilized (Cootes and Taylor 2001). The algorithm is an efficient optimization approach that matches shape and texture simultaneously. It consists of a two-step process, training and segmentation, which are briefly summarized by the following steps:

Training

Step 1: Key landmark points are manually placed on the training images.
Step 2: The manually annotated images are aligned by scaling, rotating and translating.

Step 3: A statistical model of shape and texture variation is generated by applying principal component analysis (PCA).

Segmentation

Step 1. A rough approximate starting position is found at which the mean shape is centered.
Step 2. For each landmark, a region of the image is examined to find the best nearby match.
Step 3. The model parameters are updated to best fit the new found points.
Step 4. Steps 2 and 3 are repeated until convergence.

An AAM implementation presented in Hansen *et al* (2011) was adapted for the lung segmentation task. A training set of 30 lung images are first manually annotated with 52 landmarks consisting of 38 around the contour of the lung, 7 landmarks placed at the upper part of the diaphragm and 7 landmarks at the position of the heart. To initialize the starting position of the AAM for new lung images, a center point of the lung is found. This is done by determining the widest part of the lung in the dark-field image from the row sum profile, and the location of the spine in the absorption image, determined by the column sum profile. This is illustrated in figure 2, where these two points are determined in figure 2(a) and the mean lung shape is then positioned as in figure 2(b).

2.3.2. Feature extraction. Pulmonary disease both causes a change in shape and texture of the lung, and typical x-ray characteristic signs are over-expanded lungs, a flattened diaphragm and increased retrosternal airspace (Torres and Moayedi 2007). With dark-field imaging, x-rays are scattered on the interface between air and tissue in the lung (alveoli) and any changes in the airspace structure are therefore visible (Yaroshenko *et al* 2014b). Additionally, the lung shape is clearly visible in the dark-field modality and can also be analyzed. Both intensity and shape features of the lung are therefore considered important.

2.3.2.1. Intensity features. To extract the intensity features, first a healthy model is created based on a set of 15 control lungs. For this case 15 healthy lung images were selected and segmented by the AAM. The segmented lungs are then aligned by Procrustes superimposition, which translates, rotates and uniformly scales the lungs to minimize any shape difference between them. By an affine transformation, the texture of the lungs is then warped to this aligned shape to obtain a pixel-wise correspondence between the intensities. The statistics of the healthy lungs are then calculated, by determining the pixel-wise mean μ_{ij} and standard deviation s_{ij} for every pixel ij amongst the $N = 15$ healthy subjects. The pixel-wise mean and standard deviation are given by

$$\mu_{\text{model},ij} = \frac{1}{N}\left(\sum_{k=1}^{N} x_{ijk}\right) \tag{1}$$

$$s_{\text{model},ij} = \sqrt{\frac{1}{N}\sum_{k=1}^{N}(x_{ijk} - \mu_{ij})^2} \tag{2}$$

where x_{ij} is the intensity of pixel ij.

Given the statistics of the healthy model, deviation maps are created for all other lungs by calculating the *t*-test statistic of each pixel from the healthy model

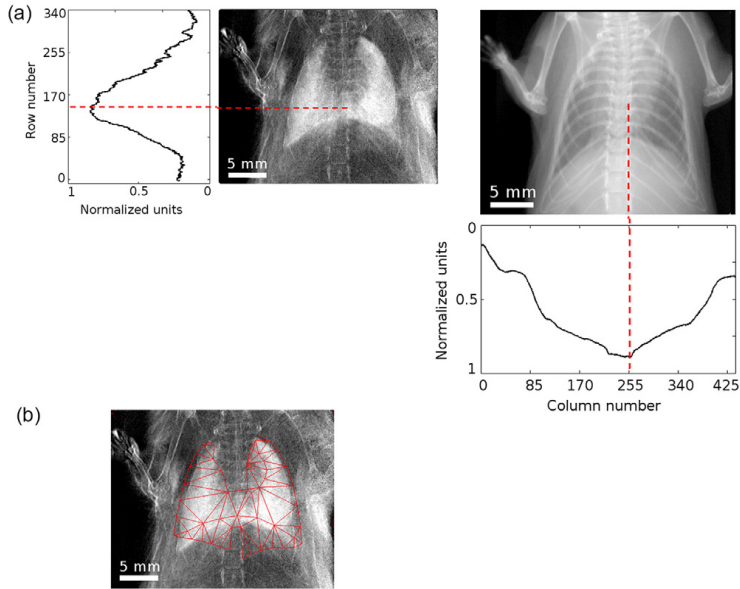$$t_{ij} = \frac{x_{ij} - \mu_{\text{model},ij}}{s_{\text{model},ij}}. \tag{3}$$

Figure 2. To obtain a starting position for the AAM, the minimum values of the row sum from darkfield and column sum from absorption are found, representing the approximate location of the center of the lung. (a) Row sum of the dark-field and column sum of the absorption image (arbitrary units). (b) Initial starting position for AAM.

The deviation maps highlight the regions of abnormal intensity and can visually aid a radiologist in the diagnosis of pulmonary disease. In order to use the deviation maps for classification purposes further feature extraction is required. The following deviation map histogram features are thus extracted: Mean value, M_1; standard deviation, M_2; skew, M_3; kurtosis, M_4; median value, M_5; median absolute deviation, MAD_1; mean absolute deviation, MAD_2; entropy, EP; and maximum intensity value of the histogram, M_6. These features are calculated as follows:

$$M_1 = \sum i \cdot h(i), \tag{4}$$

$$M_2 = \sqrt{\sum (i - M_1)^2 \cdot h(i)}, \tag{5}$$

$$M_3 = \frac{1}{M_2^3} \sum (i - M_1)^3 \cdot h(i), \tag{6}$$

$$M_4 = \frac{1}{M_2^4} \sum (i - M_1)^4 \cdot h(i) - 3, \tag{7}$$

$$M_5 = \text{median } h(i), \tag{8}$$

$$\text{MAD}_1 = \text{median}\left((h(i) - \text{median } h(i))\right), \tag{9}$$

$$\text{MAD}_2 = \text{mean}\left((h(i) - M_1)\right), \tag{10}$$

$$\text{EP} = -\sum h(i) \cdot \log h(i), \tag{11}$$

where $h(i)$ denotes the histogram of the intensity i.

2.3.2.2. Shape features. To determine the main type of variation present in the shape profiles of the lungs, a principal component analysis (PCA) of the segmented shapes is performed (Jolliffe 2002). PCA is a statistical method that by orthogonal transformation converts a set of observations of possibly correlated variables into a set of values of linearly uncorrelated variables called principal components. In other words, the original data is rotated such that a new coordinate system is obtained where the coordinate axes (principal axes) maximizes the variance of the projected data. The first axis explains most of the variation in the data, and the variation explained decreases with each sequential axis. Each component is a linear combination of all initial features (landmarks) and therefore investigating the first principal component can shed light on the shape variation present in the lung dataset.

Additional lung features are derived directly from each segmented lung region and include the height, width and area of the lung. The top margin T, bottom margin B, left margin L, and right margin R are thus determined. The shape features extracted then consist of: Lung height, $H = T–B$; lung width, $W = L–R$; lung area, A, which is the number of pixels in the lung region; first shape principal component score, PC_1; and the area of severe deviation (over 2 standard deviations), A_s.

2.3.3. Lung classification. For the classification task, a simple linear support vector machine (SVM) is implemented (Cortes and Vapnik 1995). The lung classification is performed in two steps, first a classification between control lungs versus rest is made and thereafter a classification between emphysema and fibrosis lungs is made. A leave-one-out cross-validation was used to optimize the cost function parameter and to validate the SVM results.

3. Results

3.1. Lung segmentation

Figure 3 shows the segmentation results for four separate lung images, where the lung regions are successfully located in all images. Visually, the quality of the segmentations is acceptable, and all 102 lungs were successfully segmented. Only the severe cases of fibrosis required the use of the absorption AAM to obtain a reasonable segmentation, while the dark-field AAM gave good results for the remaining lungs.

A quantitative assessment was performed, comparing the segmentation results to manually placed landmarks. The performance was evaluated using the Dice Similarity Coefficient, Jaccard Similarity Coefficient and overlap percentage by leave-one-out cross-validation. The Dice coefficient is a statistic for comparing the similarity of two samples, the Jaccard coefficient is used for comparing the similarity and diversity of a sample set and the overlap percentage measures the overlap between two sets. Figure 4 shows these results, where boxplots of the coefficients for both the absorption and dark-field AAM model are given. The boxplots
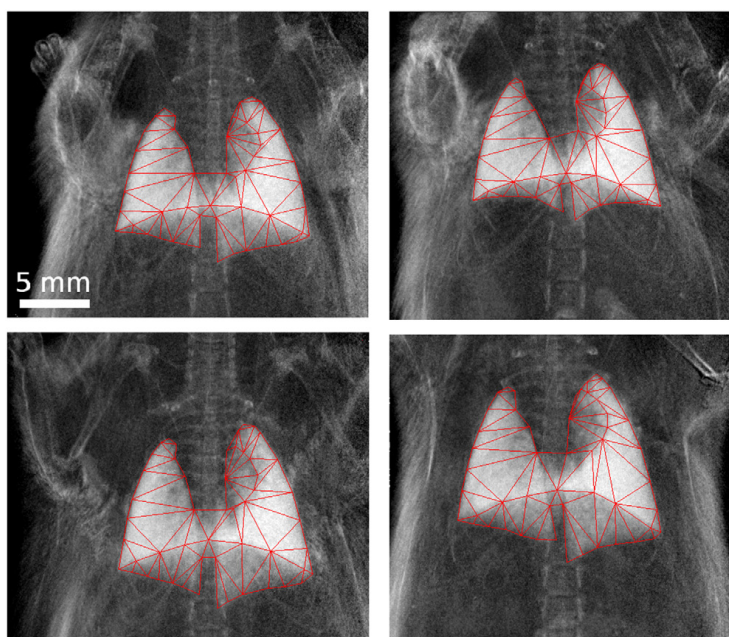
Figure 3. Examples of lung field segmentation results using the AAM algorithm.

depict the results through their quartiles where the central mark is the median and the edges of the box are the 25th and 75th percentiles, with whiskers indicating the variability outside the upper and lower quartiles. Outliers are then plotted as individual points. It is apparent that the dark-field model gives a better performance for the control and emphysema groups. Here the scores are quite high for all three measures. For severe cases of fibrosis, the dark-field lung signal can be negligible, and therefore data support for the AAM is not sufficient for a successful segmentation. For these cases it was necessary to segment using the absorption images, where the rib cage is always visible giving the AAM full data support. The segmentation results for the control and emphysema groups are not as good when using the absorption model. Therefore a strategy of trying both models individually for each lung and manually selecting the better result was employed.

3.2. Deviation maps

Figure 5 shows the healthy lung atlas consisting of the pixel-wise mean and standard deviation maps, given by equations (1) and (2) respectively. The images are shown in color to better enhance the maps. Regions near the edges of the lungs show higher deviation, especially around the heart and diaphragm regions. This is caused by a large variability in size and position of the organs.
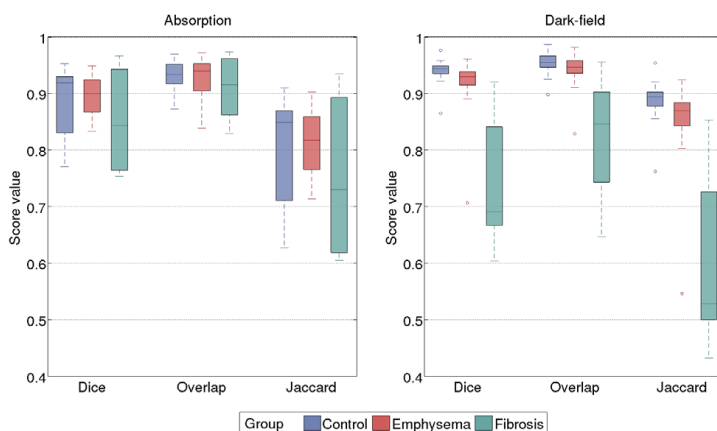
Figure 4. Boxplot of the Dice, overlap and Jaccard scores for the segmented lungs, given both for the absorption- and dark-field AAMs.
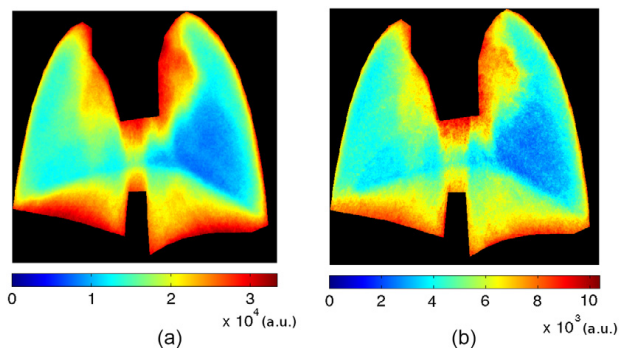

Figure 5. The healthy lung model consists of the pixel-wise mean and standard deviation values for the dark-field control lung images.

A sample of the segmented texture images and deviation maps found by eqaution (3) is shown in figure 6. The dark-field texture is warped to the mean shape in order to make a direct comparison of lung regions possible. Each pixel location in the texture image therefore corresponds between all lungs. A control lung, fibrosis lung and emphysema lung is given as an example, where the emphysema lung is shown at day 7, 12 and 14 after instillation. The dark-field signal decreases for the emphysema lung across days, and the deviation map clearly enhances the regions affected. The control lung barely differs from the healthy lung model, and therefore shows low deviation in all regions. The fibrosis lung is severely damaged, causing high deviation from the healthy model in most regions. Table 1 gives the average deviation
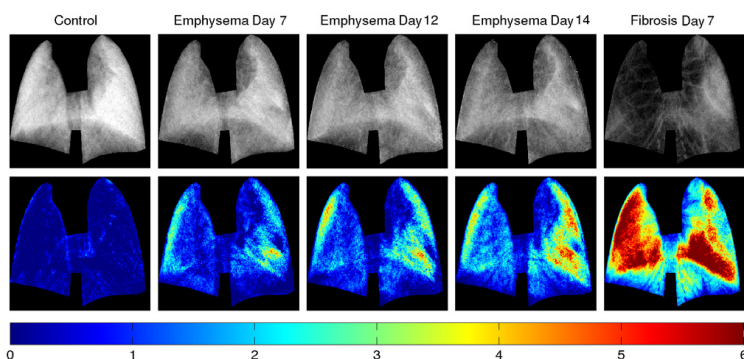
Figure 6. Deviation maps shown for a control-, emphysema- and fibrosis mouse. The emphysema maps show the same mouse at different stages of emphysema. The color scale illustrates the magnitude of deviation.

Table 1. Average deviation values, μ_d, and the area of severe deviation, $A_s > 2\sigma$, given for five sample lungs.

	Control	Emphysema day 7	Emphysema day 12	Emphysema day 14	Fibrosis day 7
μ_d	0.1 ± 0.46	0.90 ± 0.84	1.16 ± 0.99	1.63 ± 1.16	3.55 ± 1.80
A_s	0.00%	10.82%	19.11%	31.59%	78.08%

values μ_d for these lungs, along with the area of severe deviation (above 2σ), A_s. It is worth noting that all intensity features used for later classification are extracted from these warped deviation maps.

The warped dark-field images and deviation maps indicate which lungs are affected by either emphysema or fibrosis. For medical diagnostic purposes however it is necessary to warp the texture back to the original lung image. Figure 7 shows the original dark-field images of the same lungs as in figure 6, where the deviation maps have been warped to the original shape. These maps can then assist the qualitative diagnostics of the lung images.

3.3. Shape statistics

The first three principal components (PCs) for the shape profiles are shown in figure 8. They illustrate the mean shape $\pm 3\sigma$ of the PCs. The first PC mainly constitutes the variation in lung size, while the second PC is concerned with the positioning and slant of the bottom region of the lung. Finally, a variation in the width of the lung is seen in the third PC. The first PC constitutes 57.5% of the variance of the shape profiles, and is used as a shape feature for the classification step. Figure 9 shows the normalized first principal component score for the lung shapes. All control lungs except for one result in a negative score, while most emphysema lungs give a positive score. There is not a clear distinction for the fibrosis lungs, which indicates the need for other discriminative features.
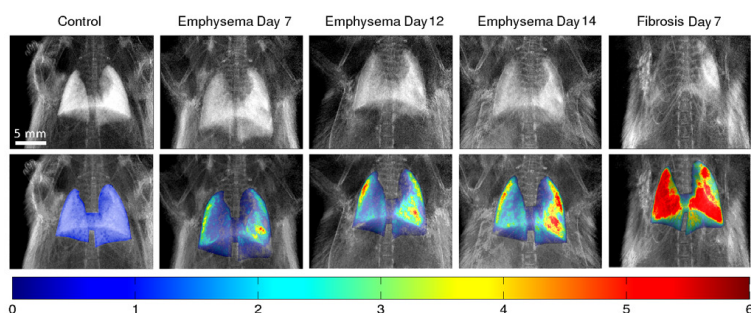
Figure 7. Deviations maps overlayed on top of the original dark-field images. The color scale illustrates the magnitude of deviation.
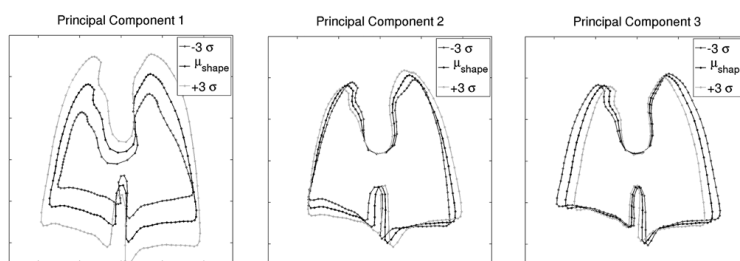

Figure 8. First three principal components of the shape parameters after Procrustes alignment (excluding scaling). The first principal component is mainly concerned with the size of the lung and constitutes 57.5% of the variance of the shape profiles.

3.4. Feature significance

To determine the feature significance and gain of evaluating the deviation maps rather than the dark-field images, we test the null-hypothesis that both healthy and non-healthy mice belong to the same population, that is for each parameter i that the means are equal, $\mu_{1i} = \mu_{2i}$. Table 2 shows the p-values for parameters found by evaluating the dark-field images directly and the deviation maps. It is obvious that evaluating the deviation maps results in significantly lower p-values in most cases, and therefore the intensity features are extracted from the deviation maps rather than the dark-field images.

3.5. Classification results

The classification results from the SVM, determined using leave-one-out cross-validation (Kohavi 1995), are given in tables 3 and 4. Different feature sets are compared, where shape and intensity features are used either separately or combined. Table 3 gives the results when classifying healthy versus non-healthy lungs, where healthy control lungs are depicted as negatives (N) and non-healthy as positives (P). A slightly better result is obtained using intensity
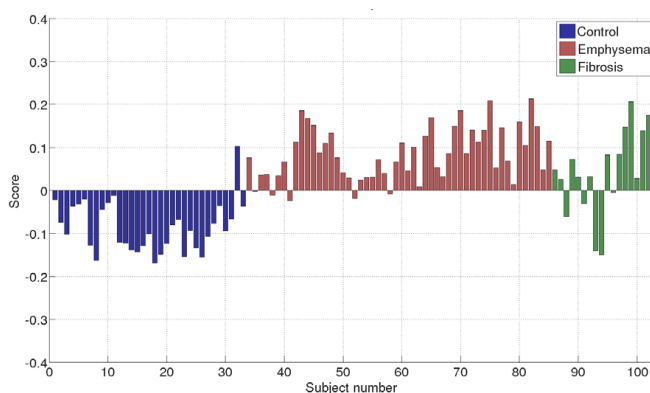
Figure 9. Bar plot illustrating the normalized first principal component score for all lungs.

Table 2. *P*-values for the different intensity features extracted for both the original dark-field images and deviation maps.

Parameter	Dark-field	Deviation map
Mean, M_1	<0.0001	<0.0001
Standard deviation, M_2	0.0748	<0.0001
Skewness, M_3	<0.0001	<0.0001
Kurtosis, M_4	0.4249	0.0778
Median, M_5	<0.0001	<0.0001
Maximum intensity, M_6	<0.0001	<0.0001
MAD (median), MAD_1	0.3597	<0.0001
MAD (mean), MAD_2	0.0807	<0.0001

Table 3. Comparison of classification results between different feature sets. Diseased lungs are given as true positives (TP) and healthy lungs are given as true negatives (TN).

Features for SVM	Number of features	TP	TN	FP	FN	Sensitivity	Specificity	Accuracy
Shape[a]	5	64 (68)	33 (34)	1	4	94.12%	97.06%	95.10%
Intensity[b]	9	65 (68)	34 (34)	0	3	95.59%	100.00%	97.06%
Intensity and shape	14	68 (68)	34 (34)	0	0	100.00%	100.00%	100.00%

[a] Shape features: Area, A; width of lung, W; height of lung, H; area of severe deviation (over 2 standard deviations), A_s; and first shape principal component score, PC_1.
[b] Intensity features: Mean value, M_1; standard deviation, M_2; skew, M_3; kurtosis, M_4; median value, M_5; median absolute deviation, MAD_1; mean absolute deviation, MAD_2; entropy, EP; and maximum intensity value of histogram, M_6.

based features over shape features. The combined model however outperforms the other two, resulting in perfect classification. When classifying between emphysema and fibrosis lungs, the intensity features also result in a better classification than the shape features alone, see

Table 4. Comparison of classification results between different feature sets. Emphysema lungs are given as true positives (TP) and fibrosis lungs are given as true negatives (TN).

Features for SVM	Number of features	TP	TN	FP	FN	Sensitivity	Specificity	Accuracy
Shape[a]	5	45 (52)	13 (16)	3	7	86.54%	81.25%	85.29%
Intensity[b]	9	47 (52)	12 (16)	4	5	90.38%	75.00%	86.76%
Intensity and shape	14	49 (52)	14 (16)	2	3	94.23%	87.50%	92.65%

[a] Shape features: Area, A; width of lung, W; height of lung, H; area of severe deviation (over 2 standard deviations), A_s; and first shape principal component score, PC_1.

[b] Intensity features: Mean value, M_1; standard deviation, M_2; skew, M_3; kurtosis, M_4; median value, M_5; median absolute deviation, MAD_1; mean absolute deviation, MAD_2; entropy, EP; and maximum intensity value of histogram, M_6.

table 4. The performance increases when combining the two sets, however it does not result in perfect classification as for the healthy versus non-healthy case. The misclassification of emphysema and fibrosis are shown in figure 10. The fibrosis cases classified as emphysema are both relatively healthy, however they show a very prominent heart shadow in the left lung. Both mice (D and E) display this behavior and therefore the misclassification seems to be systematic. Only mild emphysema is seen in the misclassified emphysema mice, and mouse C also has a large heart shadow as the fibrosis cases. It is assumed that the amount of shadowing from the heart heavily depends on the exact positioning of the mouse in the scanner, and therefore calls for an accurate placement to achieve repeatability in the resulting dark-field images. Finally, figure 11 shows examples of correctly classified lungs from all three groups.

4. Discussion

A CAD scheme for diagnosing emphysema and fibrosis from grating-based x-ray radiographs has been described. It consists of three stages: (i) automatic lung segmentation using an active appearance model; (ii) extraction of both intensity and shape features of the segmented lung; (iii) classification of healthy, emphysema or fibrosis lung based on a linear support vector machine.

The active appearance model successfully segmented all 102 lung images, either by using the data given in the dark-field image or the data from the absorption image. The segmentations based on the dark-field images gave more accurate segmentations compared to ground truth determined by an expert. However, data support for severely damaged lungs was insufficient. In these few cases the absorption AAM gave full data support, where the lung regions were segmented by fitting the rib cage visible in the images. For further implementation of the CAD scheme, an AAM combining the absorption- and dark-field data simultaneously should be considered.

From the segmented lung fields, relevant features were extracted combining shape and intensity information of the lung. A principal component analysis of the shape profiles illustrated a large variation in size between healthy and diseased lungs, which significantly contributes to correct classification of the lung in question. Additionally, intensity features based on deviation maps from healthy lung statistics were extracted, as these gave lower p-values than features extracted directly from the dark-field images.

Linear support vector machines were trained and validated using leave-one-out cross-validation, to classify two separate cases: (i) classification of healthy against diseased lungs; (ii) classification between emphysema and fibrosis lungs. Different feature sets were
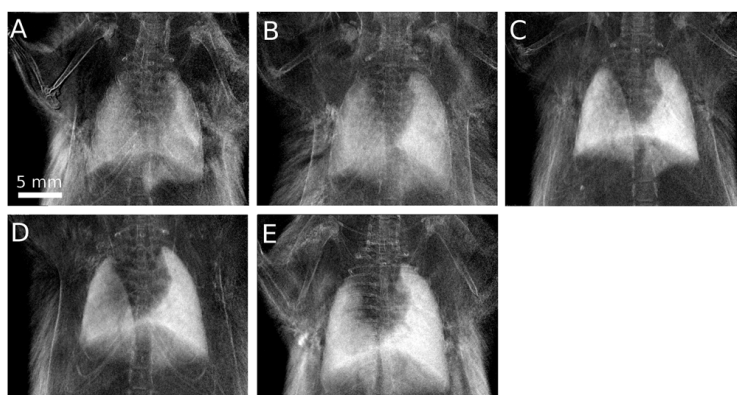
Figure 10. Incorrect classification results from SVM. A to C show emphysema lungs classified as fibrosis. D and E show fibrosis lungs classified as emphysema.
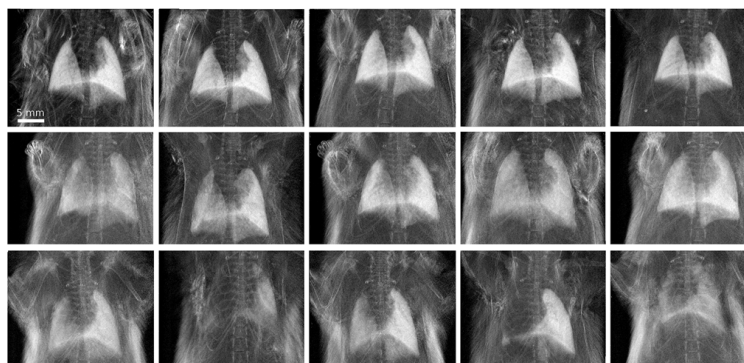

Figure 11. A sample of correct classifications determined by SVM. Top row: correct control classifications; middle row: correct emphysema classifications; bottom row: correct fibrosis classifications.

compared, either using intensity or shape features individually or combining the two feature sets. For both classification tasks, the intensity features gave better classification results than using shape features alone. Combining the two sets gave superior results for classification task (i), resulting in no misclassification of the 102 images. For classification task (ii), 3 out of 52 emphysema and 2 out of 16 fibrosis lungs where misclassified when using the combined feature set.

The analysis revealed a tendency for the emphysema lungs to expand with progressing disorder, whereas the fibrosis lungs tend not to change shape. This feature plays a large role in the classification of healthy versus emphysema versus fibrosis lungs. It should however be

noted that emphysema and fibrosis can coexist and a strategy to classify these cases should be investigated.

Future development of the CAD scheme will involve a classification scheme capable of determining the severity of pulmonary disease. In order to do so, a scheme for rating lung images according to severity is required, and suggested subgroups would be: healthy, mild, moderate and severe. This grouping has previously been demonstrated in Hellbach *et al* (2015).

The developed CAD scheme is intended to assist new diagnostic techniques for pulmonary disease using x-ray dark-field imaging. At this stage only mouse trials have been performed, however the CAD scheme has been developed such that it can easily be adapted to other subjects, such as pigs, and in the future, human trials. The training of the AAM model requires only minimal input from the user, where the landmarks are manually annotated on training images. Other adjustments include performing a new principal component analysis of the shape profiles and re-training the linear SVM. In general it can be expected that the human lung will display similar behavior as observed in mice, that is to say that a healthy lung will give a very strong dark field signal and a reduction of scattering is expected for emphysematous lungs. It remains still an open question whether the ribs (and also other tissue such as e.g. fat layer) in humans will be visible also in the dark-field projections. This would clearly complicate the model. However, it can be expected that the same features for intensity and shape can also be used to stage emphysema and fibrosis in humans.

In order to create a generic solution valid across different setups the following must be considered. The dark-field signal of the lung strongly depends on the setup parameters like the grating periods, distances between the gratings, etc. Consequently, to account for the signal variations at different setups it is necessary to implement a scaling factor, as a function of the setup parameters. Theoretical work for the scaling of the dark-field signal has been reported by Yashiro *et al* (2010), Lynch *et al* (2011) and Strobl (2014). Therefore, a more complex model would be necessary to take the dark-field signal scaling into account. However, to ensure the correct normalization it would be necessary to measure a phantom with a structure similar to the lung in all setups and verify the correct scaling factor. This is left for future work.

Acknowledgments

References

Bech M, Tapfer A, Velroyen A, Yaroshenko A, Pauwels B, Hostens J, Bruyndonckx P, Sasov A and Pfeiffer F 2013 *In vivo* dark-field and phase-contrast x-ray imaging *Sci. Rep.* **3** 3209
Cootes T F and Taylor C J 2001 Statistical models of appearance for medical image analysis and computer vision *Med. Imaging* **4322** 236–48

Coppini G, Miniati M, Monti S, Paterni M, Favilla R and Ferdeghini E M 2013 A computer-aided diagnosis approach for emphysema recognition in chest radiography *Med. Eng. Phys.* **35** 63–73

Cortes C and Vapnik V 1995 Support-vector networks *Mach. Learn.* **20** 273–97

Hansen M F, Fagertun J and Larsen R 2011 Elastic appearance models *22nd British Machine Vision Conf.* (http://dx.doi.org/10.5244/c.25.91)

Hellbach K *et al* 2015 *In vivo* dark-field radiography for early diagnosis and staging of pulmonary emphysema *Invest. Radiol.* **50** 430–5

Jolliffe I 2002 *Principal Component Analysis* (New York: Wiley)

Kohavi R 1995 A study of cross-validation and bootstrap for accuracy estimation and model selection *IJCAI* **14** 1137–45

Lynch S K *et al* 2011 Interoretation of dark-field contrast and particle-size selectivity in grating interferometers *Appl. Opt.* **50** 4310–9

Meinel F G *et al* 2014 Improved diagnosis of pulmonary emphysema using *in vivo* dark-field radiography *Invest. Radiol.* **49** 653–8

Pfeiffer F, Weitkamp T, Bunk O and David C 2006 Phase retrieval and differential phase-contrast imaging with low-brilliance x-ray sources *Nat. Phys.* **2** 258–61

Pfeiffer F, Bech M, Bunk O, Kraft P, Eikenberry E F, Brönnimann Ch, Grünzweig C and David C 2008 Hard-x-ray dark-field imaging using a grating interferometer. *Nat. Mater.* **7** 134–7

Pratt P C 1987 Role of conventional chest radiography in diagnosis and exclusion of emphysema *Am. J. Med.* **82** 998–1006

Schleede S *et al* 2012 Emphysema diagnosis using x-ray dark-field imaging at a laser-driven compact synchrotron light source *PNAS* **109** 17880–5

Strobl M 2014 General solution for quantitative dark-field contrast imaging with grating interferometers *Sci. Rep.* **4**

Sutinen S, Christoforidis A J, Klugh G A and Pratt P C 1965 Roentgenologic criteria for the recognition of nonsymptomatic pulmonary emphysema. Correlation between roentgenologic findings and pulmonary pathology *Am. Rev. Respir. Dis.* **91** 69–76

Tapfer A *et al* 2012 Experimental results from a preclinical x-ray phase-contrast CT scanner *Proc. Natl Acad. Sci.* **109** 15691–6

Thurlbeck W M and Müller N L 1994 Emphysema: definition, imaging, and quantification *AJR Am. J, Roentgenol.* **163** 1017–25

Torres M and Moayedi S 2007 Evaluation of the acutely dyspneic elderly patient *Clin. Geriatr. Med.* **23** 307–25

Yaroshenko A, Hellbach K, Bech M, Grandl S, Reiser M F, Pfeiffer F and Meinel F G 2014a Grating-based x-ray dark-field imaging: a new paradigm in radiography *Curr. Radiol. Rep.* **2** 1–9

Yaroshenko A *et al* 2014b Small-animal dark-field radiography for pulmonary emphysema evaluation *SPIE Med. Imaging* **9033** 90331M

Yaroshenko A *et al* 2013 Pulmonary emphysema diagnosis with a preclinical small-animal x-ray dark-field scatter-contrast scanner *Radiology* **269** 427–33

Yashiro W, Terui Y, Kawabata K and Momose A 2010 On the origin of visibility contrast in x-ray Talbot interferometry *Opt. Express* **18** 16890–901

Yu P, Xu H, Zhu Y, Yang C, Sun X and Zhao J 2011 An automatic computer-aided detection scheme for pneumoconiosis on digital chest radiographs *J. Digit. Imaging* **24** 382–93